

Victor Arturo Martinez Lopez

# Enhancing Solar Energy Integration with Innovative mini-modules



# Enhancing Solar Energy Integration with Innovative Mini-modules

by

VICTOR ARTURO MARTINEZ LOPEZ

in partial fulfilment of the requirements for the degree of

**Master of Science**

in Electrical Power Engineering

at the Delft University of Technology,

to be defended publicly on Wednesday August 28<sup>th</sup>, 2019 at 10:00 AM.

Student number	4746678	
Thesis Committee	Dr. ir. O. Isabella	TU Delft, supervisor
	Ir. J.C. Ortiz Lizcano	TU Delft, daily supervisor
	Prof. dr. ir. M. Zeman	TU Delft, Head of the ESE department
	Prof. dr. ir. Kasper Jansen	TU Delft, External committee member

*This thesis is confidential and cannot be made public until August 31, 2020.*

An electronic version of this thesis is available at <http://repository.tudelft.nl/>.



# Abstract

As solar energy finds its way into unexpected applications such as buildings or objects, the traditional rectangle-shaped module becomes inadequate. Although traditional modules have been optimized to deliver a large amount of power, they cannot be fitted easily into a façade or a wearable. This is why, new methods for integrating solar power into buildings and products have to be found. These methods should be attractive to designers and architects and must also allow solar energy to reach common people.

The fabrication of mini-modules can help with this task as they can be fabricated with the already mature technology of crystalline silicon solar cells. They can be made lightweight and in different figures.

This work aims to investigate ways to facilitate the fabrication of modules for use in Building Integrated Photovoltaics or Product Integrating Photovoltaics by means of studying the impact of cutting solar cells into different figures and sizes. Connection methods such as magnets and conductive tapes are also studied in order to determine their suitability in photovoltaic applications.

After this analysis, two demonstrators are built to prove the concepts. An origami based foldable module that makes use of the tape as a substitution for cables and a photovoltaic puzzle which uses magnets to connect individual cells.

The prototypes demonstrate that commercial cells can be easily processed to obtain innovative modules that can be customized according to a designer's need. Furthermore, magnetic contacts were proven to be suitable as photovoltaic contacts, at least for small power applications. This eliminates the need for connectors and speeds up the connection process.



# Preface

Before coming to The Netherlands, I started to develop an interest for solar energy. Now, two years later I write this thesis with passion for solar energy. This passion was enhanced by the PVMD group of the TU Delft. Starting with Miro and Olindo who gave me the opportunity, not only to participate in this project, but also who had confidence in me for assisting the PV lab course as Teaching Assistant.

Juan Camilo who had enough patience to guide this work and encouraged me to develop my ideas “*Eso, hagámoslo*” was his answer to every crazy idea I came up with.

The rest of the PhDs of the group provided invaluable feedback and answer to my doubts. I especially recognize the help of Andres who also showed interest in my project and explained me things that were unclear.

Stefaan and Martijn, our technicians provided invaluable help and patience with teaching me how to use the equipment and fixing problems.

My fellow MSc colleagues helped me a lot with interesting discussions, but also laughter moments or even a lunch. Sukanya and YiLong, who also helped in the PV lab shared with me this project even closer.

Outside the group, my Mexican-Ecuadorian friends, Celia, Armando, Yoelito and the rest of the team, not only provided countless hours of studying but also excellent moments that sometimes ended when the sun was about to come out.

Bea, Roland and Elise helped me finding a new home in this part of the world with dinners and board games.

I couldn't have achieved this without the loving support of my wife, Alessandra who encouraged me to come here, in the first place.

And of course, my family in Mexico. My loving parents Eric and Laura and my grandparents, Abu and Mimi. A special mention to my sister, Lore, who always showed interest in what I was doing and even, payed a visit every now and then.

The financial support of the *Consejo Nacional de Ciencia y Tecnología (CONACYT)* of the Mexican government was of prime importance.

To all of you, and the rest of people who accompanied me in this journey, many, many thanks. You really made this possible.

Arturo Martinez

August, 2019.





# Contents

Abstract.....	iii
Preface.....	v
Contents .....	vii
List of Figures .....	xi
List of Tables .....	xi
List of abbreviations .....	xiii
List of symbols.....	xv
1 Introduction .....	1
1.1. PV in everyday life.....	2
1.1.1. Building Integrated Photovoltaics (BIPV).....	2
1.1.2. Product Integrated Photovoltaics (PIPV).....	3
2 Methodology.....	5
2.1. Overview of the equipment used.....	5
1.2.1. Lasergraaf laser cutter.....	5
1.2.2. WACOM solar simulator.....	6
1.2.3. PASAN flash tester.....	6
1.2.4. EXPERIA laminator .....	7
1.2.5. LAMBDA spectrometer.....	8
1.2.6. Solar simulators SASS and LASS .....	9
2.2. Laser cutting.....	10
2.2.1. Parameter estimation of the Lasergraaf cutter .....	10
2.3. Shape and size .....	11
2.4. Cell-To-Module ratio .....	13
2.5. Prototypes.....	14
3 Creating custom shapes .....	15
3.1. Solar cell cutting.....	15
1.3.1. Laser cutting.....	15
1.3.2. Laser induced damage.....	16
3.2. Cell shape and size .....	18
2.3.1. Pulse duration.....	18
2.3.2. Speed (s) and frequency (f).....	20

2.3.3.	Repetitions .....	22
2.3.4.	Optimal laser configuration .....	23
2.3.5.	Effect of cell area .....	23
2.3.6.	Effect of cell shape.....	27
3.3.	Future work .....	32
3.4.	Conclusions .....	33
4	Building mini modules .....	35
4.1.	Cell-To-Module.....	35
1.4.1.	Inactive areas .....	36
1.4.2.	Optical losses .....	37
1.4.3.	Optical gains .....	43
1.4.4.	Resistive losses .....	46
1.4.5.	CTM ratio of the reference module. ....	46
4.2.	Electrical contacts .....	50
2.4.1.	Theory of electrical contacts.....	50
2.4.2.	Contact materials .....	51
2.4.3.	Electrically conductive adhesives .....	52
2.4.4.	Neodymium magnets .....	52
2.4.5.	Analysis of the proposed contacts.....	53
4.3.	Future work .....	55
4.4.	Conclusions .....	55
5	Foldable module .....	57
5.1.	The Miura-Ori fold.....	57
5.2.	Origami in photovoltaics .....	58
5.3.	Design of the foldable module .....	59
5.4.	Prototype .....	61
4.5.1.	Effect of the front sheet material .....	63
4.5.2.	Prototype performance.....	65
5.5.	Future work .....	68
5.6.	Conclusions .....	69
6	Solar puzzle .....	71
6.1.	Puzzle Requirements .....	72
6.2.	Cell shapes.....	73
6.3.	Mini module interconnection .....	75
6.4.	Final design .....	77

6.5.	Analysis of the finished puzzle .....	78
6.6.	Future work and applications .....	81
6.7.	Conclusions .....	82
7	Conclusion and Recommendations .....	83
7.1.	Recommendations .....	84
1.7.1.	Laser cutting.....	84
1.7.2.	Cell-To module .....	85
1.7.3.	Electrical contacts .....	85
1.7.4.	Foldable module.....	85
1.7.5.	PV puzzle .....	86
8	References .....	87
	Appendix.....	91
8.1.	Lasergraaf technical specifications .....	91
8.2.	Method for determining the Cell-To-Module ratio .....	91
8.3.	Buck converter design for the foldable module .....	92



# List of Figures

FIGURE 1. (A) LASERGRAAF LASER CUTTER. (B) OPERATING PRINCIPLE OF THE MACHINE. THE WHOLE FIGURE WAS ADAPTED FROM [15]. ..... 5

FIGURE 2. (A) WACOM SOLAR SIMULATOR AT TU DELFT. (B) COMPARISON OF THE SPECTRA OF THE WACOM AND AM1.5. PLOTTED WITH DATA FROM THE PVMD GROUP AT TU DELFT. ... 6

FIGURE 3. (A) PASAN IID FLASH TESTER HELD AT TU DELFT. (B) COMPARISON OF THE SPECTRA OF PASAN AND AM1.5. NOTE THE LARGE PEAKS IN THE INFRARED SECTION. PLOTTED WITH DATA FROM THE PVMD GROUP AT TU DELFT. .... 7

FIGURE 4. EXPERIA LAMINATOR. TAKEN FROM [18]. ..... 8

FIGURE 5, LAMDA 950. RETRIEVED FROM [20] .(B) WORKING PRINCIPLE OF THE INTEGRATING SPHERE. ONLY TRANSMITTANCE OR REFLECTANCE CAN BE MEASURED AT A TIME. ADAPTED FROM [19]. ..... 9

FIGURE 6. EXPERIMENT SETUP FOR THE MEASUREMENT OF THE IV CURVES FOR THE PIECES OF THE PV PUZZLE USING A MANUAL SWEEP. .... 9

FIGURE 7. LASS (A) AND SASS (B) HELD AT THE PV LABORATORY OF TU DELFT. .... 9

FIGURE 8. SCHEMATIC OF AN AKW CELL. ADAPTED FROM [21]. ..... 10

FIGURE 9. CELL SIZE EXPERIMENT ..... 11

FIGURE 10. CUT CELL SHAPES. THE TWO HEXAGONS, AS WELL AS THE TWO RECTANGLES, SHOWN HERE HAVE EXACTLY THE SAME DIMENSIONS. NOTE THAT THE BUSBARS IN THESE FIGURES CAN HAVE DIFFERENT ORIENTATION. .... 12

FIGURE 11. CUT EQUILATERAL TRIANGLES ..... 12

FIGURE 12. CUT HEXAGONS. THE DISPLACEMENT OF THE BUSBAR IS A RESULT OF A MISALIGNMENT OF THE LASER BEAM WITH RESPECT TO THE DESIRED MARKING PATH AND THE FACT THAT THE BACK CONTACT DOES NOT ALIGN PERFECTLY WITH THE FRONT ONE. THE CELLS WERE CUT FROM THE BACK. .... 12

FIGURE 13. PATTERNS USED FOR MEASURING THE RESISTANCE OF THE COPPER TAPE. FIRST, A COMPLETE SEGMENT WAS MEASURED (A). THEN, TWO TAPE SEGMENTS WERE GLUED TOGETHER (B). AN ANALOG PROCEDURE WAS DONE WITH THREE TAPE SEGMENTS (C). THE TERMINAL TYPE OF (D) REFERS TO THE CONFIGURATION USED FOR THE PV PUZZLE, WHILE (E) SHOWS THE PAD BUILT FOR MEASURING THE INDIVIDUAL PIECES OF THE PV PUZZLE. .... 14

FIGURE 14. LASER PULSES. THE AREA OF EACH PULSE IS THE ENERGY OF THE PULSE  $E_p$ . ..... 16

FIGURE 15. EQUIVALENT CIRCUIT OF A SOLAR CELL CONSIDERING THE EDGES. A SECOND DIODE  $I_E$  IS ADDED TO ACCOUNT FOR RECOMBINATION LOSSES AT THE EDGE.  $R_E$  REPRESENTS THE DISTANCE FROM THE MAIN BODY OF THE CELL TO THE EDGE; THUS, SEPARATING THE TWO PARTS. RETRIEVED FROM [26]. ..... 16

FIGURE 16. OPTICAL MICROSCOPY OF THE SIDE OF AN UNCUT C-SI CELL. NOTE THAT THE EDGE APPEARS SMOOTH. .... 17

FIGURE 17. OPTICAL MICROSCOPY OF THE SIDE OF A BROKEN C-SI CELL. THE EDGE IS STILL SMOOTH. .... 17

FIGURE 18. OPTICAL MICROSCOPY OF A LASER CUT CELL. NOTE THAT THE EFFECT OF THE LASER BECOMES CLEARLY VISIBLE AND THAT THE EDGE IS NOT SMOOTH ANYMORE BUT ROUGH. THE REMAINING PART (CLEAVED) IS STILL SMOOTH. .... 18

FIGURE 19. FREQUENCY THRESHOLD FOR DIFFERENT  $T_{ON}$  VALUES. AS THE  $T_{ON}$  INCREASES, THE MINIMUM USABLE FREQUENCY SHIFTS TO A LOWER VALUE. FOR INSTANCE, FOR A LOWER  $T_{ON}$ , FREQUENCY  $F_4$  CAN BE USED. HOWEVER, IF THE  $T_{ON}$  IS INCREASED A LOWER MINIMUM FREQUENCY ( $F_3$ ) HAS TO BE CONSIDERED. IF FOR THE GIVEN VALUE OF  $T_{ON}$  THAT LEADS TO A MINIMUM FREQUENCY  $F_3$ , LOWER FREQUENCY IS CHOSEN, THE OUTPUT POWER WILL BE LESS THAN THE NOMINAL POWER. HOW LESS? IT CANNOT BE ESTABLISHED AS IT IS GIVEN BY THE MACHINE ITSELF. ADAPTED FROM [16] AND [32]. 19

FIGURE 20. PULSE OVERLAP AS SPEED AND FREQUENCY CHANGE. .... 20

FIGURE 21. KERF DEVELOPMENT. DURING THE FIRST PASSES OF THE LASER THE KERF IS WIDE. THIS ALLOWS THE LASER BEAM TO HIT IN THE MIDDLE OF THE KERF; THUS, LEADING TO A GREATER DEPTH. HOWEVER, AS THE CUT DEVELOPS, THE KERF BECOME NARROWER. AT SOME POINT THE LASER WILL IMPING ON THE WALLS OF THE SUBSTRATE, MAKING THE ACHIEVEMENT OF THE DESIRED DEPTH MORE DIFFICULT..... 21

FIGURE 22. COMPARISON OF DIFFERENT LASER CONFIGURATIONS USED FOR FINE TUNING. ON THE X-AXIS, THE USED PARAMETERS OF THE SAMPLES ARE COMPARED. (F)-FREQUENCY IN [KHZ], (S)-SPEED IN [MM/S] AND (R) - REPETITIONS (NUMBER OF PASSES). IN ALL CASES, THE OUTPUT POWER WAS SET AT 100% ..... 22

FIGURE 23. CHANGE OF THE EFFICIENCY AS THE AREA INCREASES. THE EFFICIENCY OF THE UNCUT CELL IS MARKED AS REFERENCE (“FULL CELL”). NOTE THAT FOR CELL AREAS SMALLER THAN 9 [CM<sup>2</sup>] THE EFFICIENCY DROP IS CONSIDERABLE. .... 24

FIGURE 24. EFFECT OF THE AREA ON THE SHORT-CIRCUIT CURRENT. A LINEAR FIT (“ISC FIT”) WAS DONE TO BETTER CLARIFY THE LINEAR BEHAVIOR OF THE SHORT CIRCUIT CURRENT AND THE AREA..... 24

FIGURE 25. EFFECT OF THE CELL AREA ON THE VOC. ALTHOUGH THE DROP OF THE VOC APPEARS FOR AREAS LARGER THAN 9 [CM<sup>2</sup>], BELOW THIS LIMIT THE QUICK DROP CAN BE SEEN AS A VERY STEEP SLOPE OF THE CURVE..... 25

FIGURE 26. FILL FACTOR FOR DIFFERENT CELL AREAS. NOTE THE LARGE DISPERSION OF THE MEASURED VALUES SHOWN BY THE WHISKERS. FROM THIS DATA, NO RELATION CAN BE INFERRED BETWEEN THE FILL FACTOR AND THE CELL AREA. .... 25

FIGURE 27. ILLUMINATED IV CURVES FOR DIFFERENT CELL SIZES. THE DASHED CIRCLE INDICATES THE ZOOMED AREA OF FIGURE 28. .... 26

FIGURE 28. DETAIL OF THE ILLUMINATED IV CURVES FOR DIFFERENT CELL SIZES. THE ARROWS ARE POINTING AT THE SLOPE OF THE IV CURVE NEAR THE VOC POINT. THE STEEPER THE SLOPE, THE LESS SERIES RESISTANCE OF THE CELL. A VERY FLAT IV CURVE SUCH AS THE ONE FOR 5.2 [CM<sup>2</sup>] INDICATE A VERY HIGH SERIES RESISTANCE. ... 26

FIGURE 29. EFFECT OF THE AREA ON THE SERIES CELL RESISTANCE. THE INCREASED  $R_s$  IS ATTRIBUTED TO A LOSS OF OPTIMIZATION OF THE METAL GRID AT THE FRONT SIDE. .... 27

FIGURE 30. EFFICIENCY PER CELL SHAPE. NOTE THAT FOR THE SAME  $R_s$ , THERE ARE DIFFERENT EFFICIENCIES. THIS IS BECAUSE THE DIMENSIONS OF THE CELLS ARE DIFFERENT, ALBEIT THE SAME FIGURE. A DEVIATION FROM THE DASHED LINES INDICATE THAT THE FIGURES ARE NOT REGULAR FIGURES AS IS THE CASE WITH THE CIRCLE CELL WHICH IS MORE AN ELLIPSE, AND SOME OF THE SQUARE CELLS. .... 28

FIGURE 31. OVERALL COMPARISON OF CELL SHAPES. IT WAS EXPECTED THAT THE HIGHER EFFICIENCIES WOULD BEEN ACHIEVED WITH A CIRCLE AND A HEXAGON, HOWEVER SQUARES AND HEXAGONS HAVE THE BEST PERFORMANCE. WHY?..... 29

FIGURE 32. COMPLETE AKW CELL. THE YELLOW ARROWS POINT TO THE FINGERS THAT SEPARATE THIS COMPLETE CELL INTO THREE SUBCELLS. THIS SEPARATION IS DONE DIRECTLY BY THE MANUFACTURER..... 30

FIGURE 33. LARGE HEXAGON. THE DOTTED LINES SHOW THE PARTS WHERE THE CELL IS SUBDIVIDED INTO THREE DIFFERENT SUBCELLS (MARKED AS SUBCELL 1, 2 AND 3). ONLY SUBCELL 2 HAS A BUSBAR THAT ALLOWS CARRIER COLLECTION. CHARGE CARRIERS GENERATED IN SUBCELLS 2 AND 3 HAVE LOWER PROBABILITY OF COLLECTION AS THEY HAVE TO TRAVEL THROUGH A LARGER AREA. .... 30

FIGURE 34. SHADED FRACTION OF DIFFERENT CELL SHAPES. CIRCLES AND HEXAGONS, WHICH HAVE A LOWER PERIMETER-TO-AREA, ARE IN DISADVANTAGE WITH SQUARES AND RECTANGLES THAT HAVE LESS SHADED FRACTION. .... 31

FIGURE 35. FIGURE EFFICIENCY BY SHAPE DIMENSION ( $K$ ) AND SHADED FRACTION. THE DOTTED LINE SOWS THE LIMIT FOR CELLS WITH EFFICIENCIES ABOVE 19%. THE SAMPLES MARKED AS “TRI38” AND “HEX47” APPEAR IN THE “HIGH EFFICIENCY ZONE” BUT HAVE LOWER THAN 19% EFFICIENCY HAVE THEIR AREAS SPLIT INTO SEVERAL SUBCELLS..... 32

FIGURE 36. OPERATING POINT OF THE SERIES-CONNECTED CELLS. FOR CLARITY, ONLY THREE CELLS ARE PLOTTED. NOTE THAT THE GRAPH IS ZOOMED AROUND THE MAXIMUM POWER POINT. THESE THREE CELLS ARE OPERATING AT THE CURRENT MARKED BY THE DASHED LINE (“OPERATING CURRENT”) WHICH IS DICTATED BY THE LEAST PRODUCING CELL (“CELL 2”). ONLY THIS CELL WILL BE AT ITS MPP WHILE THE OPERATING POINT OF THE REST SHOULD BE DETERMINED. .... 36

FIGURE 37. SCHEMATIC OF THE OPTICAL LOSSES. OBSERVE HOW THE INCOMING LIGHT BEAM BECOMES THINNER AS IT CROSSES THROUGH THE DIFFERENT INTERFACES..... 37

FIGURE 38. CORNING GLASS REFLECTIVITY PER WAVELENGTH. THE PEAK AT AROUND 850 [NM] IS DUE TO A CHANGE IN THE SENSORS WITHIN THE EQUIPMENT. .... 38

FIGURE 39. MEASURED AKW SOLAR CELLS SPECTRAL RESPONSE..... 39

FIGURE 40. AM1.5 SPECTRUM. RETRIEVED FROM [38]..... 39

FIGURE 41. SPECTRAL ABSORBANCE OF THE CORNING GLASS ..... 40

FIGURE 42. REFRACTIVE INDICES OF CORNING GLASS AND EVA. .... 41

FIGURE 43. REFLECTIVITY AT THE GLASS-EVA INTERFACE. AS EXPECTED, THE GOOD MATCHING OF THE REFRACTING INDICES OF GLASS AND ENCAPSULANT IS TRANSLATED INTO A VERY LOW REFLECTIVITY AT THE GLASS-EVA INTERFACE. .... 42

FIGURE 44. SPECTRAL ABSORBANCE OF THE EVA. THIS ENCAPSULANT ABSORBS ALMOST NO LIGHT IN THE VISIBLE NOR INFRARED RANGE. HOWEVER, IT ABSORBS MOST OF THE ULTRAVIOLET LIGHT..... 43

FIGURE 45. OPTICAL GAINS. THESE ARE ACHIEVED FROM THE REFLECTION FROM THE BACK SHEET, THE COUPLING OF THE REFRACTIVE INDICES OF THE ANTI-REFLECTIVE (AR) COATING AND THE ENCAPSULANT; THE SCATTERING FROM THE BUSBARS AND METAL FINGERS..... 43

FIGURE 46. SHORT CIRCUIT CURRENT CHANGE WHEN VARYING THE SPACING BETWEEN CELLS. IT WOULD SEEM THAT IF THE INTER-CELL SPACING IS LESS THAN 2 [MM] (INDUSTRY STANDARD) THE BLACK OVER PERFORMS THE WHITE BACK SHEET. NEVERTHELESS, THE READER SHOULD BE CAUTIOUS IN INTERPRETING THE GRAPH. BOTH CURVES ARE A FIT. THIS MEANS THAT THE BEHAVIOR IS JUST AN APPROXIMATION. IF MORE POINTS ARE USED THE FITTING WOULD IMPROVE. HOWEVER, MAKING MODULES WITH CELL SPACES BELOW 2 [MM] IS VERY DIFFICULT AND UNPRACTICAL. HENCE, THESE MEASUREMENTS CAN BE AVOIDED. .... 45

FIGURE 47. FABRICATED REFERENCE MODULE. .... 47

FIGURE 48. CTM EFFICIENCY ANALYSIS OF THE REFERENCE MODULE. THE RED COLOR SHOWS THE LOSS MECHANISMS; THE YELLOW, THE GAINS. THE NUMBER ABOVE EACH BAR INDICATES THE RESULTING MODULE EFFICIENCY AFTER CONSIDERING EACH EFFECT. . 49

FIGURE 49. CTM POWER ANALYSIS OF THE REFERENCE MODULE. THE RED BARS INDICATE LOSS MECHANISMS WHILE THE YELLOW ONES GAINS. THE NUMBER ABOVE EACH BAR IS THE RESULTANT POWER AFTER EACH EFFECT IS CONSIDERED. NOTE THAT THE INACTIVE AREAS DO NOT CAUSE POWER LOSSES. .... 50

FIGURE 50. OVERVIEW OF AN ELECTRICAL CONTACT. SOME OF THE CURRENT LINES HAVE BEEN OMITTED FOR CLARITY. NOTE HOW THE A-SPOTS CONSTITUTE A CONSTRICTION FOR THE CURRENT. ADAPTED FROM [40]..... 51

FIGURE 51. *POT MAGNET* USED IN THIS WORK. ADAPTED FROM [46]..... 53

FIGURE 52. RESISTANCE ANALYSIS OF THE ELECTRICALLY CONDUCTIVE COPPER ADHESIVE TAPE. THE RED DASHED LINE MARKS THE RESISTANCE OF THE COPPER SIDE (WITHOUT ADHESIVE) OF THE TAPE. THIS IS USED AS REFERENCE FOR COMPARING THE BEHAVIOR OF THE ADHESIVE UNDER DIFFERENT SCENARIOS. THE WORDS “WORN” AND “OLD” INDICATE THAT THE TAPE WAS ATTACHED, REMOVED AND RE-ATTACHED AGAIN TO SIMULATE AGING. IT BECOMES OBVIOUS THAT, AS THE GLUE AGES OR LOSES ITS ADHESIVE STRENGTH, THE RESISTIVITY INCREASES. REFER TO FIGURE 13 FOR A LIST OF THE PATTERNS USED. .... 54

FIGURE 53. BOXPLOT OF THE MEASUREMENTS OF THE *DIFFERENCE* IN CURRENT BEFORE AND AFTER THE MAGNET. NOTE THAT THE MEDIAN IS 2 [MA] WHICH IS A VERY SMALL VALUE..... 55

FIGURE 54. CREASE PATTERN OF THE MIURA FOLD. THE SHADED AREA CORRESPONDS TO A *FUNDAMENTAL REGION*. .... 57

FIGURE 55. UNIT MINI MODULE. ON THE LEFT, A MINI MODULE WITH TRAPEZOIDAL CELLS. RIGHT, A MINI MODULE WITH SQUARE CELLS. .... 60



FIGURE 56. PROPOSED CONNECTION SCHEME FOR THE FOLDABLE MODULE. NOTE THAT THE TERMINALS ARE IN ONE CORNER ELEMENT. THIS ALLOWS THE INSERTION OF AN EXTERNAL CIRCUIT OR JUNCTION BOX WITHOUT INTERFERING WITH THE FOLDING. ....	61
FIGURE 57. UNFOLDED PROTOTYPE. BY PAINTING THE BUSBARS WITH A BLACK PERMANENT MARKER, THE CELLS BECAME PRACTICALLY INVISIBLE. ....	62
FIGURE 58. FOLDED STATE. TOP VIEW. THE DIMENSIONS ARE 24 X 19 [CM]. ....	62
FIGURE 59. COMPARISON OF THE TRANSMITTANCE OF THE CORNING GLASS AND FLEXIBLE FRONT SHEET. ALTHOUGH THE GLASS HAS A GREATER TRANSMITTANCE FOR LOWER WAVELENGTHS THAN THE FRONT SHEET, THE WAVELENGTHS IN THIS REGION PRODUCE LESS ELECTRONS. ON THE PEAK OF THE SPECTRAL RESPONSE OF THE CELLS, BOTH MATERIALS BEHAVE ALMOST THE SAME. THE SPECTRAL RESPONSES OF BOTH, THE AKW AND VIKO CELLS ARE PLOTTED FOR REFERENCE. ....	63
FIGURE 60. REFRACTIVE INDICES OF THE CORNING GLASS AND FRONT SHEET. THE SPECTRAL RESPONSE OF THE AKW AND VIKO CELLS ARE PLOTTED FOR REFERENCE. THE REFRACTIVE INDEX OF THE EVA IS ALSO PLOTTED. THE GLASS HAS A BETTER MATCHING THAN THE FRONT SHEET, EVEN AROUND 900 [NM] WHERE THE SPECTRAL RESPONSE OF THE CELLS IS AT ITS HIGHEST. HOWEVER, IN THIS REGION THE DIFFERENCE IS SMALL. ....	64
FIGURE 61. REFLECTANCE OF THE CORNING GLASS WITH RESPECT TO THE FRONT SHEET. THE REFLECTANCE OF THE FRONT SHEET OVER PERFORMS THAT OF THE CORNING GLASS IN THE REGION WHERE THE CELL RESPONDS BETTER. IN THE SMALL WAVELENGTH REGION, THE SITUATION IS OPPOSITE. HOWEVER, THE CELL DOES NOT PERFORM WELL IN THIS REGION. ....	64
FIGURE 62. ABSORPTANCE OF THE FRONT SHEET AND CORNING GLASS. NOTE THAT THE FRONT SHEET ABSORBS MORE LIGHT THAN THE GLASS. ....	65
FIGURE 63. IV AND PV CURVES OF THE FOLDABLE MODULE JUST AFTER FABRICATION. ....	66
FIGURE 64. DE-RATING OF THE SHORT CIRCUIT CURRENT AS A RESULT OF FOLDING AND UNFOLDING. IN ALL CASES, THE CURRENT DECREASED INDICATING THAT THE FOLDING HAD AN EFFECT ON THE CONNECTIONS. ....	67
FIGURE 65. ELECTROLUMINESCENCE ANALYSIS OF THE FOLDABLE MODULE. IT CAN BE SEEN THAT THE MODULE SUFFERED SOME DAMAGE DURING MANUFACTURING (DARK AREAS). ALSO, SOME CRACKS WERE FORMED DURING LAMINATION AND THE CELLS THEMSELVES HAVE SOME DEFECTS THAT APPEAR AS IRREGULAR SPOTS. ....	67
FIGURE 66. OFFSET PANEL TECHNIQUE. ADAPTED FROM [56].NOTE THE OFFSET OF THE LOWER PANEL TO FORM A VALLEY FOLD. ....	68
FIGURE 67. COMMERCIALY AVAILABLE MINI MODULES FROM LINK LIGHT SOLAR. RETRIEVED FROM [57]. ....	71
FIGURE 68. SOUKO ROBOTS' PHOTOVOLTAIC PUZZLE CONCEPT. RETRIEVED FROM [58]. ....	72
FIGURE 69. SOLAR PUZZLE FISH DESIGN. TOP, IMAGE OF AN ISTIOPHORUS SPP. RETRIEVED FROM [59]. BOTTOM, DECOMPOSITION INTO GEOMETRICAL SHAPES. THE NAMES ASSIGNED TO EACH CELL IS ALSO SHOWN HERE. THESE NAMES WILL BE USED THROUGHOUT THIS CHAPTER. ....	74

FIGURE 70. CUT CELLS PRIOR TO SOLDERING AND ENCAPSULATION..... 74

FIGURE 71. INTERCONNECTION SCHEME. SOME LINES ARE DRAWN IN RED FOR CLARITY. .... 76

FIGURE 72. SOLUTION FOR BREAKING THE PARALLEL CONNECTION. WHEN A MAGNETIC CONTACT IS PLACED ON TOP OF THE BROKEN PAD, IT CLOSES THE CIRCUIT TURNING THE LOAD ON. THE REMOVAL OF ANY PIECE CAUSES THE CIRCUIT TO BECOME OPEN.... 76

FIGURE 73. ELECTRICAL DIAGRAM OF THE PUZZLE INTERCONNECTION. THE RED DOTTED CIRCLES INDICATE THE POINTS WHERE THE TRACKS ARE CONNECTED AS IN FIGURE 72. .... 77

FIGURE 74. FINISHED PV PUZZLE..... 77

FIGURE 75. ELECTROLUMINESCENCE PICTURE OF THE PV PUZZLE. CRACKS CAN BE SEEN IN THE WHOLE PUZZLE. HOWEVER, THEIR EFFECT IS SMALL. THE BIGGEST PROBLEM IS IN “SAIL 3” WHICH HAS A COMPLETE AREA IN BLACK. BECAUSE OF THE ALREADY EXISTING CURRENT MISMATCH, THIS BLACK AREA DOESN’T REPRESENT A BIG PROBLEM..... 78

FIGURE 76. IV CURVES OF THE INDIVIDUAL MINI MODULE PIECES. IT CAN BE SEEN THAT THE BIGGEST CELL “BODY 2” (THICK LINE) IS UNDERPERFORMING. THIS CAN BE CORROBORATED WITH THE ELECTROLUMINESCENCE PICTURE OF FIGURE 75. ALSO NOTE THE LARGE CURRENT RANGE. FROM CELLS PRODUCING LESS THAN 0.5 [A] TO CELLS THAT ALMOST TRIPPLICATE THE SMALLER ONES. .... 79

FIGURE 77. IV CURVES OF THE WHOLE PUZZLE WHEN EACH INDIVIDUAL PIECE IS REMOVED. FOR CLARITY, NOT ALL OF THE PIECES ARE SHOWN HERE. THE IV CURVE OF THE WHOLE PUZZLE IS SHOWN AS A DASHED LINE. HERE IT CAN BE SEEN THAT THE PIECE “SAIL 2” IS LIMITING THE CURRENT. WHEN IT IS REMOVED THE CURRENT RISES. SINCE IT IS IN SERIES, ITS REMOVAL ALSO CAUSES A VOLTAGE DROP. THE OPPOSITE OCCURS WITH “SAIL 4”. THIS CELL IS CONNECTED IN PARALLEL, SO THE VOLTAGE DROP IS BASICALLY NULL. IT IS CONNECTED TO A SMALL PIECE; THEREFORE, REMOVING IT LEAVES ONLY THE SMALL PIECE IN SERIES. THIS LIMITS THE CURRENT. THE PIECE “CELL 2” THAT IS UNDERPERFORMING CAUSES ONLY THE CORRESPONDING VOLTAGE DROP. IT IS ALSO AN INDICATOR THAT THE CURRENT OF THIS CELL IS BEING LIMITED..... 80

FIGURE 78. PV CURVES OF THE WHOLE PUZZLE WHEN EACH OF THE PIECES IS REMOVED. ANALOG TO THE IV CURVES, REMOVAL OF LARGE PIECES CAUSE A SIGNIFICANT DROP IN POWER. EVEN “BODY 2” THAT IS UNDERPERFORMING HAS AN IMPORTANT ROLE IN THE ARRAY AS THE POWER IS GREATLY REDUCED WHEN THIS PIECE IS MISSING. AS BEFORE, THE REMOVAL OF “SAIL 4” LEAVES ONLY THE SMALL CELLS IN SERIES LIMITING THE WHOLE ARRAY CURRENT..... 80

FIGURE 79. EFFECT ON THE EFFICIENCY CAUSED BY REMOVING EACH INDIVIDUAL CELL. AT FIRST SIGHT, IT WOULD SEEM THAT THE REMOVAL OF “TAIL DOWN” INCREASES THE PUZZLE EFFICIENCY. CARE SHOULD BE TAKEN WHILE INTERPRETING THIS. .... 81

FIGURE 80. SCHEMATIC DIAGRAM FOR THE BUCK CONVERTER..... 92

# List of Tables

TABLE 1. RECIPE FOR THE LAMINATION OF MINI MODULES. TAKEN FROM [15] WITH A MODIFICATION IN THE COMPRESSING PRESSURE. THE ORIGINAL WAS 150 [MBAR]. FOR FRONT SHEET, THE PRESSURE IS BETTER AT 200 [MBAR].	7
TABLE 2. OPTIMAL CUTTING PARAMETERS FOR AN AKW C-SI AL-BSF. CUTTING FROM THE BACKSIDE WITH A LASERGRAAF 30 [W] FIBER LASER.	23
TABLE 3. VALUES OF THE PERIMETER-TO-AREA RATIO OF REGULAR FIGURES. ALL REGULAR FIGURES, IRRESPECTIVE OF ITS DIMENSIONS WILL HAVE THESE VALUES. SINCE THE RECTANGLE IS NOT A REGULAR FIGURE, A FIX VALUE OF $\rho$ CANNOT BE ESTABLISHED. HENCE IT IS OMITTED FROM THE TABLE	28
TABLE 4. COMPARISON OF 2 EQUAL-AREA SHAPES WITH DIFFERENT SHADING FRACTION. FOR A SAME FIGURE, THE LAYOUT WITH LESS BUSBAR LENGTH RESULT IN A CONSIDERABLE INCREASE IN EFFICIENCY. EVEN MORE, THE SHADED FRACTION PLAYS A MORE IMPORTANT ROLE THAN THE PERIMETER-TO-AREA RATIO.	31
TABLE 5. SUMMARY OF EVALUATED GAINS AND LOSSES OF THE REFERENCE MODULE. THE NEGATIVE SIGN INDICATES AN IMPROVEMENT OF EFFICIENCY OR POWER AS ARE VALUES ABOVE 1.	49
TABLE 6. COMPARISON OF THE INACTIVE AREA LOSS FACTOR OF A TRAPEZOID CELL VS A SQUARE CELL.	60
TABLE 7. COMPARISON OF THE CTM FACTORS OF THE REFERENCE MODULE OF SECTION 1.4.5 AND THE FOLDABLE MODULE PROTOTYPE. THE NUMBERS REFER TO THE $K_1$ FACTORS AND ARE DIMENSIONLESS. A HIGHER NUMBER INDICATES THAT THE LOSSES ARE LOW. FOR INSTANCE, THE FRONT SHEET REDUCES THE REFLECTION LOSSES IN COMPARISON WITH GLASS, BUT HAS ALSO A GREATER ABSORPTION LOSS.	65
TABLE 8. EXTERNAL PARAMETERS OF THE FOLDABLE MODULE.	66
TABLE 9. FULFILLMENT OF REQUIREMENTS.	73
TABLE 10. PARAMETRIZATION OF THE SINGLE CELL MODULE.	75
TABLE 11. . LASERGRAAF TECHNICAL SPECIFICATIONS. RETRIEVED FROM [32].	91
TABLE 12. LOSS AND GAIN FACTORS AS DEFINED BY HAEDRICH <i>ET AL</i> [22].	91



# List of abbreviations

AKW	Manufacturer of solar cells
Al-BSF	Aluminum Back Surface Field
BIPV	Building-Integrated Photovoltaics
c-Si	Crystalline silicon
CTM	Cell-To-Module
ECA	Electrically conductive Adhesive
EQE	External Quantum Efficiency
EVA	Ethyl Vinyl Acetate
FF	Fill Factor
IMPP	Current at the maximum power point
IV curve	Current vs Voltage curve
LASS	Large Area Solar Simulator
LED	Light Emitting Diode
MPP	Maximum Power Point
MWT	Metal Wrap-through
PIPV	Product-Integrated Photovoltaics
PV	Photovoltaic
PV curve	Power vs Voltage curve
RGB	Red Green Blue
STC	Standard Test Conditions
VMPP	Voltage at the maximum power point



# List of symbols

$f$	Frequency
$I_{sc}$	Short circuit current
$k$	Perimeter-to-area ratio
$k_j$	$j^{\text{th}}$ loss mechanism element
$n_i$	Refractive index of the $i^{\text{th}}$ medium
$\rho$	Perimeter-to-area ratio (dimensionless)
$R_{bb}$	Shaded fraction due to busbars
$R_s$	Series resistance
$T_{on}$	Pulse duration
$V_{oc}$	Open circuit voltage





# 1

## Introduction

The lack of space in modern cities limits the amount of photovoltaic power that can be installed in these places. This can slow down the development of new projects in such areas which can potentially benefit small consumers or common people.

Building Integrated Photovoltaics is already focusing on deploying solar power on urban environments. Focusing on the already mature c-Si technology of solar cells allows new products to quickly become available to the customers.

On the other hand, a relatively new branch of design is focusing on the integration of solar energy into products in the so-called Product Integrated Photovoltaics. While the technology used in this area are thin-films, potential for c-Si should also be investigated.

Custom-sized modules, non-conventional shapes, connection schemes and new applications for solar modules will be explored in this work while trying to answer the following questions.

- What is the effect of cutting a c-Si solar cell into different shapes and sizes?
  - Does the laser cutting process have a significant effect in the efficiency?
  - Is there a shape that leads to a better performance?
  - Can solar cells be cut into very tiny pieces?
- How does the Cell-To-Module ratio behave within small-sized modules?
  - Can the same approach as commercial-sized modules be used?
- Which innovative interconnection schemes can be used for PV modules?
  - How does a conductive adhesive affect the performance of the cell?
  - Does the use of magnets have a significant impact on the cell's output?
- How can a mini-module help with the integration of PV power into daily life activities?

In order to tackle these questions, a brief overview of how solar energy is being integrated into daily activities will be presented in Section 1.1.

The used methodology and an explanation of the used setups is mentioned in Chapter 2.

Before discussing the mini modules, it is necessary to understand how different geometries and sizes can be obtained. This is discussed in Chapter 3. Laser cutting will be first introduced in Section 3.1. Then, the effect of cutting the cells into smaller sizes and different shapes will be discussed in Section 3.2.

Chapter 4 discusses mini module construction by explaining the Cell-to-Module conversion ratio (Section 4.1) while Section 4.2 will focus on the electrical contacts that are proposed.

To demonstrate all the concepts two prototypes were fabricated. The first one is an Origami based foldable module, presented in Chapter 0. The second one is a photovoltaic puzzle as explained in Chapter 1.

Each chapter ends with a conclusion and an overview of the path that must be followed to obtain a fully working product. Finally, the overall Conclusions and recommendations are presented in Chapter 7.

## 1.1. PV in everyday life

### 1.1.1. Building Integrated Photovoltaics (BIPV)

The integration of solar energy into the urban environment has found way in the so-called *Building integrated Photovoltaics* -or BIPV-. This technology allows to replace constructive elements of a building with photovoltaic modules. The key of BIPV is that it is completely embedded into the building envelope. In this way, part of the façade, roof or windows can be totally substituted with photovoltaic products [1]. Hence, BIPV serves as a structural element and an energy generation source [2].

At this point it is convenient to distinguish between BIPV and BAPV (*Building Attached Photovoltaics*). While the former *substitutes* parts of the building's structure, the latter is only added to it. Therefore, its only purpose is energy generation and not the double function as the BIPV [2, 3]. However, sometimes the boundary between the two concepts is not clear and the term *BIPV* is often used indistinctly.

Cerón, *et al* [2], discusses that there are two main ways to achieve BIPV. First, as *PV modules* especially designed to meet the architectural constraints; second, as *constructive elements* that are designed since its inception with PV generation capabilities embedded within construction materials. They can be classified into four groups which are

- *Roofs*
- *Façades*
- *Urban furniture*
- *Custom design*

In 2012 the BIPV market was mainly dominated by constructive elements which constituted a 56% of the total. The BIPV modules accounted for the rest. Within the constructive elements, the roofing systems constituted the majority (46.6%), followed by urban furniture (31.7%), façades (11.6%) and custom designs (10%) [2]. In 2017 the University of Applied Sciences and Arts of Southern Switzerland (SUPSI) in conjunction with the Solar Energy Application Centre of The Netherlands (SEAC) [4] reported that the PV roofing is still dominating by number of products available on the market.

The reason for the growth of BIPV is that it allows to implement a *greener* image on the cities, therefore having a high social impact and acceptance. Nowadays is easier to spot small stand-

alone systems, such as public lighting, that serve as a proof of the positive image that the solar energy generates not only energy but a better image in the urban environment [2].

In order for a BIPV product to be successful and useful it must not also be able to generate energy, but it has to be attractive to architects and public. In this matter, Cerón *et al* [2] mentions that the ability to easily connect several modules and adapt them to the architectural constraints (i.e. *modularity*) is a key factor on the acceptance of new products. In fact, the same author sets a requirement of modules whose dimensions are multiple of 100 [mm]. Thus, allowing its easy integration onto the building.

One of the major focus of the BIPV products is to become aesthetically pleasant. While roof products are chosen to be black and opaque [2], façade modules do not necessarily need to attach to this constraint. Coloured or patterned modules become then important players on the market. An example of this products is a module that uses small Metal Wrap Trough (MWT) cells to create a mosaic pattern. The use of small solar cells reduces the resistive losses and, at the same time, allows different visual effects. Furthermore, a conductive layer between the cells and the copper base (used for connections) can be coloured enhancing the visual effect [5].

A different approach that makes use of the MWT cells was proposed in [6]. Here, coloured dots were placed on top of the solar cells. When looked in the distance, the cells are practically invisible and only the image created by the dots is visible. Since the dots cover active areas of the cells, reducing the power output, an algorithm was used to optimize the dot placement while trying to minimize the power losses.

### 1.1.2. Product Integrated Photovoltaics (PIPV)

The actual interest of using decentralized energy sources has leaded designers to include renewable sources in everyday life. In order to achieve so, solar photovoltaic technology offers a good solution. What is more, this technology is the only one that allows a complete integration into products without sacrificing its esthetic appearance [7].

Current large-scale technology based on rectangular PV modules is not suitable for PIPV applications as it is sturdy and rigid. This prevents its correct integration on curved surfaces. Their size can exceed the product's dimension and they can be esthetically unattractive and even unpleasant. Even more, they do not allow customization in terms of shape and size which is a property often looked by designers [7].

In 1978 the idea of integrating PV in a common-citizen life was successfully achieved with the invention of the solar calculator. From that point onward, and especially during the 2000's, the area of PIPV experienced a rapid growth. It has found its way into different applications such as watches and other consumer products, lighting –with lamps powered by solar modules-; urban furniture as trash compacters, recreation and leisure activities (in the form of solar powered motor homes or camping lights); transport (as prototype vehicles or planes) and, surprisingly, arts (mainly as decorative elements and sculptures) [8]. The integration of

photovoltaics into products can also be used in relief operations as the product proposed by Findeisen, *et al* [9], which incorporates thin film modules onto an inflatable refugee tent.

For a product to be considered in the category of PIPV, some requirements should be met as enlisted by [8].

- The PV element should be on the surface or casing of the product.
- The product must use the energy generated by the PV element.
- A user must be able to directly use the product or interact with it.
- The device must be easy to transport.

One way to achieve this is by using thin-film technology as this technology allows to be bended and it allows to mimic the solar cells; thus, enhancing esthetics. Furthermore, with a proper process, thin films can be manufactured in a variety of shapes and sizes. This fulfills the requirements of designers that are looking for custom-made products [7].

A considerable number of PIPV devices are used indoors. This adds an additional challenge because the solar cells are characterized under *Standard Test Conditions* (STC). These conditions represent a reference for comparing the performance of the cells *outdoors*, mainly because they use the spectrum of the Sun (AM1.5 spectrum). However, cells that are used indoors experience a different spectrum. Namely, one that is composed by natural light and artificial sources. While the natural light also comes from the sun, it is mainly diffuse or scattered light. The windows and possible glazing may act as filters, changing the spectrum that the cell receives. Furthermore, the spectrum of artificial sources depends on the technology that is used [10]. This adds to the fact that the available irradiance is also less. In comparison with a winter cloudy day outdoors where the irradiance can reach values up to 100 [W/m<sup>2</sup>], the available irradiance indoors is 10 to 100 times less that value. For this reason, PIPV that is intended for indoors can only be used to feed low power devices [11].

PIPV opens new market opportunities. In an analysis made by Satpute, et al [12], they analyzed the potential market applications from the perspective of human needs. The Maslow hierarchy of needs was used. This hierarchy enlist how people satisfy their needs. The first elements in the hierarchy are the most important (Physiological ones). Once they are satisfied, the individual climbs up to a higher level. This hierarchy is as follows [13] .

1. Physiological – food, water, air...
2. Safety – (shelter, security, health...)
3. Love and belonging (friends, family...)
4. Self-esteem – achievement, recognition, status
5. Self-actualization – personal growth

The majority of commercially available PIPV products aim at the “Safety” level of the hierarchy while few aim to be used to satisfy the basic needs (physiological). Nevertheless, the authors of the study concluded that the potential market of PIPV lays in products that aim at the “Love and belonging” and “Self-esteem” needs [12].

# 2

## Methodology

This chapter aims to describe the equipment used in each experiment. A brief introduction to the working principle of the machines is given. Also, the procedure followed for each experiment is explained

### 2.1. Overview of the equipment used

#### 1.2.1. Lasergraaf laser cutter

A fiber laser is a kind of laser cutter that makes use of a fiber optic to transport the light beam, typically 1070 [nm], from the source to the output [14]. The laser is then directed via mirrors to a  $\theta$ -lens. This lens allows an even distribution of the beam focus in the whole plane, rather than only in a single point [15]. For the experiments, a Lasergraaf 30[W] fiber laser “Emma” was used.

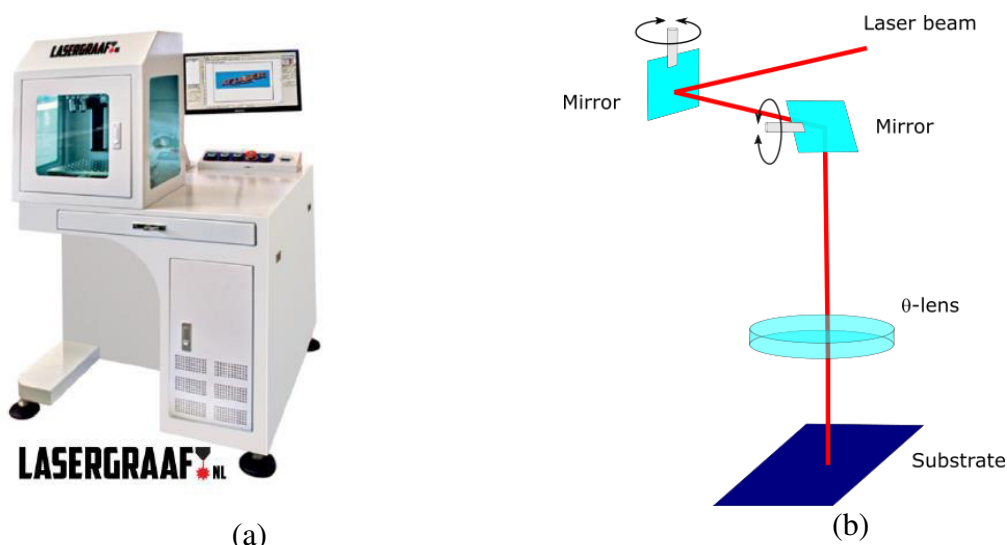
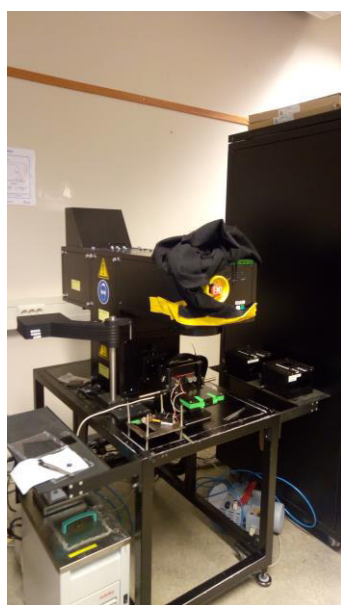


Figure 1. (a) Lasergraaf laser cutter. (b) Operating principle of the machine. The whole figure was adapted from [15].

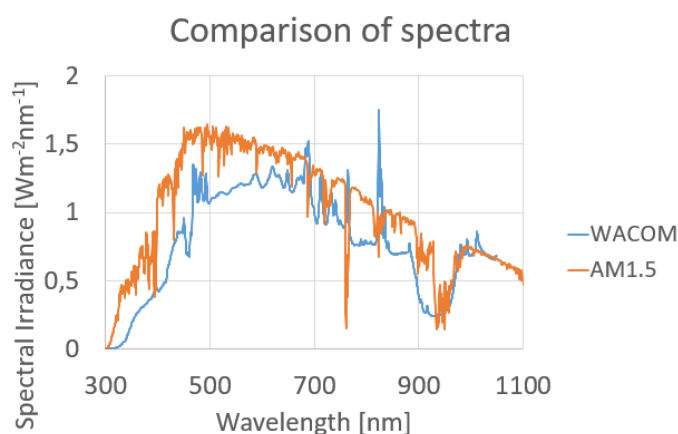
### 1.2.2. WACOM solar simulator

Solar simulators offer a good way to measure the performance of the solar cell. They provide the irradiance for measurements of the IV curve under near *Standard Test Conditions* (STC) by matching the spectrum of artificial sources with the spectrum of the Sun (AM1.5).

The used simulator was a WACOM WXS-90S-L2. This is a class AAA simulator that generates the spectrum using a xenon and a halogen lamp [16]. Figure 2 (a) shows the setup held at TU Delft. Figure 2 (b) shows the spectrum of the device and compares it to the spectrum of the Sun.



(a)



(b)

Figure 2. (a) WACOM solar simulator at TU Delft. (b) Comparison of the spectra of the WACOM and AM1.5. Plotted with data from the PVMD group at TU Delft.

### 1.2.3. PASAN flash tester

Analog to the WACOM simulator, the PASAN flash tester provides the illumination for during the sweeping of the IV curve. However, instead of a continuous illumination as WACOM, a 4.5 [ms] *flash* is fired upon the sample and the IV is swept during this period [17]. Measurements using the flash tester are faster than WACOM and without the inconvenient of temperature rise. However, the flash is produced with a single lamp. Therefore, the spectrum differs from AM1.5. Especially in the infrared section of it.

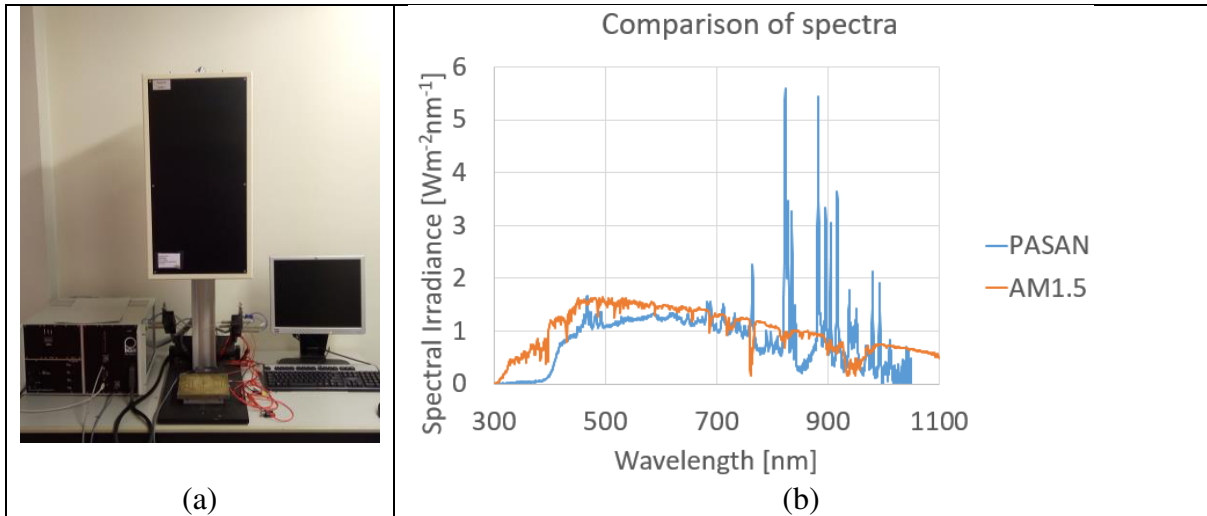


Figure 3. (a) PASAN IId flash tester held at TU Delft. (b) Comparison of the spectra of PASAN and AM1.5. Note the large peaks in the infrared section. Plotted with data from the PVMD group at TU Delft.

#### 1.2.4. EXPERIA laminator

The lamination of modules is a process in which the solar cells are encapsulated between glass (or foil) and a supportive back sheet (glass or foil). An *encapsulant* is used to glue all the components of the stack together. Heat is applied to the encapsulant (ethyl vinyl acetate (EVA)) to melt it followed by pressure that keeps all the stack in place. Once the EVA has cured, pressure is released and the module is encapsulated.

A good lamination must be free of air bubbles inside the encapsulant, no broken cells and no weak corners that can lead to de-lamination [18].

For this purpose, an EXPERIA Laboratory Laminator LAM600 was used. This machine allows the user to program a recipe. For the manufacturing of mini modules, the recipe found by Villa [15] was also used and is reproduced in Table 1.

Process	Time [s]	$p_{\text{up}}$ [mbar]	$p_{\text{down}}$ [mbar]	$T_{\text{set}}$ [ $^{\circ}\text{C}$ ]	Pins
Evacuating	120	0	0	80	Up
Heating up	500	0	0	140	Up
Compressing	60	150-200	0	140	Down
Curing	500	900	0	145	Down
Venting	30	0	1000	145	Down
Release	30	0	1000	145	Up

Table 1. Recipe for the lamination of mini modules. Taken from [15] with a modification in the compressing pressure. The original was 150 [mbar]. For front sheet, the pressure is better at 200 [mbar]



Figure 4. EXPERIA Laminator. Taken from [18].

### 1.2.5. LAMBDA spectrometer

A LAMDA 950 spectrophotometer, manufactured by Perkin Elmers, allows the optical characterization of the glass, encapsulant and transparent foils used in this work. It makes use of an integrating sphere covered with a highly reflective material and two detectors on its walls. Each of the two detectors will cover a part of the spectrum. For the Near Infrared (NIR) part a lead sulphide (PbS)-based sensor with a resolution of 0.2 [nm] is used. This sensor covers wavelengths from 860.6 [nm] and above. For the UV/vis range of the spectrum a photomultiplier tube is used. It operates for shorter wavelengths up to 860.6 [nm] with a resolution of 0.05 [nm]. At the mentioned wavelength of 860.6 [nm], the equipment switches from the PbS to the photomultiplier tube [19].

Placing the sample before the integrating sphere allows the determination of the transmittance, while in the back, of reflectance.

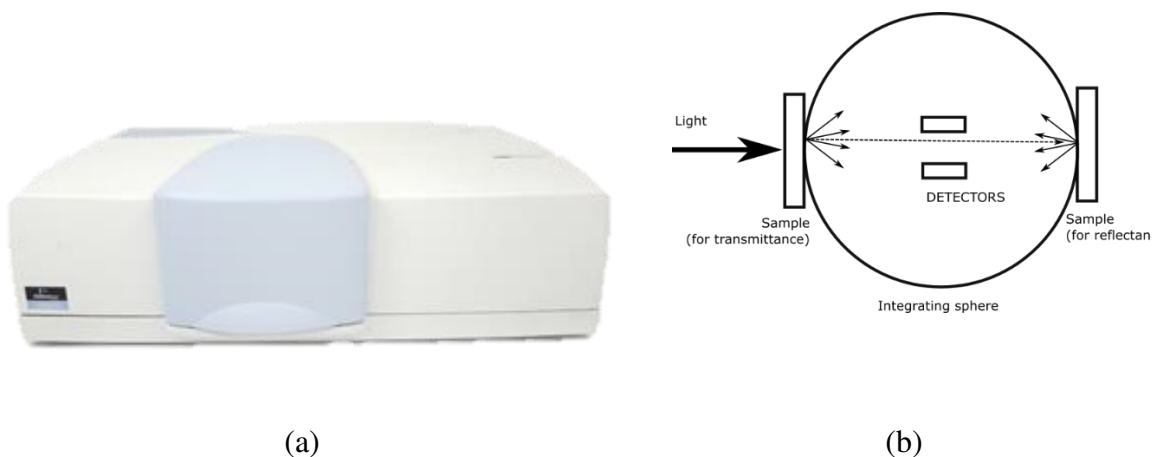




Figure 5, LAMDA 950. Retrieved from [20] .(b) working principle of the integrating sphere. Only transmittance or Reflectance can be measured at a time. Adapted from [19].

### 1.2.6. Solar simulators SASS and LASS

The Large Area Solar Simulator (LASS) manufactured by EXASUN provides a near AM1.5 spectrum and is suitable for measuring commercial-sized modules. It provides an automatic sweep of the IV curve.

The Small Area Solar Simulator operates in an analogue way as the LASS but for a smaller area. The disadvantage of this setup is that the simulator only provides the illumination. The IV sweep has to be done manually. In order to do this, an electronic load was used to sweep the IV curve while two multimeters will give the readout of voltage and current. The diagram of Figure 6 better illustrates this.

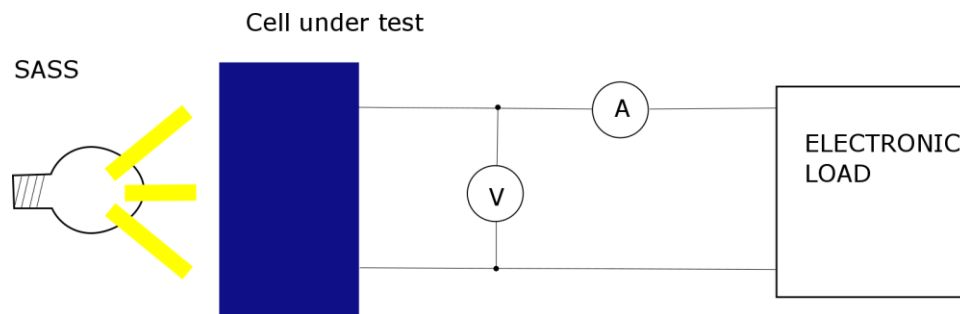
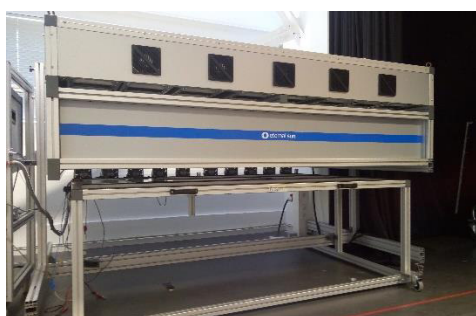


Figure 6. Experiment setup for the measurement of the IV curves for the pieces of the PV puzzle using a manual sweep.



(a)



(b)

Figure 7. LASS (a) and SASS (b) held at the PV laboratory of TU Delft.

## 2.2. Laser cutting

The experiments related with the laser cutter involve the determination of the laser cutting parameters, the effect of cell shape and the effect of cell size.

To do this, commercially available c-Si solar cells with Al-BSF were used as substrate. For the laser cutting experiment, the cells were manufactured by AKW solar (kindly given to TU Delft by *Kameleon Solar*). These cells have three continuous busbars on the front and three rows with three soldering pads each. The manufacturer does not provide a very accurate datasheet, but with the information available [21], the cells have an efficiency of 20.4% and its output power is 4.95 [W] at maximum power point. The other external parameters are a short circuit current of 9.61 [A] and an open circuit voltage of 0.654 [V]. Each cell is a semi square with a standard size of 15.6 x 15.6 [cm].

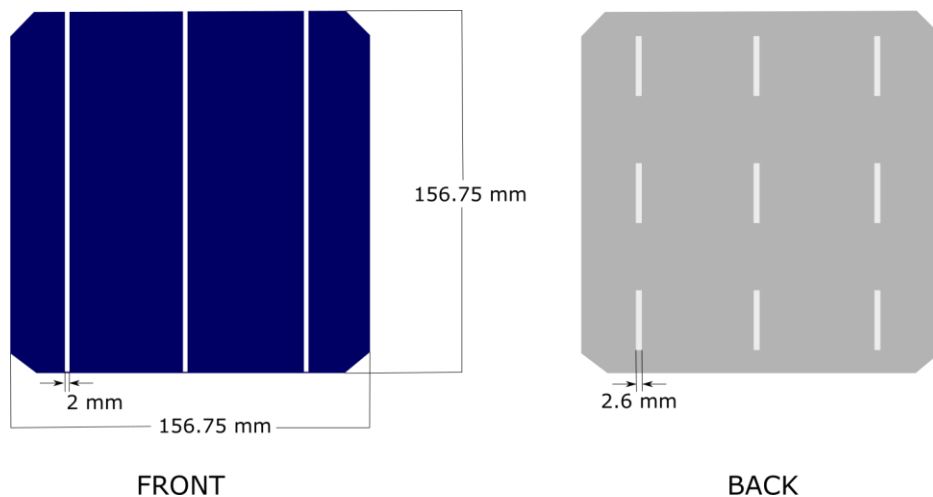


Figure 8. Schematic of an AKW cell. Adapted from [21].

### 2.2.1. Parameter estimation of the Lasergraaf cutter

The Lasergraaf laser cutter does not have an automatic focus function and it must be manually adjusted. The indicator of focus is a laser pointer that should overlap with the main laser pointer. However, the focus must be first set, then the indicator can be fixed. As the height of the cutting table changes, the focus might be lost. Thus, causing the two pointers to separate.

In order to determine the focus a hatched square was marked. The height of the table was manually adjusted during the marking until a bright light and a clear sound was observed.

The procedure was repeated for several times or every time there was a reason to believe that the machine was out of focus. After different adjustments, the settings were found to be the same.

Several cuts were performed varying all the parameters, starting with the pulse within the picosecond range and then increasing it to the nanosecond range, then the repetitions, frequency and finally, speed. The cells were first marked and then mechanically cleaved.

In all cases, only cells *within* the wafer were used. In other words, the edges of the original cell were discarded. This in order to fully understand the laser effect.

The parameters were varied, and the cut cells were measured under the WACOM solar simulator in near Standard Test Conditions (STC). The cell efficiency was the parameter used to determine the correct tuning of the machine.

Since there are four parameters, three of them could be kept constant varying the remaining one and then, repeating the procedure changing the variable parameter. In order to reduce the useful results, every combination that resulted in no cut, cell breaking and cell bending during the process or completely cut through was discarded.

Once a clean mechanical cleavage was obtained, a complete cell was randomly scribed with the potential parameter candidates. The cell that leads to the highest efficiency is then the one with the optimal parameters.

Note, that in all cases, the cell size was kept constant.

### 2.3. Shape and size

In order to determine the effect of the cell area, a 15.6 x 15.6 cm cell was measured using a PASAN flash tester. Afterwards, the cell was cut in half using the laser parameters obtained before. Both parts were measured again. Each half was cut once more time in half (quarter cells). The process was repeated until an area of 1 [cm<sup>2</sup>] was obtained. A schematic of the experiment can be appreciated in Figure 9. Note that the quarter cells can be cut either vertically or horizontally.

The vertical quarter cells are cut through the middle of the busbar.

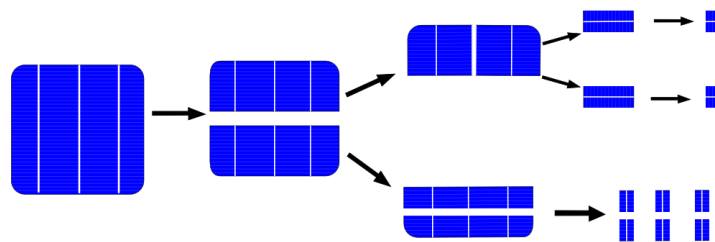


Figure 9. Cell size experiment

For the effect of the cell shape, a full cell was cut into different geometries. Namely circles, hexagons, equilateral triangles; squares and rectangles. The orientation of the long side of rectangles was chosen in such a way that the busbars would have different lengths for the same area (Figure 10).

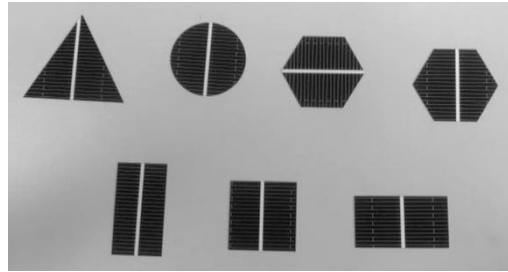


Figure 10. Cut cell shapes. The two hexagons, as well as the two rectangles, shown here have exactly the same dimensions. Note that the busbars in these figures can have different orientation.

The triangles (Figure 11) were also cut into different sizes in order to compare the effect of both, shape and size. For the hexagons, the same procedure was done. Note that in Figure 12, the busbars are not centered. This is because the laser cutter has a misalignment between the cutting beam and the desired marking path that is commanded in the laser software. The misalignment is further increased by the fact that the front and back contacts of the cell do not necessarily match. Since the cell is cut from the back, the alignment becomes a trial and error process.

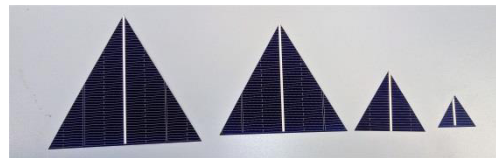


Figure 11. Cut equilateral triangles

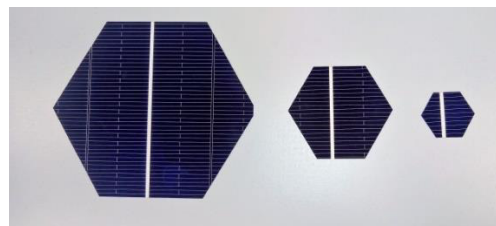


Figure 12. Cut hexagons. The displacement of the busbar is a result of a misalignment of the laser beam with respect to the desired marking path and the fact that the back contact does not align perfectly with the front one. The cells were cut from the back.

All cells were measured using a PASAN flash tester.

## 2.4. Cell-To-Module ratio

The procedure for measuring the Cell-To-Module CTM gains and losses was adapted from Haedrich, *et al* [22]. The optical properties of a CORNING glass 0.7 [mm] thick were determined.

A piece of Ethylene Vinyl Acetate (EVA), which functions as an encapsulant, was melted and laminated with the EXPERIA laminator. Then, a sample consisting of one layer of Corning glass together with a piece of EVA were laminated together. Both samples were optically characterized.

For each sample, the reflectance and transmittance were measured and from the collected data the absorptance of each material was determined with Equation (2-1).

$$A = \log_{10} \frac{T}{R} \quad (2-1)$$

Where  $T$  is the measured transmittance and  $R$  the measured reflectance.

The optical coupling of the EVA was determined by measuring a 9 [cm<sup>2</sup>] cut from a 15.6 [cm] AKW cell using the laser parameters of Table 2. Standard tabbing wire was soldered at the contacts of this cell. After that, the IV curve was traced for the cell.

Afterwards, it was encapsulated. The composition of the stack was Corning glass-EVA-solar cell-EVA-*black* back sheet.

A similar setup was used for determining the optical gain due to reflection of the back sheet. In this case, a single cell module was fabricated, encapsulating a cut 9 [cm<sup>2</sup>] AKW cell with a white back sheet. Using a custom-made mask, the module was measured varying the aperture area.

To measure the resistive losses, the IV curve for individual 9 [cm<sup>2</sup>] cut cells was measured. Then the cells were soldered in series using standard tabbing wire. The separation between cells was aimed at 3 [mm]. A string consisting of three cells was then measured. With this procedure, the interconnection losses were studied.

The losses of the string connection are determined by measuring the IV curve of individual strings before the connection and after it. This was done with a 4 [mm] width standard tabbing wire.

Finally, a full mini module consisting of six 9 [cm<sup>2</sup>] cut cells was fabricated with a 10 x 10 [cm] Corning glass, EVA and a white back sheet. This module was measured again and used as a reference.

The measurement of all the IV curves in this section was done using the WACOM solar simulator. The optical characterization of the corresponding samples was done with the LAMBDA setup while the lamination with the EXPERIA laminator.

## 2.5. Prototypes

The prototypes were fabricated using standard 15.6 [cm] Viko solar cells and laminated using an EXPERIA laminator. In the specific case of the photovoltaic puzzle, once the cells were laminated, molds were prepared of MDF in order to pour silicone rubber (RESION RS1040AB, Polyestershoppen.nl). Commercially available magnets were used as contacts.

After lamination, an electroluminescence test was done to check the functionality and potential cracks of the products.

An electrically conductive copper tape (Manufactured by 3M) was used as connecting element within the PV puzzle and the foldable module. Experiments to determine the resistance of the tape were done using standard tabbing wire and a piece of electrically conductive adhesive tape (3M). First, the resistance of the tabbing wire was measured using a bench multimeter. Then, the copper tape. The copper tape was then cut in two. Using the adhesive, both pieces were joined again and the resistance measured again. It must be noted that in all cases, the magnets were used as contacts.

The procedure was repeated for three pieces and for a single piece with two terminals on top forming a “T” as shown in Figure 13 (c).

Finally, the two copper tape pads were made by joining stripes of tape forming a wider copper pad. Magnets were placed randomly at different points of this pad and the resistance measured again. The whole setup can be best understood by looking at Figure 13.

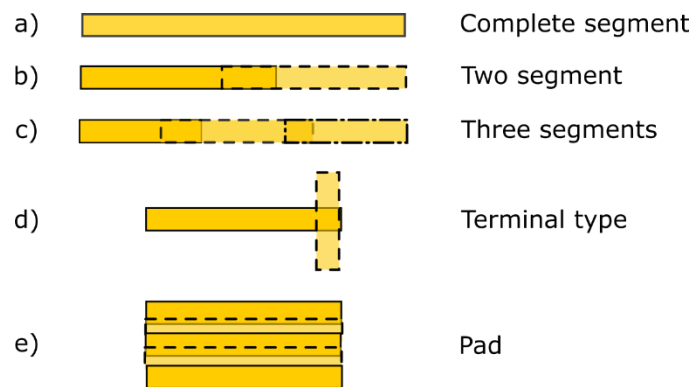


**Figure 13.** Patterns used for measuring the resistance of the copper tape. First, a complete segment was measured (a). Then, two tape segments were glued together (b). An analog procedure was done with three tape segments (c). The terminal type of (d) refers to the configuration used for the PV puzzle, while (e) shows the pad built for measuring the individual pieces of the PV puzzle.

The copper pads were then used to manually sweep the IV curves of each individual piece. In order to do so, each piece was connected to the pads using its magnets. The connection was placed under a *small area solar simulator (SASS)*, again under near STC.

# 3

## Creating custom shapes

### 3.1. Solar cell cutting

#### 1.3.1. Laser cutting

A high-energy laser beam can be used to modify the physical properties of a substrate by increasing its temperature. When the *laser conduction limited heated* is used, the substrate is only heated but it does not melt. In contrast, in the *non-conduction limited heating*, the substrate does not remain solid anymore. Depending on the application, one method or the other must be used. For instance, quenching requires conduction limited heating. Cutting, drilling and welding are examples of applications of non-conductive limited heating [23].

The operating principle of laser cutting is based on melting and evaporation of a substrate using a high-energy laser beam. This beam is irradiated onto a substrate. In return, the material will absorb part of the beam energy. Because this absorption and the high energy density in a reduced area, the substrate will rapidly heat-up. This causes melting and ultimately, evaporation of the irradiated surface. A pressure force will act on the liquid as the vapour leaves the material. This pressure will increase the evaporation rate even more. The combination of evaporation and pressure results in cavity formation [23].

The pulse duration of the incident laser defines how the cavity is formed. This is because, not only vapour but also liquid can be expelled from the cavity when pulses in the millisecond range are used. For pulses lasting only nanoseconds, there is no liquid ejection and the cavity forms mainly by the pressure of the vapour acting upon the liquid. In either case, using a jet of gas can improve the cutting by removing material and debris from the cavity [23].

The laser machines can be classified in two operating modes

- Continuous wavelength laser. A single laser ray is fired onto the substrate.
- Pulsed lasers. A pulse train is irradiated on the material
  - Q-switched. As the name implies, a switch is used to block the laser beam, thus producing a pulse train [16]. A Q-switched laser only allows tuning of the pulse frequency keeping the pulse length constant.
  - Master Oscillation Power Amplifier (MOPA). Is an upgrade of the Q-switched laser which allows tuning of pulse frequency *and* duration [24].

Figure 14 shows a schematic of the laser pulses and the main parameters  $T_{on}$  [ns] and frequency ( $f$ ) [kHz]

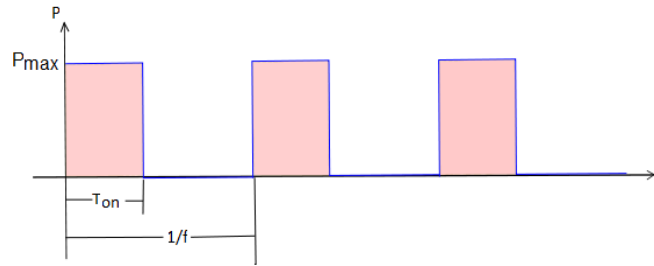


Figure 14. Laser pulses. The area of each pulse is the energy of the pulse  $E_p$ .

Adjusting the pulse parameters makes it possible to set-up the energy of the laser in order to obtain an optimal cut. The amount of energy irradiated in an area given by the radius ( $r$ ) of the spot is the so-called *laser fluence*, with units [ $J/cm^2$ ] [25]. In other words, the fluence  $\phi$  is given by Equation (3-1).

$$\phi = \frac{E_p}{\pi \cdot r^2} \quad (3-1)$$

And the average pulse energy  $E_p$  is simply the average power  $P_{avg}$  divided by the pulse frequency [16].

$$E_p = \frac{P_{avg}}{f} \quad (3-2)$$

The spot size is partially determined by the focus of the laser. Considering Equation (3-1), it can be stated that the focus has a major impact on the fluence.

### 1.3.2. Laser induced damage

A cell whose PN junction extends fully to the edges, which is true for most commercial cells, may be modelled by the circuit (Figure 15) proposed by McIntosh *et al* [26].

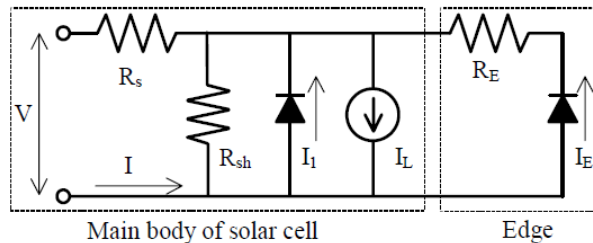


Figure 15. Equivalent circuit of a solar cell considering the edges. A second diode  $IE$  is added to account for recombination losses at the edge.  $RE$  represents the distance from the main body of the cell to the edge; thus, separating the two parts. Retrieved from [26].



The diode  $I_E$  represent the recombination current at the edges, while the resistor  $R_E$  is separating the main body of the cell from the edge. Furthermore, the edge is modelled as a diode since the edge recombination current is not linear but *exponential* and dependent on the voltage [26].

Commercial solar cells have their edges passivated in order to reduce the edge recombination. It is possible to observe with optical microscopy (Figure 16) that the edge is a smooth surface. A mechanically broken cell with no laser used produces a profile as shown in Figure 17. Here, the profile is also a smooth surface. Some irregularities can be observed in the back of the cell which are probably caused by the attachment of the aluminum back contact.

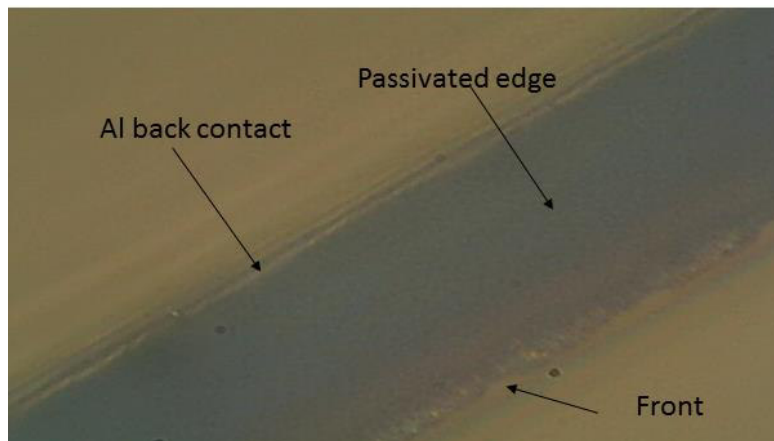


Figure 16. Optical microscopy of the side of an uncut c-Si cell. Note that the edge appears smooth.

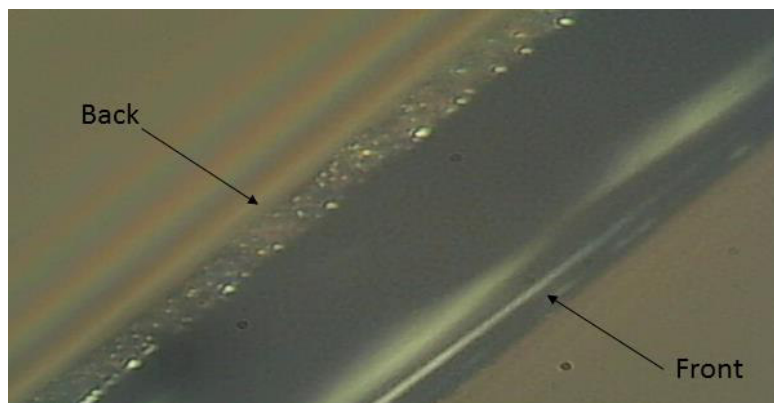


Figure 17. Optical microscopy of the side of a broken c-Si cell. The edge is still smooth.

The different illuminated IV curves for different laser parameters strongly suggest that the laser modifies the structure of the cell. Although the short-circuit current  $I_{sc}$  remains almost the same for various configurations, the open-circuit voltage  $V_{oc}$  and Fill Factor  $FF$  exhibit a greater variation. The latter is mostly responsible for the changes in efficiency.

As the material melts because of the laser, shunts are created through the P-N junction, especially when the process is performed on the front side of the cell [27]. These shunts reduce the parallel resistance  $R_{sh}$  of the cell. Nevertheless, the main cause of efficiency loss is not because of the shunts themselves but an increased saturation current  $I_E$  [28] as a result of the lattice being completely disrupted at the edges. This disruption plays a major role in the

reduction of efficiency. Moreover, additional shunts may be avoided if cutting the cell from the back [27].

McIntosh *et al* [26], also concluded that the edge recombination is responsible for a lower Fill Factor, partially because of a reduction in the open-circuit voltage as the recombination increases.

In order to illustrate the damage caused by the laser, an optical microscopy picture was taken as can be seen in Figure 18. The surface is not smooth anymore in comparison to Figure 16 nor Figure 17 but completely irregular as a result of the melting process. The footprint of the laser can be even appreciated. The cell is mechanically cleaved after the laser scribing. This is the reason for a smooth surface in part of the cell.

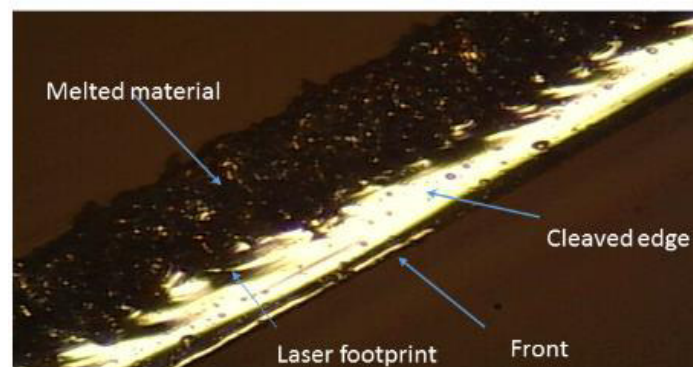


Figure 18. Optical microscopy of a laser cut cell. Note that the effect of the laser becomes clearly visible and that the edge is not smooth anymore but rough. The remaining part (cleaved) is still smooth.

## 3.2. Cell shape and size

The first step to create custom shaped cells is cutting them. From Section 1.3.1 it can be concluded that the laser is a versatile and relatively inexpensive tool to produce custom shapes from commercially available solar cells. However, their performance might be reduced as the process itself damages the cell. Therefore, in order to achieve acceptable results, the laser cutting machine must be properly calibrated. This is done by adjusting the laser parameters at which the machine is operating. The reader must be warned that each machine is different and obtaining the correct configuration is time consuming as there are no guidelines to automatically determine them.

### 2.3.1. Pulse duration

The pulse duration ( $T_{on}$ ) is one of the most important parameters because has a direct impact on the intensity of the beam as can be seen in Equation (3-2)

Several studies [29], [30], [31] have concluded that the use of ultra-short pulse lasers (i.e. pulse duration ranging from [ns] to [fs]), lead to ablation without thermal stress.

When the material is irradiated, the photon energy of the laser is transferred to the electrons of the material. When this energy is very high, the electrons will transfer the excess energy to the lattice in the form of heat. The heating not only causes the melting of the material, but also may induce heat damage in the surroundings of the cavity [29]. This area, affected indirectly by the laser, is called the Heat Affected Zone or HAZ.

When using ultra-short pulses, the laser only impacts the substrate for a time that is shorter than the relaxation time of the material. This means that the electrons do not have enough time to transfer the extra energy to the lattice before the next pulse hits the surface. Therefore, the material melts and evaporate faster but there is no Heat Affected Zone in the cavity or it is smaller than longer pulses [29].

According to [30], the pulse duration impacts mainly the cutting depth. As a lower pulse duration is used, the material is ablated more quick resulting in a deeper cut.

In this study, the pulse duration was varied in order to determine an optimum value for a c-Si solar cell with Al-BSF.

In contrast to literature, experiments using pulse duration in the range of picoseconds resulted in the use of more repetitions in order to avoid cell breakage. Small pulses caused either cell bending while cutting, insufficient cutting, or cell breakage after the cutting.

The explanation of this is that the minimum operating pulse width, according to Table 11, is 6 [ns]. At shorter pulse widths, the output power is not 30 [W] anymore but an unknown value fixed by the machine. The power is also determined by the operating frequency.

Since the laser machine tries to operate always at an average output power of 30 [W], for a given  $T_{on}$ , it exists a threshold frequency marked by the manufacturer. If the chosen frequency is *above* the threshold, the machine operates normally and can maintain an output of 30 [W]. However, *below* this threshold, the machine reduces its output power [32]. This is illustrated in Figure 19.

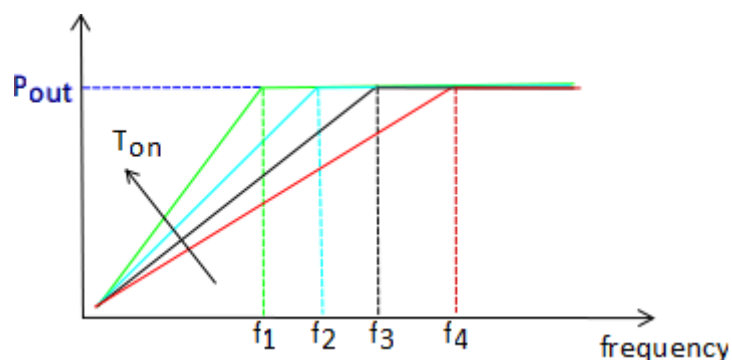


**Figure 19.** Frequency threshold for different  $T_{on}$  values. As the  $T_{on}$  increases, the minimum usable frequency shifts to a lower value. For instance, for a lower  $T_{on}$ , frequency  $f_4$  can be used. However, if the  $T_{on}$  is increased a lower minimum frequency ( $f_3$ ) has to be considered. If for the given value of  $T_{on}$  that leads to a minimum frequency  $f_3$ , lower frequency is chosen, the output power will be less than the nominal power. How less? It cannot be established as it is given by the machine itself. Adapted from [16] and [32].

An optimal value of 20 [ns] was found and the maximal  $T_{on}$  is assumed to be 25 [ns]. Values above this also results in no cutting or an aggressive process that leads to deposition of debris in the surroundings of the kerf.

### 2.3.2. Speed (s) and frequency (f)

Selecting the speed [mm/s] and frequency [kHz] impacts in the number of incident pulses in the working piece. Moreover, they determine how many pulses will overlap as illustrated in Figure 20.

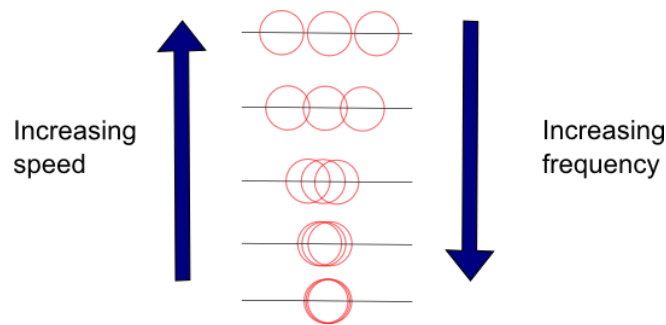


Figure 20. Pulse overlap as speed and frequency change.

The pulse overlapping can be expressed as a percentage, where 0% corresponds to no overlapping and 100% means that two pulses are completely overlapped.

Equation (3-3) Allows to mathematically calculate the overlapping percentage  $O_{percentage}$  [16]. The relation follows what can be observed in Figure 20.

$$O_{percentage} = \left(1 - \frac{s}{2r \cdot f}\right) \quad (3-3)$$

As described by Fornaroli, *et al* [31], the pulse overlap plays an important role during the early stages of cutting. This because as more pulses overlap, a deeper cut is achieved quicker. However, as the groove grow deeper, the laser beam does not impact the center of the kerf, but can also hit the side walls. Thus, leading to a decreased fluence acting upon the material. As a result, once the groove reaches this point, it will no longer increase its depth significantly. This can be appreciated in Figure 21.

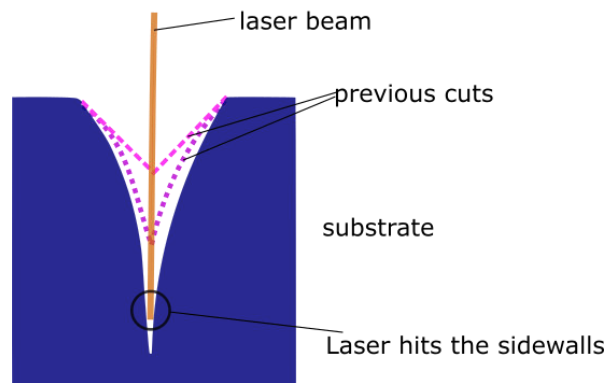


**Figure 21. Kerf development. During the first passes of the laser the kerf is wide. This allows the laser beam to hit in the middle of the kerf; thus, leading to a greater depth. However, as the cut develops, the kerf become narrower. At some point the laser will imping on the walls of the substrate, making the achievement of the desired depth more difficult.**

The chosen way of determining the effect of the laser on solar cells is to measure the efficiency of a cut cell. A higher efficiency of the reduced-size cell would indicate that the effect of the laser is small. The optimal cutting parameters are then chosen as those which lead the highest efficiency of a cut cell.

It was observed that a higher laser speed produces a cleaner cut of the cells. For instance, using a speed lower than 100 [mm/s] produced an uneven cut and harsh edges. A higher speed also leads to the highest cut cell efficiencies regardless of the  $T_{on}$  used. Although a higher speed implies a higher resultant efficiency, it also means that a greater number of repetitions is needed. The kerf is shallower with high speeds.

The effect of frequency is appreciated in Figure 22. Here, different laser configurations were used to fine tune the parameters. The frequencies at 90 [kHz] and 325 [kHz] reported the highest values. With a smaller frequency, the cut is smoother. It was assumed that a smoother cut would result in a higher efficiency. However, this is not the case. For instance, at  $f=325$  [kHz], some harsh edges can be detected in the cut cells, while at 90 [kHz] the edges were

smooth. Nevertheless, the efficiency is still higher at 325 [kHz]. Even more, the mechanical breaking of the cells is easier, which reduced the number of broken cells.

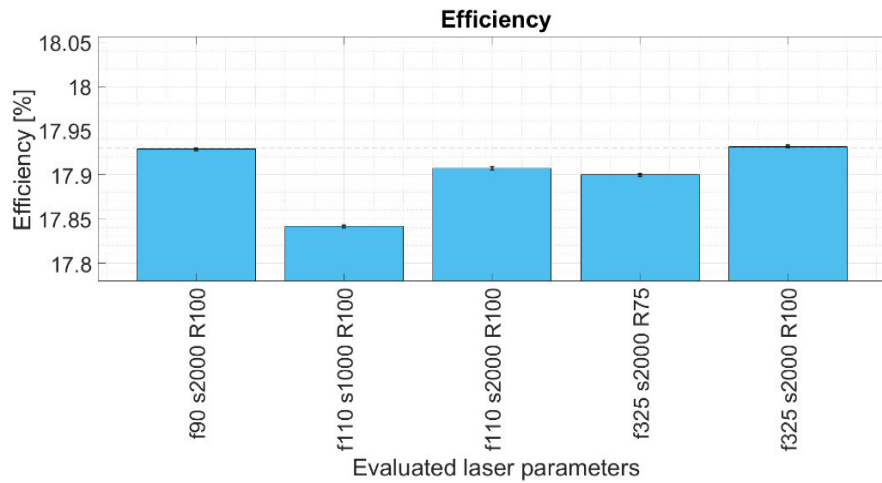


Figure 22. Comparison of different laser configurations used for fine tuning. On the x-axis, the used parameters of the samples are compared. (f)-frequency in [kHz], (s)-speed in [mm/s] and (R) - repetitions (number of passes). In all cases, the output power was set at 100%

Figure 19, stated that there is a minimum frequency threshold for a given  $T_{on}$ . When looking at the manufacturer's datasheet [32], for a  $T_{on}$  of 20 [ns], the *minimum* frequency is 210 [kHz]. If a lower value is used, then the output power is not 30 [W] anymore but an unknown value assigned by the machine itself. This is why at  $f=110$  [kHz] the efficiency is lower as, probably, the assigned value for the output power resulted in either incomplete cutting or a very aggressive one.

At  $f=90$  [kHz] there is also a peak in the efficiency. However, it is possible that the machine adjusted the output in such a way that it resulted, by chance, in a good efficiency.

Since at  $f=325$  [kHz] the selected value is above the threshold, the selected parameters are given by the user and not by the machine. This ensures repeatability and confidence in the cutting parameters

### 2.3.3. Repetitions

As the number of repetitions increases, the damage of the cell increases as well.

The reason behind this is that, when an elevated number of repetitions is used (ca. 250 and up to 1000), pits start to develop within the kerf. These pits grow deeper as more repetitions are used until they start inducing microcracks [31]. It is important to mention that the explanation given above was given for ultra-short pulses, however, the measurements also indicate that beyond 100 repetitions, the cell suffers damage that result in a reduction of efficiency.

### 2.3.4. Optimal laser configuration

From the experiments above, the optimal cutting parameters for a 185 [ $\mu\text{m}$ ] crystalline silicon Al-BSF are.

Frequency (f)	325 [kHz]
Pulse duration ( $T_{\text{on}}$ )	20 [ns]
Repetitions (R)	100
Speed (s)	2000 [mm/s]

Table 2. Optimal Cutting parameters for an AKW c-Si Al-BSF. Cutting from the backside with a Lasergraaf 30 [W] fiber laser.

**It is important to mention that the values shown in Table 2 are machine dependent and cannot be considered as universal.**

They are also valid for a specific type of cell. This is because different materials have different absorption rates, thus they will behave differently when irradiated by a laser and the thickness of the material has also to be considered.

The cutting method for the AKW cells is laser scribing followed by mechanical breaking.

It is interesting to mention, that with the values of Table 2, the edges of the cell are not perfectly smooth. Reducing the frequency to 90 [kHz] results in smoother edges. Nonetheless, the efficiency is still higher and the mechanical force to break the cells is less with the chosen parameters.

Although the results are not as expected, the differences can be attributed to the samples used by [31]. In the study, the authors used a 500 [ $\mu\text{m}$ ] silicon wafer, 1000 repetitions and a laser wavelength of 532 [nm].

In contrast, for these experiments a 185 [ $\mu\text{m}$ ] commercial solar cell was used. The fact that the used substrate is a solar cell is important because the laser must first cut the aluminium back contact. Hörde man [30] and [31] Fornaroli just proved a pure silicon wafer and the ability of the laser to cut it. Their parameters are adjusted to solely interact with the silicon material.

The Lasergraaf laser cutter is not designed to operate with ultrashort pulses. This is the reason that experiments with  $T_{\text{on}}=0.2$  [ns] did not exhibit correct results.

### 2.3.5. Effect of cell area

Bertrand [33] *et al*, performed a study in which they concluded that the cell efficiency would drop as the cell area decreases. In their paper, using solely squared cells, they found that beyond of 25 [ $\text{cm}^2$ ] using 5 x 5 [cm] cells the efficiency would drop dramatically.

Figure 23 shows the effect of the cell area on the efficiency of the cut cells using the Lasergraaf and the parameters of Table 2.

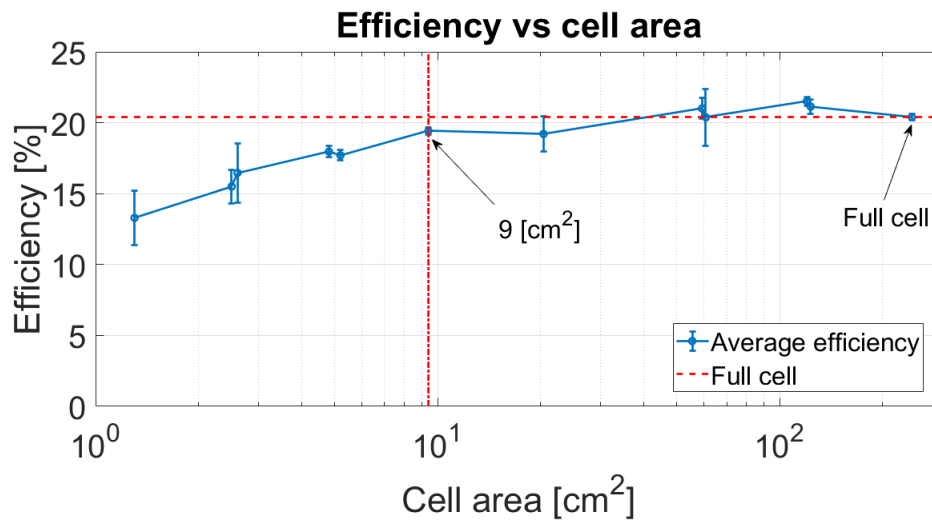


Figure 23. Change of the efficiency as the area increases. The efficiency of the uncut cell is marked as reference (“Full cell”). Note that for cell areas smaller than 9 [cm<sup>2</sup>] the efficiency drop is considerable.

From this experiment, the limit is found at 9 [cm<sup>2</sup>]. Then, it is possible to obtain smaller cells than 25 [cm<sup>2</sup>] without greatly compromising the efficiency of the cell.

For a solar cell, the short circuit current varies linearly with the area as can be seen in Figure 24.

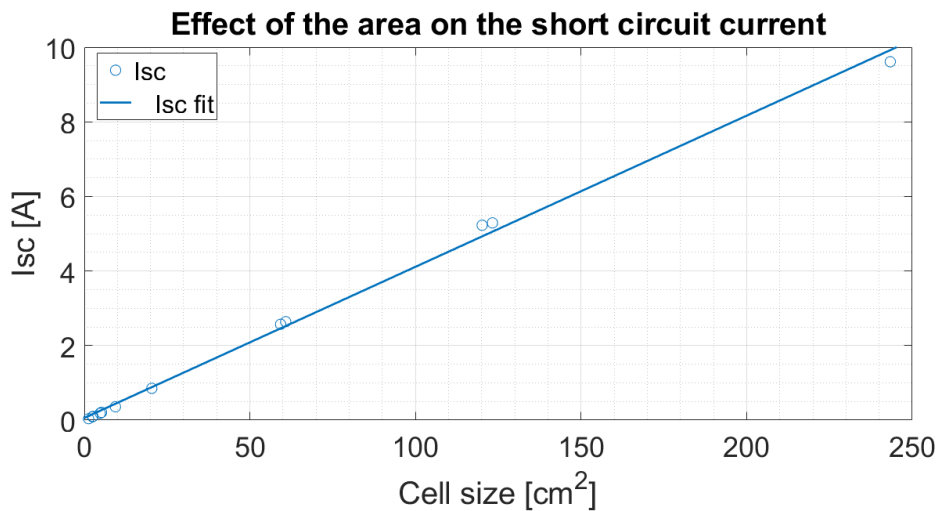


Figure 24. Effect of the area on the short-circuit current. A linear fit (“Isc fit”) was done to better clarify the linear behavior of the short circuit current and the area.



However, the open-circuit voltage, does not exhibit this behavior. In turn, it falls steeply as the cell area is reduced (Figure 25).

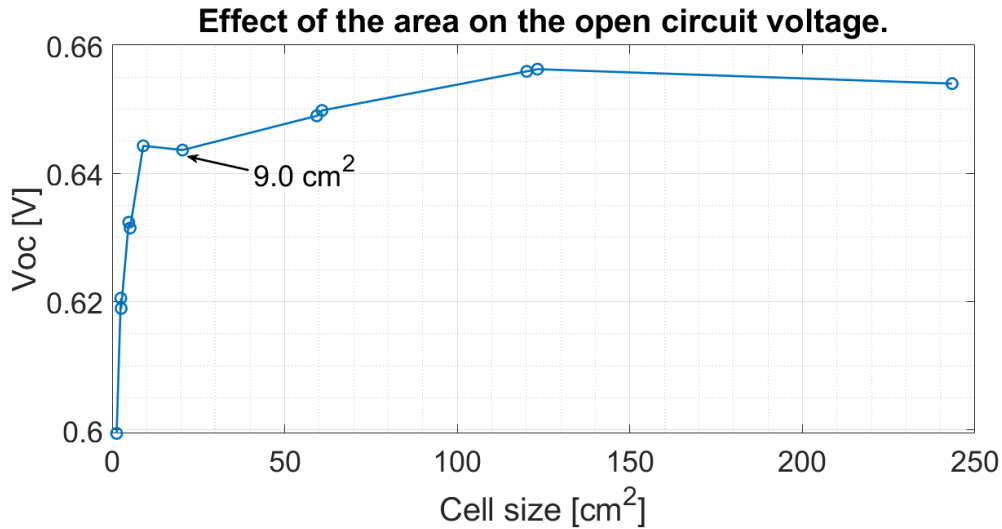


Figure 25. Effect of the cell area on the Voc. Although the drop of the Voc appears for areas larger than 9 [cm<sup>2</sup>], below this limit the quick drop can be seen as a very steep slope of the curve.

Since the open-circuit voltage is a measure of recombination within the solar cell, this drop in the  $V_{oc}$  indicates that the loss mechanism is because of recombination.

The recombination under the metallization grid (fingers and busbars) and the recombination at the edges are the two main areas where the  $V_{oc}$  losses occur as the cell size diminishes. When the cell is large enough, the generated current can compensate for the recombination in these regions [27].

The fill factor does not exhibit a clear trend as can be seen in Figure 26

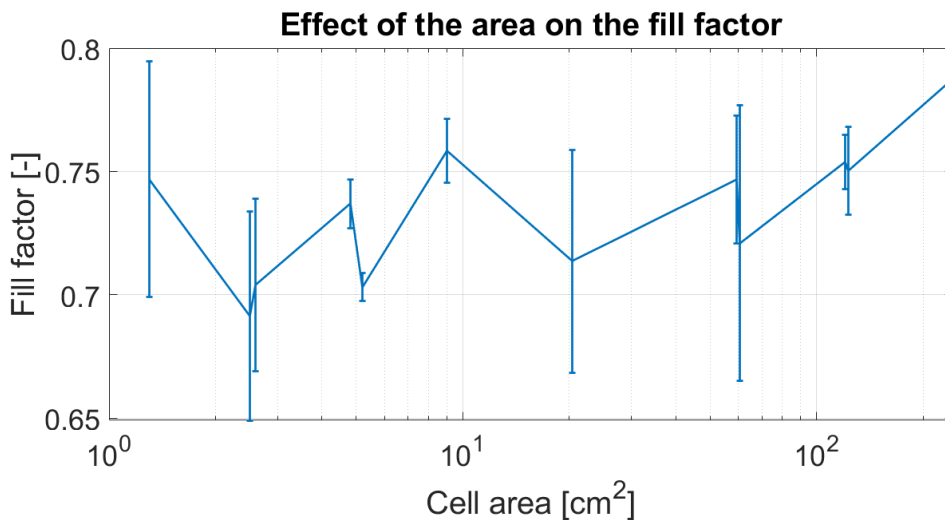


Figure 26. Fill factor for different cell areas. Note the large dispersion of the measured values shown by the whiskers. From this data, no relation can be inferred between the Fill Factor and the cell area.

Figure 27 shows the illuminated IV curves for different sizes. Their behavior follows what is expected from Figure 24 and Figure 25. However, a closer look near the  $V_{oc}$  point (Figure 28) reveals that the *series resistance* of the cell increases as the cell size becomes smaller.

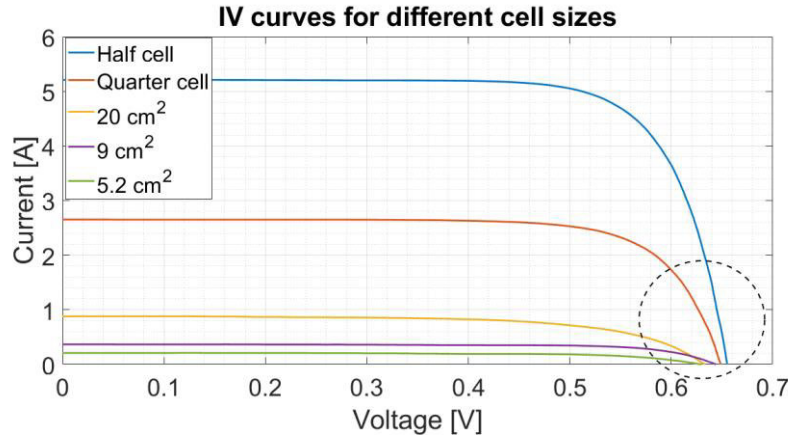


Figure 27. Illuminated IV curves for different cell sizes. The dashed circle indicates the zoomed area of Figure 28.

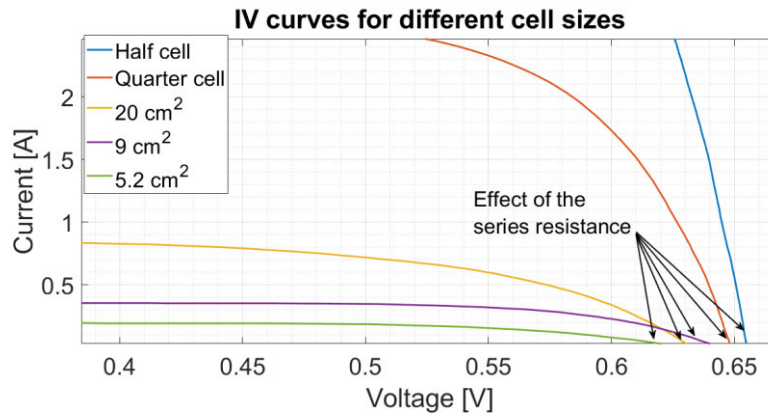


Figure 28. Detail of the illuminated IV curves for different cell sizes. The arrows are pointing at the slope of the IV curve near the  $V_{oc}$  point. The steeper the slope, the less series resistance of the cell. A very flat IV curve such as the one for 5.2 [cm<sup>2</sup>] indicate a very high series resistance.

The series resistance of the cells was calculated from the slope ( $m_{IV}$ ) of the illuminated IV curves using Equation (3-4) evaluated in the  $V_{oc}$  point.

$$R_s \approx \frac{1}{m_{IV}} = \frac{\Delta V}{\Delta I} \quad (3-4)$$

The series resistance congregates the semiconductor resistance, the resistance between the metal and the semiconductor and the resistance of the contacts themselves. Furthermore, its value can differ if different IV curves are used. Namely illuminated and dark measurements. This is expected as the current will flow through different paths in both conditions [34].

Figure 29 illustrates the relationship between the cell area and its series resistance.

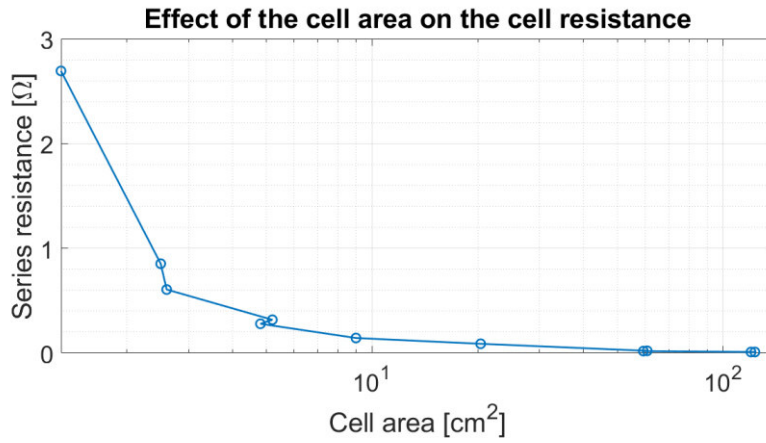


Figure 29. Effect of the area on the series cell resistance. The increased  $R_s$  is attributed to a loss of optimization of the metal grid at the front side.

The rise in the  $R_s$  can be explained with the degradation of the optimized front metallization grid. For a full cell, the front-contact grid is optimized for that size. Whereas, the cut cell does not take this into account. Bertrand *et al* [34] proved that the cut cells have indeed a non-optimized metal grid. Thus, by cutting them and then designing the small cell grid, it is possible to overcome the efficiency loss due to this factor.

### 2.3.6. Effect of cell shape

As discussed before, the recombination losses of a solar cell are partially determined by its edge. Therefore, it is possible to introduce the ratio perimeter-to-area  $k$  in Equation (3-5)

$$k = \frac{P}{A} \quad (3-5)$$

However, this ratio will always depend on the cell dimensions and it is a *dimensional* number with units [ $\text{cm}^{-1}$ ]. If the ratio is modified to Equation (3-6) [35], then for regular shapes, the values will be always constant, regardless of the dimensions of the figure.

$$\rho = \frac{P}{\sqrt{A}} \quad (3-6)$$

For the figures used in this study, the values of  $\rho$  are calculated and shown in

Table 3. Note that the rectangle is not included in the table as it is not a regular figure and its  $\rho$  will depend on its dimensions.

Figure	$\rho$ [-]
Circle	3.54
Square	4
Equilateral triangle	4.55
Regular hexagon	3.72

Table 3. Values of the Perimeter-to-Area ratio of regular figures. All regular figures, irrespective of its dimensions will have these values. Since the rectangle is not a regular figure, a fix value of  $\rho$  cannot be established. Hence it is omitted from the table

Equation (3-6) is important because it allows to discover errors. Either in the calculation of area or perimeter or in the cutting itself. Since  $\rho$  is always constant for a regular shape, a hexagon with a  $\rho=3.4$  indicates that either it is not a regular hexagon or its dimensions (especially the apothem) were wrongly determined.

Figure 30 illustrates the efficiency of different shapes. They are grouped using the value of  $\rho$ ; hence, the x-axis is non-dimensional. The dashed lines represent the theoretical values of  $\rho$  for regular shapes that appear in

Table 3.

Note that, as explained before, the rectangles do not have a fix value of  $\rho$ . Also, note that some rectangles are very close to become squares.

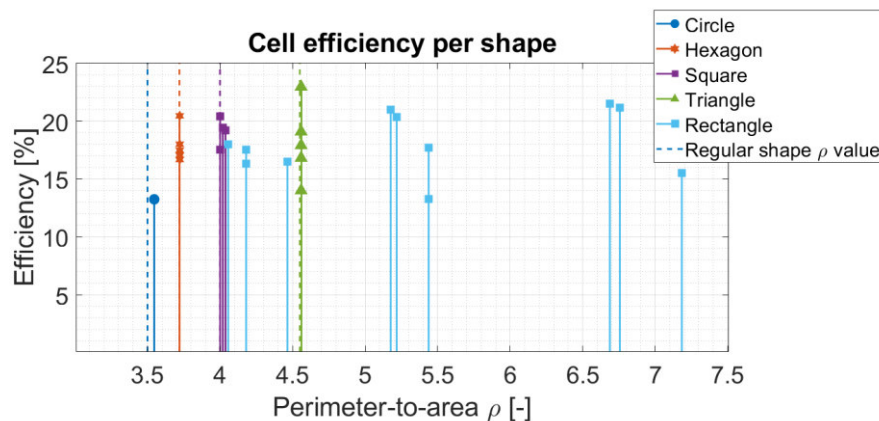
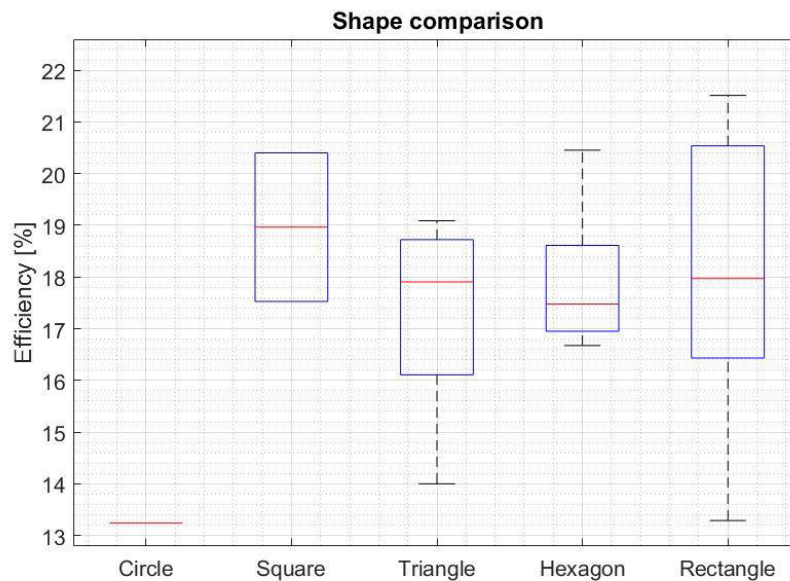


Figure 30. Efficiency per cell shape. Note that for the same  $r$ , there are different efficiencies. This is because the dimensions of the cells are different, albeit the same figure. A deviation from the dashed lines indicate that the figures are not regular figures as is the case with the circle cell which is more an ellipse, and some of the square cells.

A clearer comparison of the shapes can be seen in Figure 31. The square is the shape that has an overall greater efficiency. Using rectangles lead to a great dispersion of the values. This is in part because of the changing dimensions of the rectangles as can be observed in Figure 30.



**Figure 31. Overall comparison of cell shapes. It was expected that the higher efficiencies would be achieved with a circle and a hexagon, however squares and hexagons have the best performance. Why?**

The poor results for the circle are due to the damage of 2 cells during the cutting. Although the cells were not visible broken, their performance suggested that they were damaged. Also, some cells were completely broken when performing the mechanical cleavage. Reason for which this shape was not analyzed further. The explanation also holds for the fact that in Figure 30 and Figure 31 a single point –representing the average of the measurements– appear. Only 1 size was tested.

One clear disadvantage of using  $\rho$  instead of  $k$  is that the effect of the perimeter is unclear. In this way, several figures can have the same  $\rho$  but different dimensions. Geometrically speaking, for equal areas the circle has the least perimeter-to-area ratio ( $k$ ), followed by the hexagon then square, rectangle and finally the triangle. Therefore, it was expected that the efficiency of the cells cut in these shapes would follow the same order. However, Figure 31 illustrates that this is not the case.

As explained earlier, the circle has poor performance as the cutting process results in damage of the cells. It is important to mention that, for the shapes with *straight* edges, the cuts were performed in long straight lines. Scribing directly the shape in the wafer is not preferred as the behavior of the machine results in broken cells. This is one of the reasons that the circles have low efficiency.

A complete AKW solar cell is separated by its metallization grid into three different sub cells. This separation can be seen in Figure 32 marked by the yellow arrows.

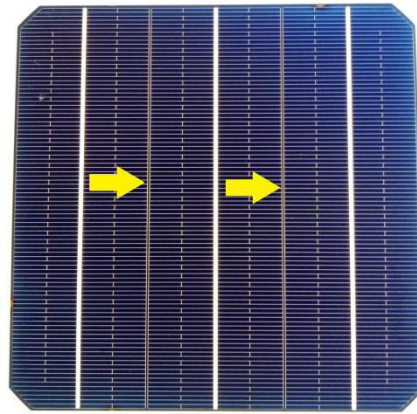


Figure 32. Complete AKW cell. The yellow arrows point to the fingers that separate this complete cell into three subcells. This separation is done directly by the manufacturer.

When a large cell is cut it is desirable to stay *within* the area enclosed by a *sub cell*. Or include a second or third busbar in the cutting design. If the cells exceed the delimited area, the generated carriers outside the area will have less probability of being collected leading to a reduction of efficiency. As an example, the large hexagon of Figure 33 was analyzed. The figure should be around 19% to 20% efficient. Nevertheless, its efficiency drops to 17.5%. Note that the figure edges surpass the width of the sub cell.

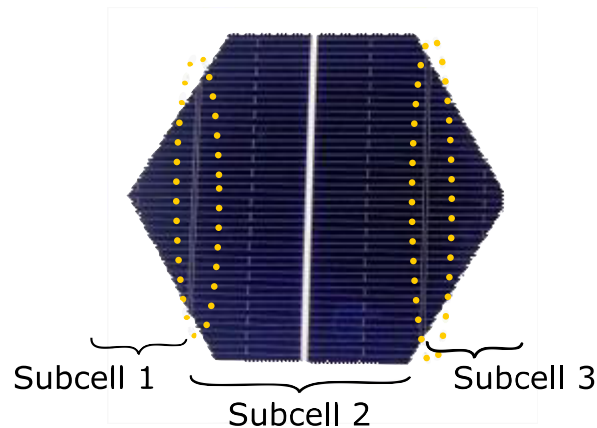


Figure 33. Large hexagon. The dotted lines show the parts where the cell is subdivided into three different subcells (marked as subcell 1, 2 and 3). Only subcell 2 has a busbar that allows carrier collection. Charge carriers generated in subcells 2 and 3 have lower probability of collection as they have to travel through a larger area.

Finally, as the cell becomes smaller, the shaded fraction of the fingers and busbars will increase. As the finger shading is assumed to be very small, only the busbars were considered. Following a similar analysis as Bertrand *et al* [27], the shading fraction of the busbars is defined as

$$R_{bb} = \frac{A_{bb}}{A_{cell}} \quad (3-7)$$

$A_{bb}$  refers to the area of the busbar. For the AKW cell this is 0.12 [cm] x height of the cell ( $h$ ). Equation (3-7) can be rewritten as

$$R_{bb} = \frac{0.12 \times h}{w \times h \times c} \quad (3-8)$$

Depending on the *figure* (square, rectangle, hexagon, etc.) the constant  $c$  will have a different value. This leads to the conclusion that the shaded fraction depends only on the *width* of the cell. *Width* is defined here as the distance *perpendicular* to the busbar. Hence, it is considered that the cell is oriented with its busbar in a *vertical* position.

Figure 34 compares the different cut shapes and their shading fraction. A higher value of  $R_{bb}$  will result in reduced cell efficiency. From this figure it can be stated that although circles and hexagons have privilege on the perimeter-to-area ratio, they lose more active area do to shading of the busbar.

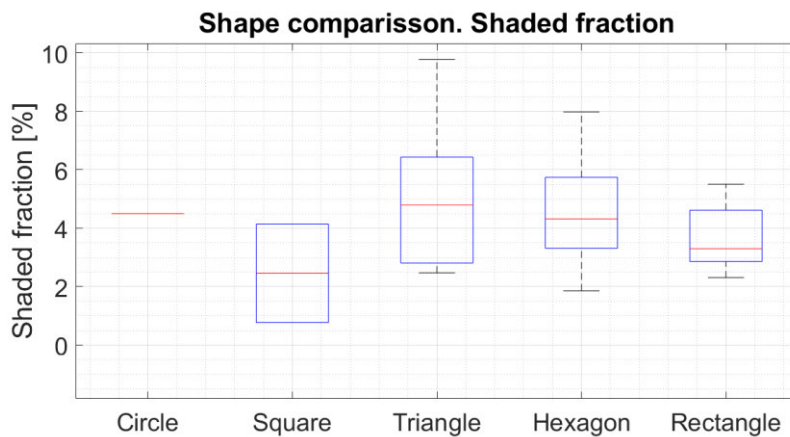


Figure 34. Shaded fraction of different cell shapes. Circles and hexagons, which have a lower perimeter-to-area, are in disadvantage with squares and rectangles that have less shaded fraction.

The effect of  $R_{bb}$  is clearly illustrated when analyzing two rectangles and two hexagons with the same area but with different busbar layout. Table 4 shows the effect of reducing the overall busbar length.

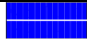



	Shaded fraction ( $R_{bb}$ )	Efficiency
	5.5%	16.33%
	3.03%	17.52%
	4.31%	17.04%
	4.99%	16.67%

Table 4. Comparison of 2 equal-area shapes with different shading fraction. For a same figure, the layout with less busbar length result in a considerable increase in efficiency. Even more, the shaded fraction plays a more important role than the perimeter-to-area ratio.

In [27], the authors found that  $k$  should remain below 1.5 [ $\text{cm}^{-1}$ ] to avoid a sharp efficiency loss. The value of  $R_{bb}$  was used to calculate a *corrected efficiency* that do not consider the effect of the busbars. However, it was believed that a better approach would be to define limits for these values. A good design can be achieved irrespective of the chosen shape. The relationship between  $k$ ,  $R_{bb}$  and the efficiency is shown in Figure 35. The highest cell efficiencies, equal or above 19% are reached with a perimeter-to-area ratio below 1.38 [ $\text{cm}^{-1}$ ] and a shading fraction



of *at most* 3.8%. As discussed earlier, despite of these two parameters, the cell must lie within the area of the sub cell.

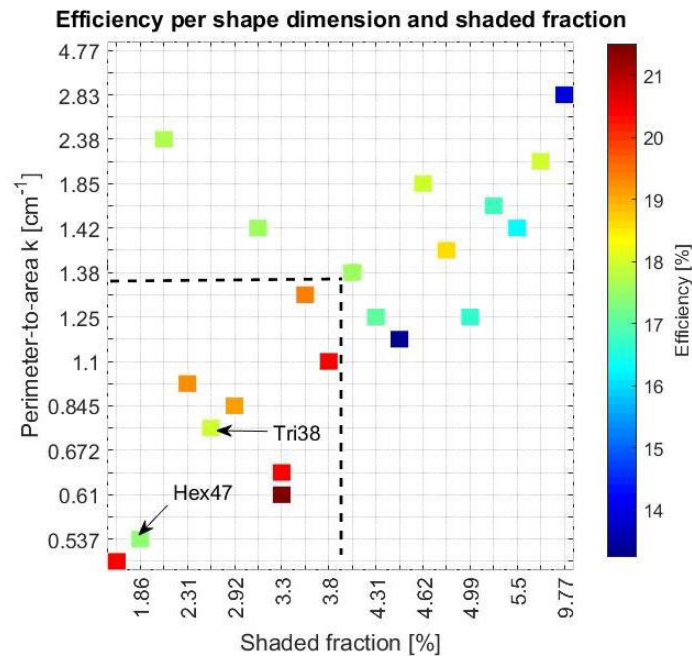


Figure 35. Figure efficiency by shape dimension ( $k$ ) and shaded fraction. The dotted line shows the limit for cells with efficiencies above 19%. The samples marked as “Tri38” and “Hex47” appear in the “high efficiency zone” but have lower than 19% efficiency have their areas split into several subcells

### 3.3. Future work

One of the main drawbacks of the laser cutting is the amount of time and material that is needed to fine tune the machine. Especially since every machine is different and each user has unique applications and materials. From all the revised papers, the working parameters were very different from one group to the other. Furthermore, there is not a standard procedure to save time and material.

Future work must be focused on creating, either a method, or a database that can be used as a starting point for the users. It should be noted that this methodology must be designed in such a way that the users don't rely on complicated setups.

A focus should also be given to optimizing the geometry by extending the analysis done here, and paying attention to the effect of the loss of the optimization of the original metal grid and how to reduce this effect.

Finally, simple passivation techniques can be designed to treat cut cells aiming to improve the efficiency and shunt losses.



### 3.4. Conclusions

The use of laser to cut crystalline silicon solar cells was discussed. The working principle of the laser was explained and how does a laser cutter can be tuned to scribe or cut.

One of the main features of the laser is that it melts the material inducing, in the case of solar cells, possible shunt. One way to reduce this undesirable effect is to cut the solar cells from the back (front side down). Also, not cutting completely through the cell but scribing followed by mechanical cleaving diminishes the probability for shunt creation. Finally, the repetitions should be kept as small as possible to reduce the damage to the cell.

With the use of a laser cutter it is possible to obtain different shapes from a commercial square cell. The geometry of the cell will impact its efficiency. The perimeter, source of edge recombination, should be minimized while the area maximized. As the cell becomes smaller, the perimeter of the cell will act negatively upon the efficiency. It was noted that not only the relationship of area and perimeter are important when choosing the geometry, but also the shaded fraction (caused by the busbars) must be considered.

The unexpected results of Figure 31 are attributed to the shading fraction of the cell, the involuntary splitting of large cells into different subcells and cells that were damaged during the mechanical breaking process.

Reducing the cell size by cutting is possible; however, its efficiency is to be preserved as much as possible, the size cannot exceed certain limit. In the case of the analyzed cells, this limit was found at 9 [cm<sup>2</sup>].

Further work is needed especially in determining the optimal laser parameters as here is not a unified and universal method to do it. This results in a lot of time and material needed to determine the optimal configuration. Attention should also be placed on reducing the waste material (unused cell) and the re-optimization of the metal grid after cutting.



# 4

## Building mini modules

### 4.1. Cell-To-Module

A solar cell performs different when alone and when connected to a string in a module. For instance, when connected it will be subject to current mismatch, resistive losses, optical losses and unused spaces. However, it can also benefit from optical effects. the ratio of *power* between the unencapsulated cells and the output power of the finished module is known as *Cell-to-Module conversion ratio* or CTM-CR and typical values range 0.94 to 0.97 [36].

$$CTM = \frac{P_{module}}{\sum P_{cells}} \quad (4-1)$$

To estimate the efficiency and power losses, the methodology proposed by Haedrich *et al* [22] was followed. In this method, the power losses are calculated in order as the light travels from the air to the cell active surface. The calculation allows to determine a loss/gain factor  $k_i$  that is then used for the power and efficiency loss or gain.

It is important to mention that the power loss or gain of a particular effect depends on the previous ones. Therefore, it is of extreme importance to determine the power losses in order. Equation (4-2) shows the *power* loss/gain of the  $j$ th element.

$$\Delta P_j = P_0 \times (1 - k_j) \prod_{i=3}^{j-1} k_i \quad j \leq 13 \quad (4-2)$$

Note that Equation (4-2) does not consider the first two effects  $k_1$  and  $k_2$ . This is because these two relate to the impact of the inactive areas and do not produce *power* losses. It only affects the *efficiency* as can be noted in Equation (4-3)

$$\Delta \eta_j = \frac{P_0}{I_{STC} \times A_{cell}} \times (1 - k_j) \prod_{i=3}^{j-1} k_i \quad 3 \leq j \leq 13 \quad (4-3)$$

In Equations (4-1) and (4-2) the term  $P_0$  represents the sum of powers at which each cell is operating. This term allows to take into consideration the current mismatch [22].

$$P_0 = \sum P_{cell_{op}} \quad (4-4)$$

The limiting cell is assumed to be operating at its maximum power point (MPP). The current of this cell at its MPP will determine the current at which the rest of the array will work. Knowing the current of each cell makes it possible to know the operating voltage, hence output power of each individual cell by looking at its IV curve. This procedure is best seen in Figure 36 that shows the operating point of some of the cells used in the reference module.

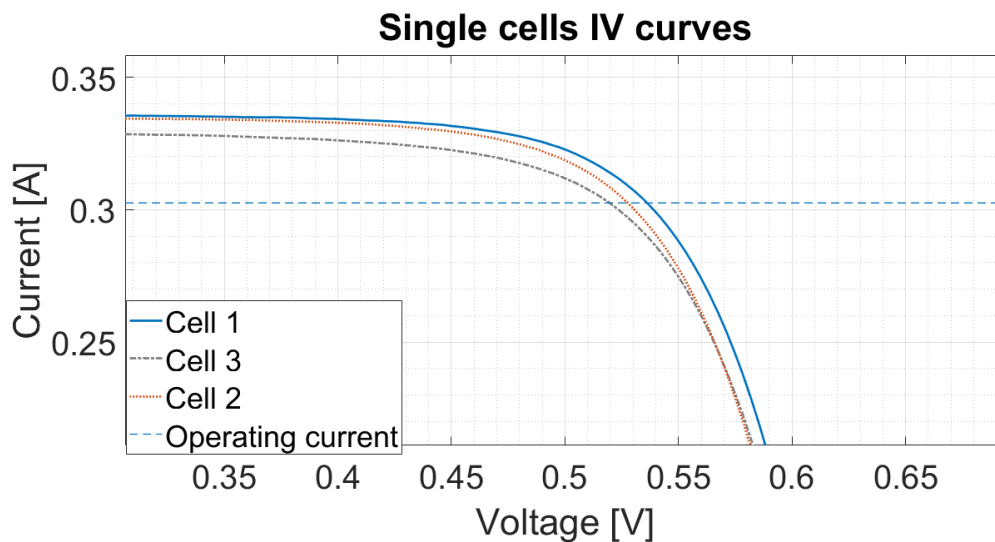


Figure 36. Operating point of the series-connected cells. For clarity, only three cells are plotted. Note that the graph is zoomed around the maximum power point. These three cells are operating at the current marked by the dashed line (“operating current”) which is dictated by the least producing cell (“Cell 2”). Only this cell will be at its MPP while the operating point of the rest should be determined.

#### 1.4.1. Inactive areas

The inactive areas of the module comprise the module border and the cell interspacing. These areas do not generate power but are also illuminated with light, hence, reducing the efficiency of the module. The inactive areas do not cause a *power* loss. According to [22], the efficiency loss factors  $k_1$  (effect of the module border) and  $k_2$  (effect of the cell interspacing) can be estimated with Equations (4-5) and (4-6).

$$k_1 = 1 - \frac{A_{border}}{A_{module}} \quad (4-5)$$

$$k_2 = 1 - \frac{A_{cell\_spacing}}{A_{module}} \quad (4-6)$$

### 1.4.2. Optical losses

As the light travels from the cell to the air, it encounters obstacles that cause a decrease number of photons reaching the active area of the cell, causing power losses. Following Haedrich's [22] method and nomenclature, the optical *losses* are

- Reflection at the glass-air interface ( $k_3$ )
- Absorption of the glass ( $k_4$ )
- Reflection at the glass-EVA interface ( $k_5$ )
- Absorption of the EVA ( $k_6$ )

These mechanisms are illustrated in Figure 37. The full list of gain and loss mechanisms is can be consulted in Appendix 8.2

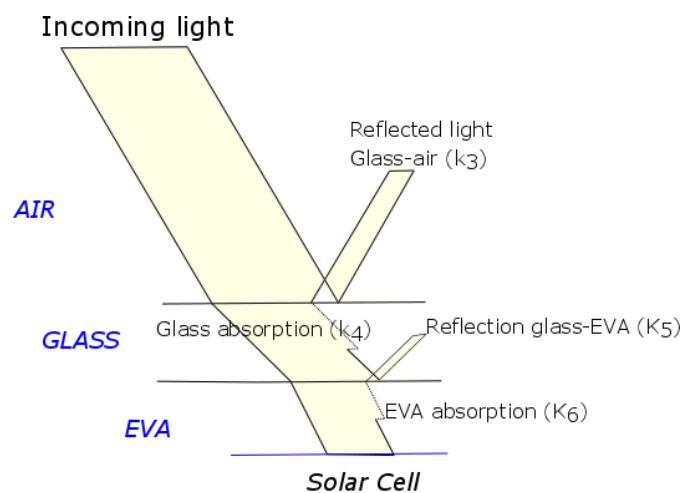


Figure 37. Schematic of the optical losses. Observe how the incoming light beam becomes thinner as it crosses through the different interfaces.

a) Reflection at the glass-air interface

When the incoming light reaches the glass, part of it will be transmitted through the glass and another will be reflected. This occurs because the light is travelling from a medium with a refractive index  $n_1$  (air) to a second medium with refracting index  $n_2$  (glass).

According to Figure 38, the reflectivity of the used CORNING glass is between 9 and 10 % for all wavelengths. This means that for all the incoming light, only 90% of it can be transmitted *through* the glass.

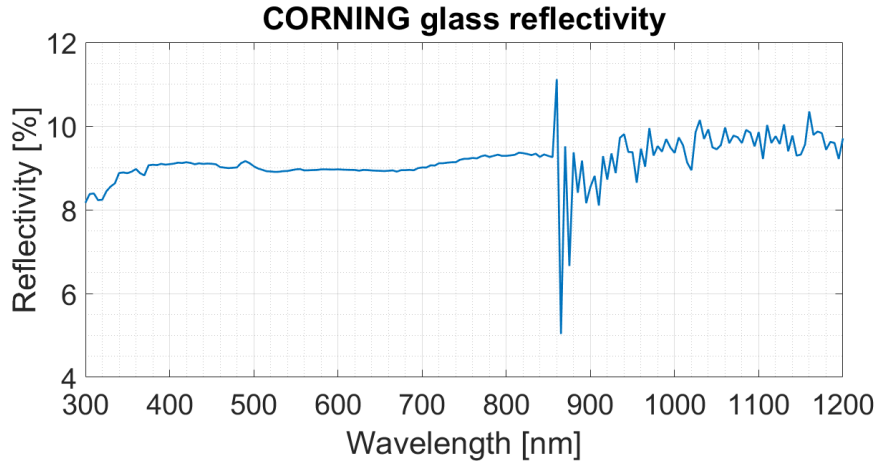


Figure 38. CORNING glass reflectivity per wavelength. The peak at around 850 [nm] is due to a change in the sensors within the equipment.

Equation (4-7) translate this 10% of lost light into a power loss factor  $k_3$  [22].

$$k_3 = 1 - \overline{R_{glass}} \quad (4-7)$$

$$\overline{R_{glass}} = \frac{\int I_{AM1.5}(\lambda) \times SR(\lambda) \times R_{glass}(\lambda) \times d\lambda}{\int I_{AM1.5}(\lambda) \times SR(\lambda) \times d\lambda} \quad (4-8)$$

$I_{AM1.5}$  is the solar spectrum as shown in Figure 40 and  $SR$  is the cell spectral response (Figure 39). The spectral response of the AKW cell was measured using an EQE setup of the PVMD group at TU Delft. With the measured data, the spectral response of the cell can be calculated according to Equation (4-9) [37]. Note that the units of  $\lambda$  are [nm].

$$SR = \frac{q\lambda}{hc} \times EQE = \frac{\lambda \times EQE}{1239.8} \quad (4-9)$$

$R_{glass}$  corresponds to the data of Figure 38 which indicates the reflectivity of the CORNING glass per wavelength.

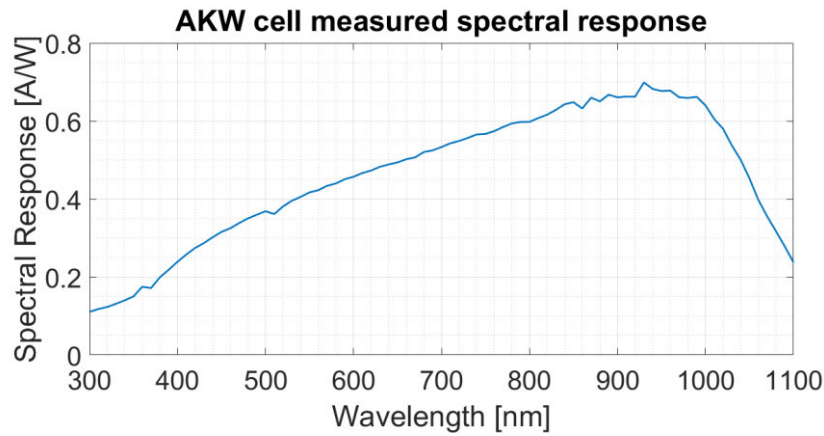


Figure 39. Measured AKW solar cells spectral response.

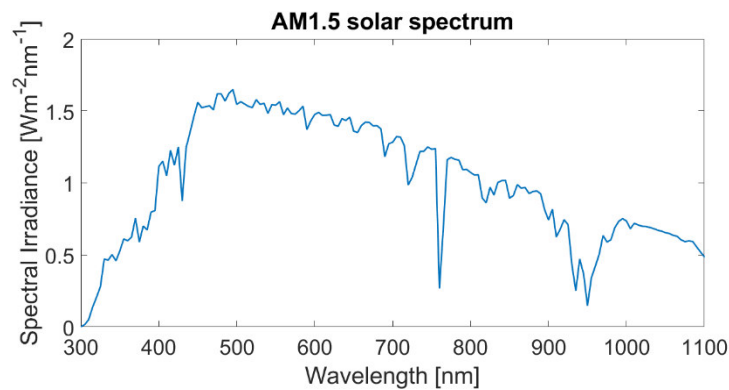


Figure 40. AM1.5 Spectrum. Retrieved from [38].

Note that Equation (4-8) is a *weighted* value. This means that the effect of the reflected light is compared *weighted* to the light that would have been seen by the cell otherwise.

#### b) Absorption of the glass

Once the light has entered the glass, a fraction of it will be absorbed by the material. A spectral analysis of the CORNING glass (Figure 41) reveals that it is mainly a non-absorptive material in the visible range. It only absorbs a small fraction of the ultraviolet light in the analyzed range. The small peak at 850 [nm] is due to a sensor change within the measurement equipment.

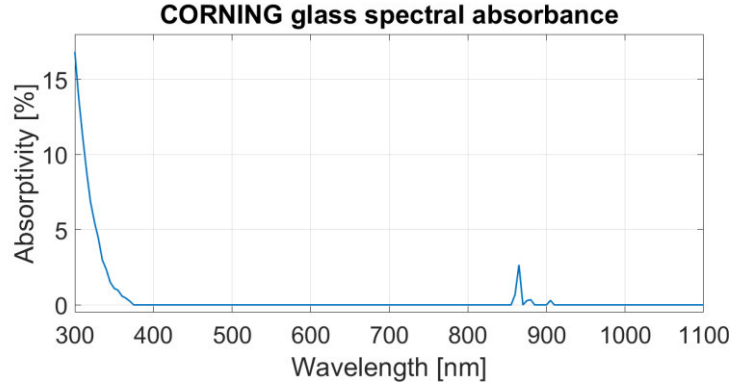


Figure 41. Spectral absorbance of the CORNING glass

The loss due to the glass absorption,  $k_4$ , can be calculated in a similar manner as  $k_3$  but considering

1. Only the transmitted light ( $1 - R_{glass}$ )
2. The spectral absorbance as depicted in Figure 41

$$k_4 = 1 - \overline{\alpha_{glass}} \quad (4-10)$$

$$\overline{\alpha_{glass}} = \frac{\int I_{AM1.5}(\lambda) \times (1 - R_{glass}(\lambda)) \times \alpha_{glass}(\lambda) \times SR(\lambda) d\lambda}{\int I_{AM1.5}(\lambda) \times (1 - R_{glass}(\lambda)) \times SR(\lambda) \times d\lambda} \quad (4-11)$$

### c) Reflection at the glass-EVA interface

The interface glass-EVA is an additional point for reflection. The light travelling within the glass will find a difference in refractive index (interface glass-EVA) and part of it will be reflected to the glass. The reflectivity at this interface can be calculated from the Fresnel equations for normal incidence (Equation (4-12))

$$R_{glass-EVA} = \left( \frac{n_{EVA} - n_{glass}}{n_{glass} + n_{EVA}} \right)^2 \quad (4-12)$$

The LAMBDA spectrometer does not give the refractive index  $n$  as an output. Therefore, it must be calculated. In order to do so, the interface air-glass and air-EVA is used. The transmittance is obtained with the spectrometer and using also Fresnel's equation for normal incidence (Equation (4-13)).



$$T_{normal} = \frac{4n_1n_2}{(n_1 + n_2)^2} \quad (4-13)$$

Considering that the refractive index of air  $n_1=1$  and solving Equation (4-13) for  $n_2$ , the value of  $n_{glass}$  ( $n_2$  in this case) is found. An analogue procedure is used to determine the refractive index of the EVA using an air-EVA interface, i.e., measuring the transmittance of a single layer of EVA surrounded by air. Figure 42 show the obtained results. A typical value of  $n_{glass}$  is 1.5 which indicate that the results are as expected. Also, the indices of the encapsulant (EVA) and glass are almost the same which helps to reduce the reflected light at this interface.

The major differences appear in the blue region of the spectrum; therefore, more reflection is expected within this range. It is interesting to see that  $n_{EVA}$  falls to zero in the ultraviolet range. This is because the material absorbs almost all the light at short wavelengths and no light is transmitted.

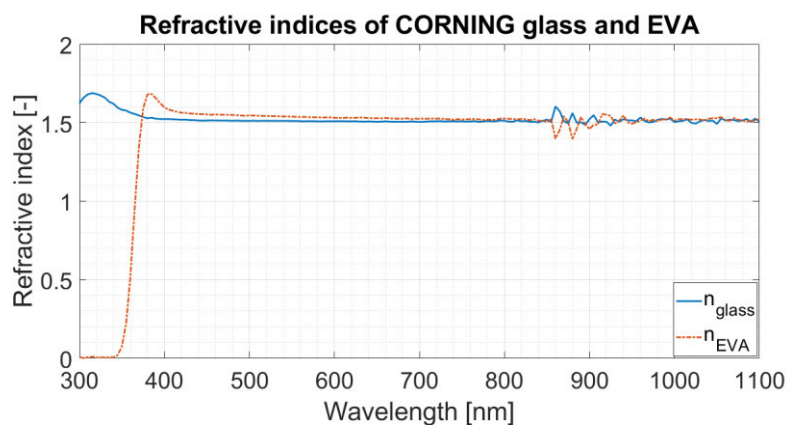


Figure 42. Refractive indices of CORNING glass and EVA.

The reflectivity at the glass-EVA interface is depicted in Figure 43. Note that the values are very small, almost reaching 0. This is a result of a good matching of the refracting indices of the glass and the encapsulant. These values are also plotted in Figure 43. As expected, more light is reflected when the matching of the indices is not perfect.

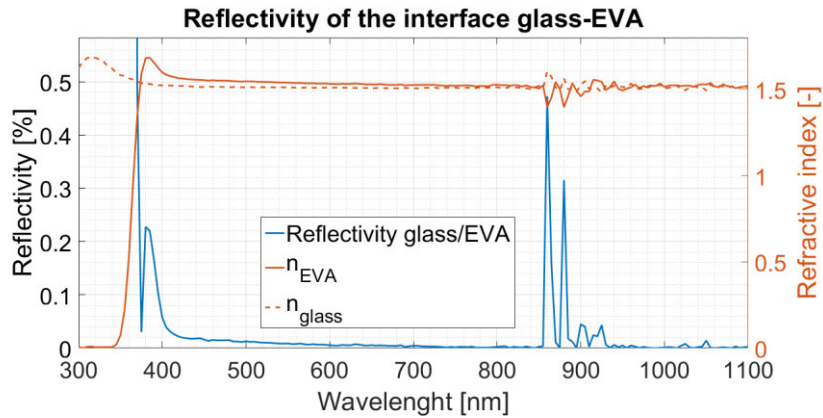


Figure 43. Reflectivity at the glass-EVA interface. As expected, the good matching of the refracting indices of glass and encapsulant is translated into a very low reflectivity at the glass-EVA interface.

These results lead to think that the power loss due to this effect is very small.

As done before, the loss factor  $k_5$  is calculated with Equation (4-14). This is achieved by using the *weighted* reflectivity as done before and shown in Equation (4-15)

$$k_5 = 1 - \overline{R_{glass/EVA}} \quad (4-14)$$

$$\overline{R_{glassEVA}} = \frac{\int I_{AM1.5}(\lambda) \times (1 - R_{glass}(\lambda)) \times (1 - \alpha_{glass})(\lambda) \times SR(\lambda) \times R_{glassEVA}(\lambda) d\lambda}{\int I_{AM1.5}(\lambda) \times (1 - R_{glass}(\lambda)) \times (1 - \alpha_{glass}) \times SR(\lambda) \times d\lambda} \quad (4-15)$$

#### d) Absorption of the EVA

The last optical loss is the absorption of light by the EVA. As can be seen in Figure 44, the EVA absorbs all the UV light. That being the reason for the extremely high values (beyond 100%) at small wavelengths.

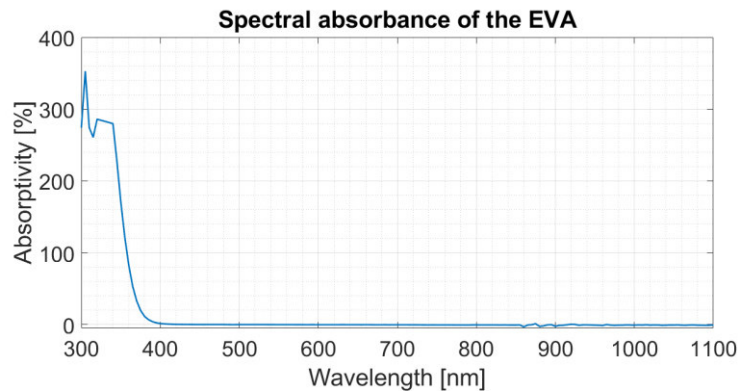


Figure 44. Spectral absorbance of the EVA. This encapsulant absorbs almost no light in the visible nor infrared range. However, it absorbs most of the ultraviolet light.

The calculation of the power loss factor is similar as Equations (4-14) and (4-15), but taking into account the transmitted light ( $1 - R_{\text{glass/EVA}}$ ) and including the absorptivity  $\alpha_{\text{EVA}}$ .

#### 1.4.3. Optical gains

Not all the light that reaches inactive areas of the cell is considered lost as it can be redirected towards the cell. Thus, this section discusses the mechanisms shown in Figure 45.

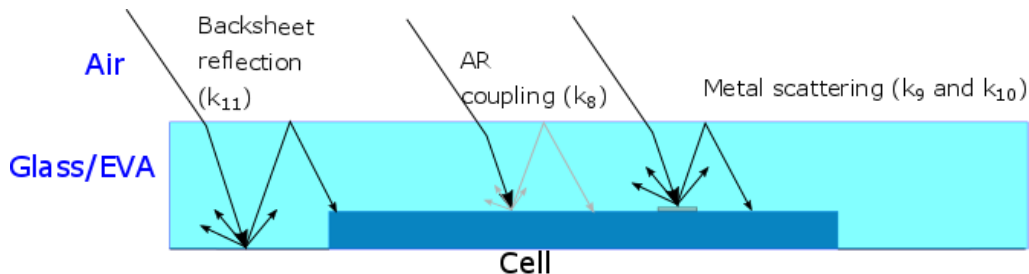


Figure 45. Optical gains. These are achieved from the reflection from the back sheet, the coupling of the refractive indices of the anti-reflective (AR) coating and the encapsulant; the scattering from the busbars and metal fingers.

##### a) Optical coupling

The anti-reflective (AR) coating of the cell can be optically coupled with the encapsulant reducing the reflected light from the *surface* of the cell enhancing its absorption. This is achieved because the refractive index of the encapsulation (glass-EVA) is increased from 1 (air) to roughly 1.5. The AR has a refractive index of approximately 2.1 [22]. Hence, less light is reflected by this coupling.

Furthermore, the addition of the encapsulation material allows light to be redirected to the cell by total internal reflection. Even more, light that reaches the fingers and interconnection wires can be redirected to the cell also by total internal reflection. It is important to mention that this

phenomenon occurs at the glass-air interface as the glass and the EVA have roughly the same refractive index. Consequently, the glass and EVA can be considered as a single *encapsulant* from an optical point of view.

These coupling mechanisms are not possible when the cell is surrounded by air; therefore, they are considered as gains.

To make a proper analysis, a black back sheet is needed, which leads to the assumption that the gain is only due to optical coupling of the encapsulant ( $k_8$ ) and scattering in the interconnection wire ( $k_{10}$ ), busbars and fingers ( $k_9$ ).

The combined properties of a glass-EVA sample were determined using the LAMBDA spectrometer.

It is possible then to establish a ratio of the short circuit current of a cell measured in air and the same magnitude measured after encapsulation. Equations (4-16), (4-17) and (4-18) allow to determine the gain factor.

$$k_{8,9,10} = \frac{\frac{I_{sc,encap}}{I_{sc,air}}}{(1 - \overline{R_{encap}})(1 - \overline{\alpha_{encap}})} \quad (4-16)$$

$$\overline{R_{encap}} = \frac{\int A_{AM1.5}(\lambda) \times (1 - R_{encap}(\lambda)) \times SR(\lambda) d\lambda}{\int A_{AM1.5}(\lambda) \times SR(\lambda) d\lambda} \quad (4-17)$$

$$\overline{\alpha_{encap}} = \frac{\int A_{AM1.5}(\lambda) \times (1 - R_{encap}(\lambda)) \times SR(\lambda) \times \alpha_{encap} d\lambda}{\int A_{AM1.5}(\lambda) \times (1 - R_{encap}(\lambda)) \times SR(\lambda) d\lambda} \quad (4-18)$$

Note that in Equations (4-16), (4-17) and (4-18) the sub index “*encap*” refers to the combined material glass-EVA.

#### b) Back sheet reflection

The gain obtained by the light scattering at the back sheet depends on the distance between cells as well as the chosen material. According to Haedrich *et al* [22], the change of the short-circuit current can be estimated using an exponential fitting of the form given by Equation (4-19).

$$\Delta I_{sc}(d) = \frac{(I_{sc}(d) - I_{sc0mm})}{I_{sc0mm}} = A_1(1 - e^{-\frac{d}{t_1}}) \quad (4-19)$$

In order to obtain the fitting parameters  $A_I$  and  $t_I$ , a single cell module with a white reflective back sheet is laminated. A dark mask is then placed on top. The distance  $d$  from the edge of the cell to the mask is increased after every measurement under the WACOM solar simulator.

The same procedure is repeated using a black back sheet.

Figure 46 shows the result of this fitting. Note that a white back sheet provides a greater increase of the short-circuit current on larger distances. However, the results below 2 mm should be taken carefully. The lack of points in this area might lead to the wrong conclusion that a black sheet is a better option if going for closer spacing.

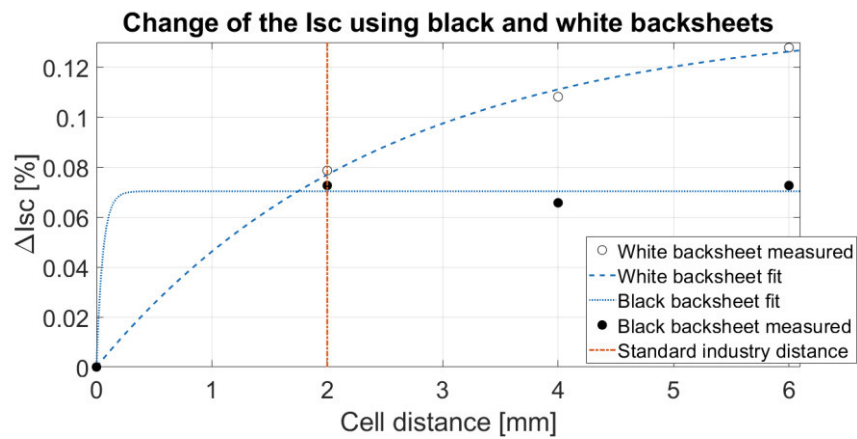


**Figure 46.** Short circuit current change when varying the spacing between cells. It would seem that if the inter-cell spacing is less than 2 [mm] (industry standard) the black over performs the white back sheet. Nevertheless, the reader should be cautious in interpreting the graph. Both curves are a fit. This means that the behavior is just an approximation. If more points are used the fitting would improve. However, making modules with cell spaces below 2 [mm] is very difficult and unpractical. Hence, these measurements can be avoided.

However, in practice the cell spacing ranges from 2 to 3 [mm] and the results shown in Figure 46 are valid.

The optical gain from the reflection is then calculated with Equation (4-20) which is only valid for a square cell.

$$k_{11} = 1 + \Delta I_{sc} \quad (4-20)$$

It must be mentioned that this formula does not consider a specific effect of the cells located at the corners or edges of the module. These cells receive more light and therefore produce more current. This increased current can also be responsible for a greater power mismatch since all the cells are connected in series. However, for large industrial cells, if they are chosen in such a way that the deviation of the  $I_{sc}$  is within 0.2 [A], the effect is negligible. Furthermore, this spacing can also improve the performance of the module in a 0.5% [39].

#### 1.4.4. Resistive losses

The interconnection of the cells by means of copper tabbing wire results in energy being dissipated as heat. The same holds for the interconnection between strings. Dissipated power in the tabbing wire can be expressed as shown in Equation (4-21).

$$P = RI^2 \quad (4-21)$$

Where  $R$  is the resistance of the wire,  $I$  is the current flowing through it and  $P$  is the dissipated power.

The power dissipated in the string interconnection can be easily estimated by measuring each individual cell. Noting that the operating point of the cells has already been corrected for current mismatch, it is possible to obtain the theoretical power by adding the individual operating points. After this, they are measured under the WACOM solar simulator. The difference in power can then only be attributed to resistive losses. The same principle applies to the interconnection between strings.

It is important to highlight that the contact resistance is neglected [22].

#### 1.4.5. CTM ratio of the reference module.

The analysis proposed by Haedrich *et al* [22] and explained above, was designed for full size commercial modules. Nonetheless, the impact in small-sized modules needs to be assessed in order to determine if the above analysis is also valid for these modules.

In order to validate the model, a 6-cell, 10 x 10 [cm] mini module with CORNING glass and white back sheet was built. A photo of this module can be seen in Figure 47.

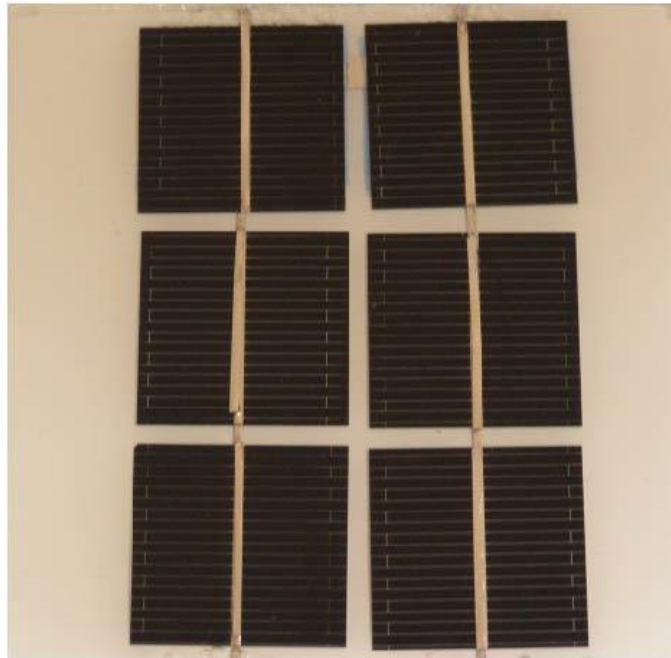


Figure 47. Fabricated reference module.

The cells considered were the cut cells. Therefore, the effects of the laser are not considered. The reason behind this is that the cut cells are the *constructive elements* of the mini module, just as the full-size cells are for the full-size module. Therefore, a fairer comparison is possible. Naturally a small mini module will produce less power than even a full-size cell (which can be required by an application). Because of this is not possible no account for the power of a complete cell and it was decided to use the already-cut cells as the starting point.

Table 5 shows the loss mechanisms. The minus sign as well as values of  $k_j$  greater than 1 indicates a gain. This is better seen in Figure 48 and Figure 49. The results have a similar tendency as the ones published in [22].

With the small cells, the CTM ratio of the reference module is 1.0174. This high result is achieved thanks mainly to the optical gains. They can counteract the CORNING glass reflection which is the biggest power loss of this module. Using a white back sheet and more spaced cells (4 [mm] vs 2[mm] of a commercial module) also allows a power boost.

The used CORNING glass is also thinner (0.7 [mm]) than a standard solar glass of 3 [mm]. This causes a minimal glass absorption which is even negligible. However, the CORNING glass is not designed for photovoltaic use, which explains the high glass reflection loss.

The biggest drawback of the mini module fabricated with CORNING glass is the efficiency loss due to the module borders.

Even though it is possible to cut the glass, the chance of breaking it while doing the operation is high. Since the available glass size was only 10 x 10 [cm] the module size was bounded to this value. Fitting more cells increase the probability of not completely encapsulating them or breaking them during lamination.

The use of a different material such as flexible foil is expected to improve the efficiency as a custom-size module or with non-conventional shape can be better fitted. Thus, reducing the unused area and increasing the efficiency.

If the efficiency losses due to inactive areas are not considered, the efficiency of the reference module is increased from 18.35 % (efficiency of a single cell) to 18.65 % (efficiency of the active area).



Loss mechanism	Loss factor $k_i$ [-]	Efficiency loss [%]	Power loss [W]
Module border area	0.59	7.49	0.000
Cell spacing area	0.93	1.28	0.000
Glass reflection	0.91	0.87	0.087
Glass absorption	1.00	negligible	0.001
Reflection glass/encapsulant	0.99	0.06	0.006
Encapsulant absorption	1.00	0.02	0.002
Optical coupling	1.08	-0.67	-0.067
Reflection of the back sheet	1.10	-0.90	-0.090
Cell interconnection	0.96	0.37	0.037
String interconnection	0.96	0.18	0.018

Table 5. Summary of evaluated gains and losses of the reference module. The negative sign indicates an improvement of efficiency or power as are values above 1.

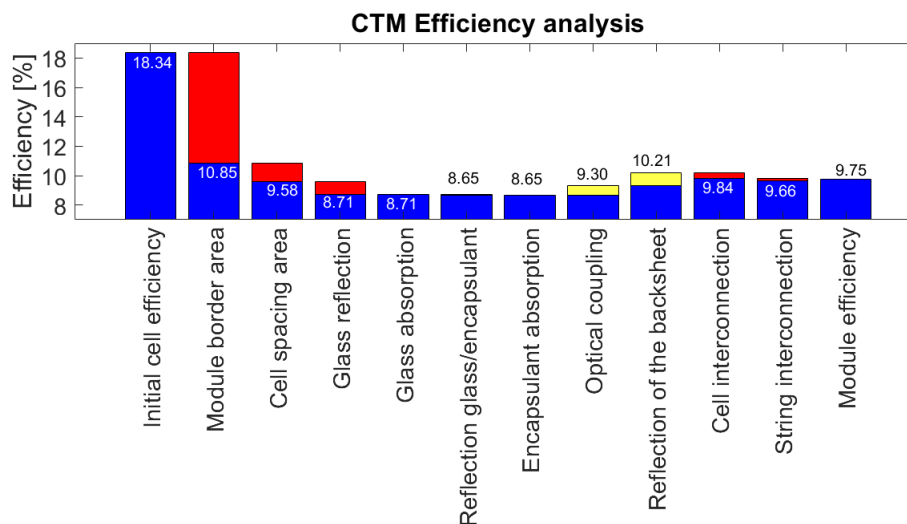


Figure 48. CTM efficiency analysis of the reference module. The red color shows the loss mechanisms; the yellow, the gains. The number above each bar indicates the resulting module efficiency after considering each effect.

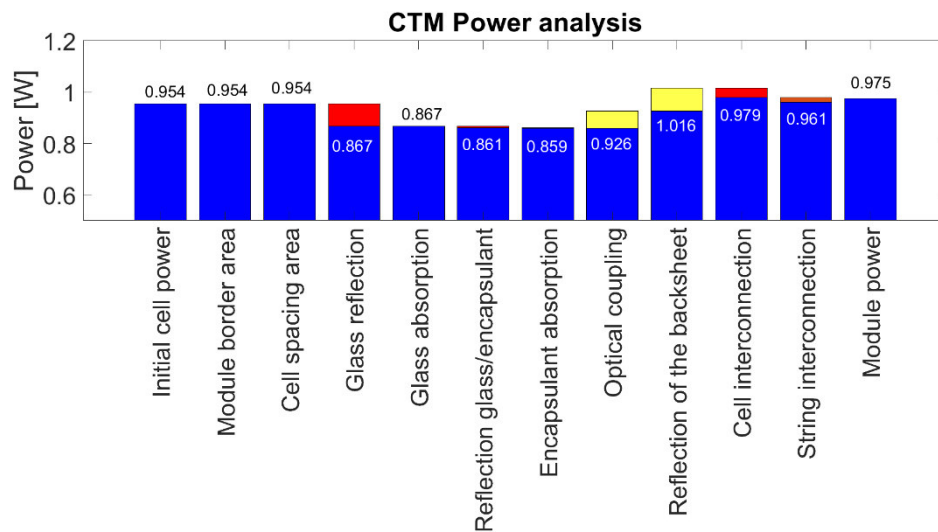


Figure 49. CTM Power analysis of the reference module. The red bars indicate loss mechanisms while the yellow ones gains. The number above each bar is the resultant power after each effect is considered. Note that the inactive areas do not cause power losses.

## 4.2. Electrical contacts

### 2.4.1. Theory of electrical contacts

Before analysing the electrical contacts used in the prototypes, it is important to understand how an electrical contact is formed.

Firstly, every surface, no matter how flat appear to the eyes, is rough in a microscopic scale. When the two electrodes become close enough, some ridges will become in *contact* with the other allowing a current flow only on these spots (called *a-spots*). In a macroscopic level, the *a-spots* cause that the *real* contact area is effectively reduced. This is, the whole area of a connector is not the area of the connector as not every point of the connector is in contact with its counterpart [40].

The *a-spots* appear as bottlenecks (constriction) to the current flow path causing a *contact resistance* which is different from the resistance of the conductor [40],[41]. Figure 50 shows the current flow over two contacts. It can be appreciated that if more pressure is applied, more edges will be in contact creating new *a-spots*. As the number of contact points increase, the total contact resistance will decrease. Hence, increasing the pressure on the contacts will reduce the contact resistance [41].

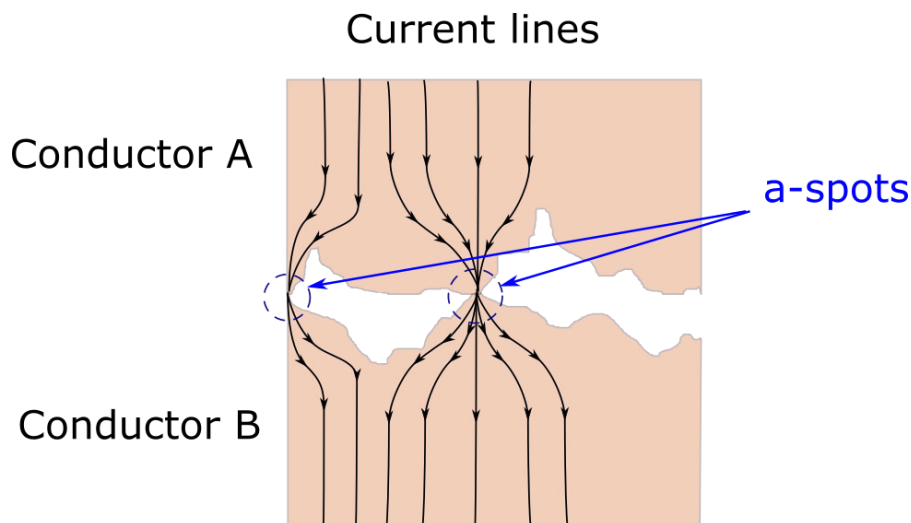


Figure 50. Overview of an electrical contact. Some of the current lines have been omitted for clarity. Note how the a-spots constitute a constriction for the current. Adapted from [40]

The irregularities and resultant cavities formed by the a-spots allow the presence of contaminants which can form films on top of the contacts, especially oxide layers. The films may act as an additional barrier to the current increasing the contact resistance, especially if they grow on top of the conducting a-spots [41]. However, the use of films and coating can also have the opposite effect by protecting the surface against oxidation [40].

#### 2.4.2. Contact materials

Among the many metals used for electrical contacts are gold, silver, platinum, molybdenum, tin, lead, etc. However, this work will only focus on the two used materials: copper and nickel.

- Copper is a material that has been known to mankind since ancient times. It can be easily identified by its red coloration. It is very resistant to corrosion at ambient temperature. However, at higher temperatures a layer of oxide becomes evident. Furthermore, copper is susceptible to salt water which can greatly corrode the material. It is an excellent electrical conductor with a resistivity as low as  $1.5 \times 10^{-8}$  [ $\Omega\text{m}$ ]. Nevertheless, for electrical applications is often alloyed with other metals in order to improve its mechanical properties. Depending on the application, Cadmium, silver, or tin can be used with the drawback of reducing its electrical performance [40].
- Nickel, on the other hand is less conductive than copper, with a resistivity of nearly 8 times higher. Still, it is widely used in electrical applications, mostly as an alloy with iron or even copper. It has an excellent resistance to corrosion and low thermal expansion which makes it suitable for sealing or high temperature applications. It finds also application in printed circuit boards (PCB) [40].

### 2.4.3. Electrically conductive adhesives

A different alternative to create an electrical contact is to use an *electrically conductive adhesive* -or ECA-. These products have conductive particles diluted in an adhesive solution. Though mainly used in the electronic industry, they are finding their way into the photovoltaic industry as an alternative to soldering, especially in the manufacturing of *shingled modules*. [42], [43].

The idea behind the shingle cell technology is to place cut cells with their busbar aligned in one edge, one on top of the other. In this way, the busbar of the bottom cell will be connected to the back contact of the top cell. By using this method, the shaded fraction of every cell will be replaced by an active area with the advantages of reducing inactive area losses (no cell interspacing), increasing the active area (greater efficiency) and potentially reducing the resistive losses due to the small-sized cells [42].

An ECA performance will be influenced by the concentration of conductive particles (defined by the manufacturer), the thickness of the applied product, the curing time and the temperature at which it is cured. These factors modify the resistance of the adhesive, affecting the fill factor of the module [44].

Eitner, *et al* [45] concluded that the ECAs are a good alternative for lead-free soldering as the required temperature is lower or for module designs where soldering is not possible. Nonetheless, the soldering method still has the lower resistance. In order to correctly exploit the advantages of the ECA, and, since its effectiveness is easily influenced by external parameters, it is better to use an automated system.

### 2.4.4. Neodymium magnets

A versatile way to create a temporal attachment of two surfaces is by using magnets. The so-called “super magnets” are fabricated with a composition of Neodymium, Iron and Boron. These magnets allow a great attachment force in smaller areas. Even more, they are coated with a 12 [µm] layer of an alloy of Nickel and Copper to prevent brittles and corrosion [46].

One advantage of the Neodymium magnets is that they can be fabricated in different forms. One of them, which was used in this work, is as *pot magnets*. Here, a Neodymium magnet is housed inside a steel *pot* which enhances the magnet’s adhesion over an iron surface. The pot can be manufactured with a thread that allows the use of standard nuts [46].

Figure 51 illustrates the magnet used. It is fabricated by Supermagnete® [46], a magnet manufacturer and seller in The Netherlands.

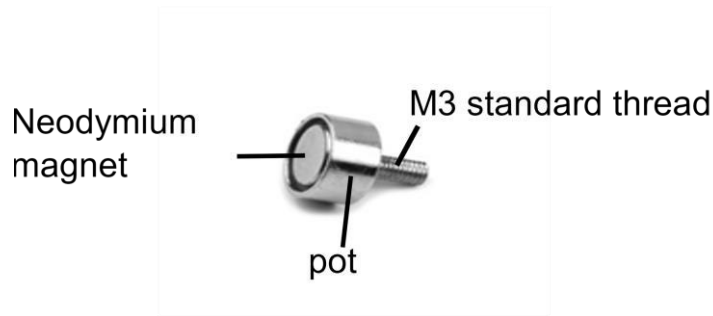


Figure 51. Pot magnet used in this work. Adapted from [46].

Because of the construction of the pot magnet, the actual magnet will not be in contact with the surface. Rather the *rim* of the pot will be. The M3 standard thread is used to attach a circular connection pad. This means that the current will flow over the *pot* and not the magnet.

#### 2.4.5. Analysis of the proposed contacts.

One of the greatest disadvantages of the ECAs is their storing conditions that require temperatures as low as  $-25$  [°C] to  $-40$  [°C]. Because of this, an electrically conductive adhesive tape (3M 1181 tape) was used. Although it was found that this tape is not suitable for shingle cell fabrication, it is still a good option for non-conventional designs.

The comparison between a standard tabbing wire and the 3M copper tape was done by taking a 7.5 [cm] long tabbing wire and single piece of copper tape were measured with a bench multimeter. For thin, thick and copper tape the resistance was found to be 0.05 [ $\Omega$ ]. This leads to conclude that the copper side of the tape presents no additional problem, thus, the elevated series resistance must be caused by the adhesive. Several experiments were performed by connecting 2 and three segments of the tape using the tape's adhesive and placing the magnets with the measuring probes randomly on top of the tape.

The results of Figure 52 show that as soon as the adhesive is used the resistance greatly increases. The results for "Used connection" and "Used connection worn" target the actual layout of the tape as it was used on the final design.

As indicated by the wide dispersion of the values, the resistive effect of the adhesive is vastly affected by

1. The position of the magnet
2. The wear-and-tear of the tape.
3. The stiffness of the junction.

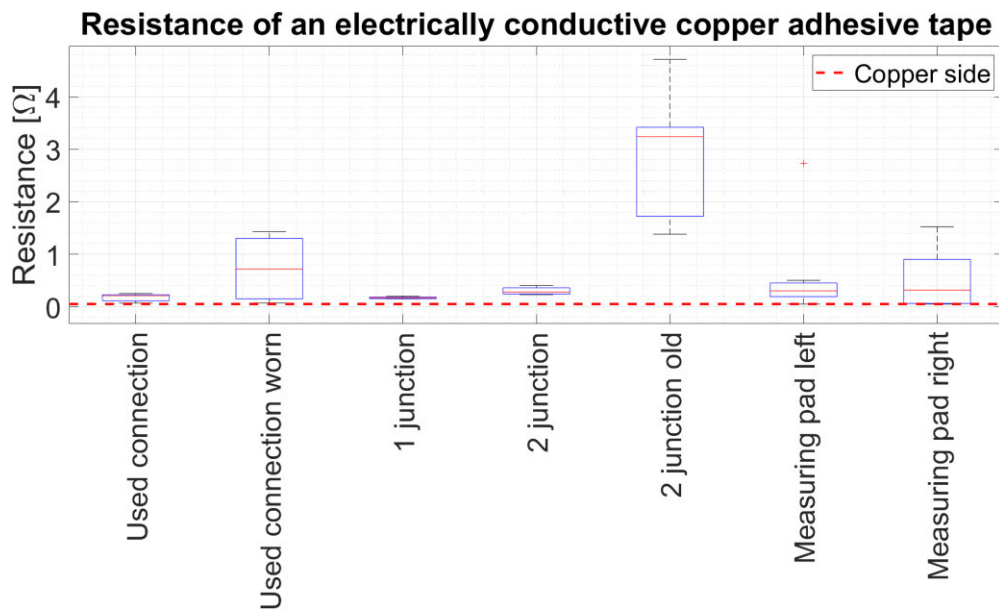


**Figure 52.** Resistance analysis of the electrically conductive copper adhesive tape. The red dashed line marks the resistance of the copper side (without adhesive) of the tape. This is used as reference for comparing the behavior of the adhesive under different scenarios. The words “worn” and “old” indicate that the tape was attached, removed and re-attached again to simulate aging. It becomes obvious that, as the glue ages or loses its adhesive strength, the resistivity increases. Refer to Figure 13 for a list of the patterns used.

The resistance of the adhesive increases when the junction starts to detach. In some applications that require a sliding movement over the tape and the constant connection and disconnection of them result in adhesive detachment. Depending on the position of the magnet, the resistance can reach values in the ohm range, while the resistance for the copper side lays within the milliohm domain.

The wide dispersion of values observed in Figure 52 reinforce the idea that the junction is not completely stable. This can lead to an uncertain behaviour of the tape within an application.

As the magnets were used as contact materials, its effect was analysed by measuring the change in short circuit current of encapsulated cells before and after the magnet. The difference, if any, can then only be attributed to an extra resistance added by the magnet itself.

The pieces of the PV puzzle were used as tests, before housing them into the silicone rubber leading to a current reduction of just 11 [mA] on average. This is a rather small loss considering that the operating currents are, on average 640 [mA]. This represents a 1.8 % loss. However, the aforementioned numbers are a generalization. The observations indicate that the losses are even less. Figure 53 shows a boxplot with all the taken measurements. Except for two outliers out of 11 samples, most of the readings have a difference in the short circuit current around 2 [mA]. Therefore, the effect of the magnets can be considered insignificant.

### Analysis of the change in $I_{sc}$ because of the magnet

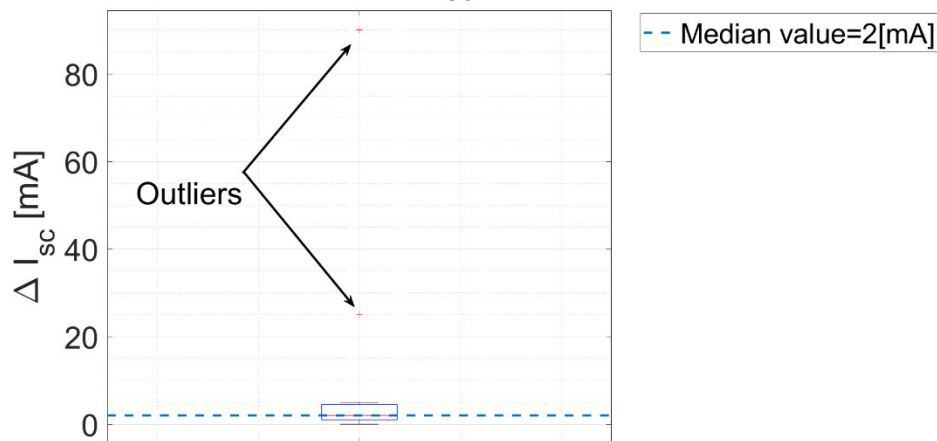


Figure 53. Boxplot of the measurements of the *difference* in current before and after the magnet. Note that the median is 2 [mA] which is a very small value.

### 4.3. Future work

The unified method for determining CTM ratio used here is suitable for full scale modules. However, it obviously doesn't consider losses that are inherent to a mini module such as the laser loss and fitting the power of the full cell in relation with the smaller area for the cells used. In short, the study in this work considered a cut cell as the initial unit, while a better approach would be to refer to the original uncut cell.

As for the contacts, four probe measurements to determine the specific contact resistance of the magnets might illustrate better their effect. Due to storing requirements it was not possible to experiment with ECA, which can also help to compare their performance with that of the copper tape. Furthermore, the possibility to use ECA in combination with the copper tape aiming at developing new solder-free connection techniques can be explored.

### 4.4. Conclusions

A complete Cell-to-module analysis was performed leading to conclude that the inactive areas play an important role in improving the power output of the module, especially when a reflective back sheet is used. Even when the unused areas lower the module's efficiency, they can improve the output power, and even overcome the optical losses as well as the resistive losses. This cannot be always achieved with commercial modules that investigate high packing density and bigger cells. But, in a mini module, the cells become smaller, bringing the resistive losses down. Under this situation, the benefit of the optical gains can be fully exploited. The biggest source for optical losses is the glass reflection which can be relatively easy tackled using anti-reflective glass.

The glass used in the experiments demonstrated to be suitable for use in mini modules from the optical point of view. However, the mechanical properties of the CORNING glass might not be adequate for industrial purposes.

An electrically conductive adhesive tape was analyzed for its use as solar connector for mini modules. While the copper side of the tape demonstrated to be an excellent conductor, as expected, the main feature, which is the conductive adhesive, underperforms. The adhesive is not suitable at all for cell interconnection and it has a very high resistance, especially when it is pulled out and then placed again, causing a considerable uncertainty in the resistance value.

The used pot magnets do not represent a great disadvantage as the reduction in current is extremely small. This indicates that the magnets can be effectively used as electric contacts for solar cells.

One of the most important aspects when considering to form an electric contact is the pressure applied in order to maximize the number of a-spots. The proposed magnets also help to comply with this requirement.



# 5

## Foldable module

### 5.1. The Miura-Ori fold

The Miura fold –or *Miura-ori*- fold is a method for folding a piece of paper in such a way that each component remains flat. In other words, each of the faces that form the fold do not suffer bending.

This fold was invented by Koryo Miura to store a compact solar array into a rocket and be able to deploy it once in space. An additional feature is that, in contrast to a typical map folding, the Miura fold allow folding and unfolding with a single movement, by pulling and pushing opposite corners [47].

The reader is encourage to see Nishiyama [47] for a detailed explanation on how to apply the Miura folding to a standard piece of paper.

Figure 54 shows the crease pattern of the folding. This crease pattern results when a piece of paper is folded and then unfolded. The valley folds result from folding the paper *upwards* forming a *valley* in the paper. A mountain fold, on the contrary, will produce a *mountain* by folding the paper *downwards*.

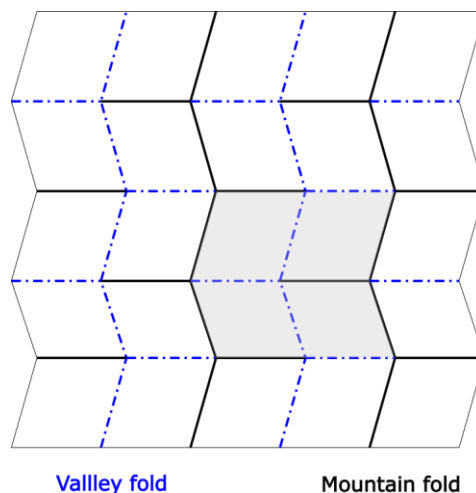


Figure 54. Crease pattern of the Miura fold. The shaded area corresponds to a *fundamental region*.

From Figure 54 it becomes evident that the Miura fold consist of a tessellation of basic parallelograms. Furthermore, Miura [48] establishes that four of these parallelograms form a *fundamental region* (highlighted in Figure 54). This fundamental region, when folded, results in a tetrahedron. At the common vertex of tetrahedron, the sum of the four angles is always  $2\pi$ . Everywhere within the folding, a fundamental region can be found. As it is proved that the fundamental region can be folded flat, then the whole folding can be folded from a 3D construction to a flat one.

The Miura folding is a two-dimensional fold. Meaning that in order to fold it, an action must be performed along the horizontal *and* the vertical axis. This in opposition to a concertina fold where the action is only applied alongside the horizontal axis [48].

In a traditional orthogonal fold -which is also a two-dimensional fold where all the creases are perpendicular, hence its name-, two movements are needed to fold the plane. The horizontal and vertical axes are independent of each other allowing folding in one direction *then* in the other. However, the construction of the Miura fold forces both axis to move *simultaneously*. The effect of folding one fundamental region is then transferred throughout the entire plane [48]. Thus, allowing the closure or deployment with a single movement by pushing (pulling) opposite corners [49].

Orthogonal folding presents another problem that is well tackled by the Miura fold. The stress induced on a folding material increases as its thickness does. In the orthogonal folding, the thickness on the sheet increases with each fold. This can be easily proved by folding a piece of paper in half, then in half again (orthogonal folding) and so on. The stress ( $t_s$ ) caused by the fold can be expressed by the relation between the thickness of the sheet ( $t$ ) and its curvature radius ( $r$ ).

$$t_s \propto \frac{t}{r} \quad (5-1)$$

With each fold, the sheet thickness increases and, as seen by Equation (5-1), the stress too. If this stress is too large, a crack might start at a vertex and propagate along the fold line [48].

While the aforementioned is true for every folding method, its effects are reduced by the Miura-ori fold as there are less pieces inside the previous fold and in every case they do not overlap completely, reducing the thickness of the sheet and the stress [48].

## 5.2. Origami in photovoltaics

Just like many other things present in everyday life, the use of origami in solar energy found its origins in space exploration. As stated in Section 5.1, the Miura folding was invented in order to store a photovoltaic array in a space ship and deploy it in space. Specifically, Koryo Miura invented the folding for an experiment of the Japanese satellite *Space Flyer Unit*,

launched in 1995 [50]. More recently, NASA developed a prototype for folding a 25 [m] diameter into a compact size that results in a diameter of only one tenth of the deployed surface. Although this array is a cylindrical form, the basic fold is inspired in the Miura fold [50].

Back on Earth, the idea of fabricating foldable solar modules is not new. Especially since foldability is closely related to portability. Several designs already exist on the market. Nevertheless, any of the commercially available products make use of the Miura folding or other origami techniques. Most of the products are solar chargers for gadgets or portable generators. On average they deliver 10 [W] of power with a USB output of 5 [V] which is enough to power up small gadgets such as smartphones, speakers, power banks or tablets. The folding technique that is mostly applied is folding the modules over themselves (1-dimension folding).

A clear application of the Miura folding in solar cells was achieved by Tang, *et al* [51] by fabricating a solar cell which incorporates micro hinges in order to fold it using the Miura fold. In this case, the process is such, that the hinge is incorporated during the cell manufacturing process. This is achieved by fabricating the cell with a conventional process, including the design of the metal contacts and the hinge. In fact, the hinge is part of the contact and has a serpentine-like design. Once the contacts have been deposited, a dielectric material is also deposited to form a mask and then the silicon is etched away to form the parallelogram shape and separating the cell in different units, each joined by the serpentine hinge. The prototype, a 6.3 [cm] x 6.5 [cm] (unfolded) forms a single solar cell which can be folded into a compact 5.4 [cm] x [1.2] cm shape.

A performance analysis of the cell was made after folding the prototype up to 40 times. During the first folds, a decrease in the performance was observed, especially a reduction in the current density. Since the performance loss stabilized after 40 folds, this de-rating is attributed to breakage of some serpentine hinges. As the number of folds increase, the material starts to deform preventing breakage and allowing a normal current flow [51].

Binyamin, *et al* [52] proposed a portable solar system which incorporates the Miura fold to store the panels. In this complete system, the panels are stored inside a box. While deploying the box lid can be made flat and the panels easily unfolded exploiting the Miura folding aided by a motor. The panels lay on top of the flat lid. This structure is attached to a dual axis sun tracker system. The whole system (deployment of panels and solar tracking) is controlled by an Arduino microcontroller.

### 5.3. Design of the foldable module

The design of the origami-based solar module started with each parallelogram. The prototype is aimed to power a 15 [W] load with a 5 [V] output and 3 [A] output. Therefore, all the modules must be able to supply this amount of power. An efficiency of 80% was assumed for the buck converter used to step-down the voltage to a stable level of 5[V] when the module is operated under sunny conditions. The design of the buck converter used is included in the Appendix 8.3

In order to demonstrate the effectiveness of the Miura fold, a mini module consisting of 15 parallelograms in a 3 x 5 array was proposed. Note that according to Section 5.1, it is possible to construct a foldable unit with an array of any size. However, with a smaller array the fold cannot be fully appreciated; albeit, it is still functional. Furthermore, using an odd number of parallelograms, ensures the folding and unfolding just by pulling the edges.

Figure 55 shows the basic parallelograms used in the foldable module. Each parallelogram consists of a mini module made of 4 cells. It is important to mention that the cells inside the parallelogram is a trapezoid. This was done in order to keep the voltage high by increasing the number of cells and, at the same, keeping the current low using small-sized cells.

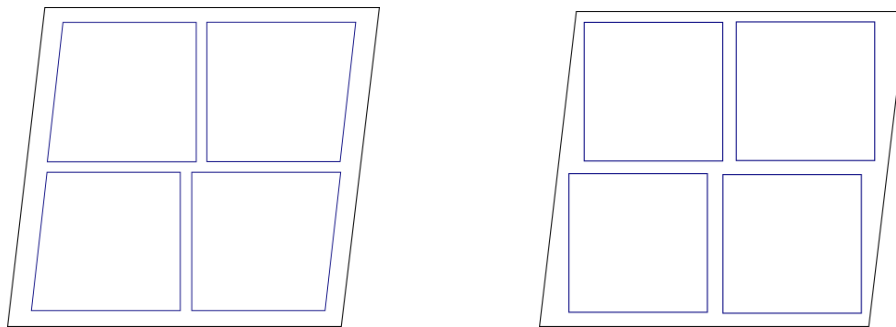


Figure 55. Unit mini module. On the left, a mini module with trapezoidal cells. Right, a mini module with square cells.

Considering the restriction hitherto mentioned and if the short-circuit current density of the Viko cell is estimated at  $380 \text{ [A/m}^2\text{]}$  the required area of each *cell* is  $15.077 \text{ [cm}^2\text{]}$ . The shape of this cells can be easily achieved using a laser cutter. Nevertheless, in practice, due to some scaling mistakes, the resultant size of the cells was  $16 \text{ [cm}^2\text{]}$ . The total area of each mini module is  $75.22 \text{ [cm}^2\text{]}$

With this design, the total area occupied by the cells is  $64 \text{ [cm}^2\text{]}$ . The cell spacing area is  $[4.9 \text{ cm}^2]$  and the border area  $6.32 \text{ [cm}^2\text{]}$ .

However, if a square cell with exactly the same area is used, the spacing area becomes  $5.06 \text{ [cm}^2\text{]}$ . And the border area becomes  $6.16 \text{ [cm}^2\text{]}$ . The differences between the two shapes becomes very small. When comparing both approaches, the expected losses according to the CTM analysis presented previously due to shape are compared in

Table 6.

	Trapezoid	Square
$k_1$ (losses due to border area)	0.9209	0.9229
$k_2$ (losses due to cell spacing)	0.9387	0.9367

Table 6. Comparison of the inactive area loss factor of a trapezoid cell vs a square cell.

The advantages of using a trapezoid cell is that the border area remains constant throughout the entire module. Whereas for a square cell, some corners are too close to the module's border increasing the risk of wither delamination or exposure (not being laminated) because the small

threshold. Using a smaller cell size could overcome the problem sacrificing efficiency and output power.

A series connection was proposed following the pattern of Figure 56. Note that each mini module has now two inputs *and* two outputs. The advantage of this pattern is that the terminals lie within one of the corner facets. Thus, allowing a possible attachment of the electronics when folded. Another advantage is that it reduces the connection length of each mini module. If a traditional module was laminated (1 input, 1 output), with 4 cells, the terminals of each mini module will be on the same side. Therefore, an additional wire of the length of the mini module is needed to connect it to the next one. This, in addition to the hinges can potentially increase the resistive losses. With the proposed design the length of each connection is minimized. Furthermore, with the proposed connection scheme both terminals, (+) and (-), are on the same *facet*. This allows a possible connection of junction boxes or other external elements. Keeping in mind that this is a foldable module, the connection to the external circuit must be on one corner to prevent interfering with the folding.

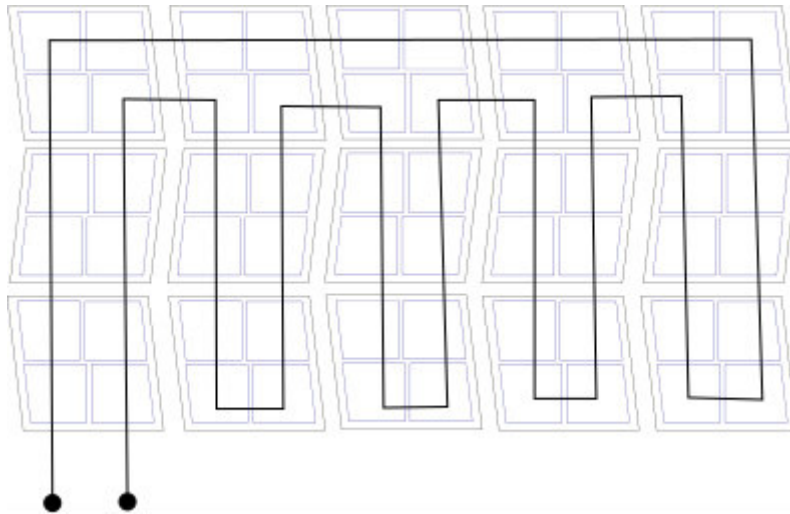


Figure 56. Proposed connection scheme for the foldable module. Note that the terminals are in one corner element. This allows the insertion of an external circuit or junction box without interfering with the folding.

## 5.4. Prototype

A demonstrator with the previous design was built. Each unit mini module consists of 4 cells laminated with flexible foil and black back sheet. This *foil-to-foil* method is useful to create non-square shapes as it avoids the need for cutting glass. Further, by painting the busbars with a black permanent marker, the cells become practically invisible.

Tyvek® was used to support the whole design. Tyvek® is a polymer material designed by DuPont. One of the main features of the material is that it resembles paper; but, it can withstand tear, is waterproof and recyclable [53]. This makes it suitable as a back support because the Miura fold can be done in Tyvek® following the same procedure as in a normal

paper. The hinges are then automatically constructed. Each resultant folding mark is used as a guideline to glue the mini modules in place.

One of the main challenges of this module is to create the electrical connections of Figure 1Figure 56. Especially the inter module connection is difficult because the chosen solution must be able to bend along the hinge. For this reason, the proposed approach is the use of an electrically conductive tape. The available tape was an aluminium tape. Since the aluminium is difficult to solder with a traditional analogue soldering station, an ultrasonic station and solder were used to attach a piece of tape to the corresponding tabbing wires.

The completed module is a 54 x 32 [cm] rectangle when unfolded but only 24 x 19 [cm] when folded. This is roughly one-quarter of the unfolded area (top view). Pictures of the folded and unfolded finished prototype can be seen in Figure 57 and Figure 58.

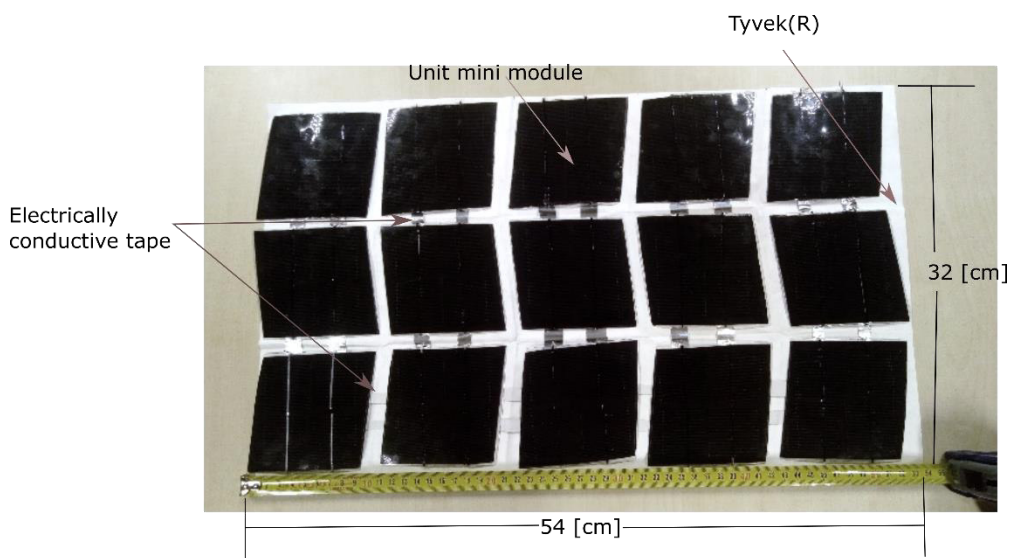


Figure 57. Unfolded prototype. By painting the busbars with a black permanent marker, the cells became practically invisible.

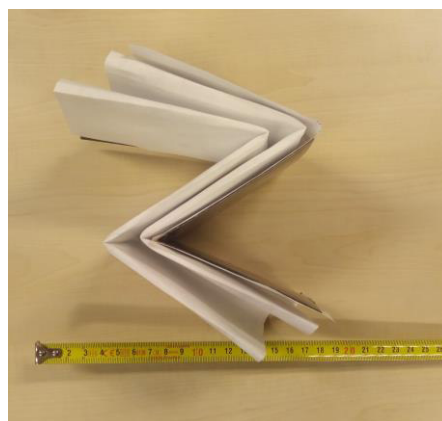


Figure 58. Folded state. Top view. The dimensions are 24 x 19 [cm].

#### 4.5.1. Effect of the front sheet material

The foldable module was encapsulated using a flexible front sheet material. This overcomes one of the main problems of the CORNING glass which is the ability to create non-square shapes. Although it is possible to cut CORNING glass using a diamond, it is a lengthy process which can lead to breaking of the glass, sharp edges that could be dangerous for the user or incomplete cutting.

The flexible front sheet, on the other side, can be easily cut with scissors or a guillotine. This makes the process faster and safer. Moreover, the flexible foil is not fragile as glass and it is also lighter.

Figure 59 compares the transmittance of the CORNING glass, used in the reference module with that of the front sheet used for the foldable one. Although the CORNING glass allows the light transmission in the small wavelength range, the response of the cell is not high. From 800 to 1000 [nm] the cell converts most of the light into electricity. At this point, both materials have almost the same transmittance value. The CTM factor is expected to be, therefore, very close to that of glass.

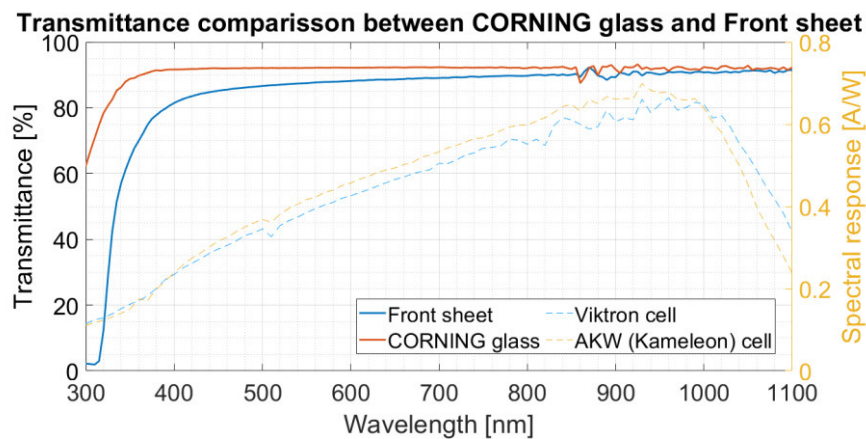


**Figure 59. Comparison of the transmittance of the CORNING glass and flexible front sheet. Although the glass has a greater transmittance for lower wavelengths than the front sheet, the wavelengths in this region produce less electrons. On the peak of the spectral response of the cells, both materials behave almost the same. The spectral responses of both, the AKW and Viko cells are plotted for reference.**

A similar analysis was done in Figure 60 to compare the refractive indices of both materials. The refractive index for the EVA is plotted for reference. In Section 1.4.2 it was explained that the CORNING glass and the EVA had almost the same refractive index. This leads to a small reflection at the glass-EVA interface. The front sheet has also a close value but the difference is higher than the glass that has a better matching over the whole spectrum.

Again, in the region where the cell performs better, the difference becomes very small and can be stated that the indices are matched.



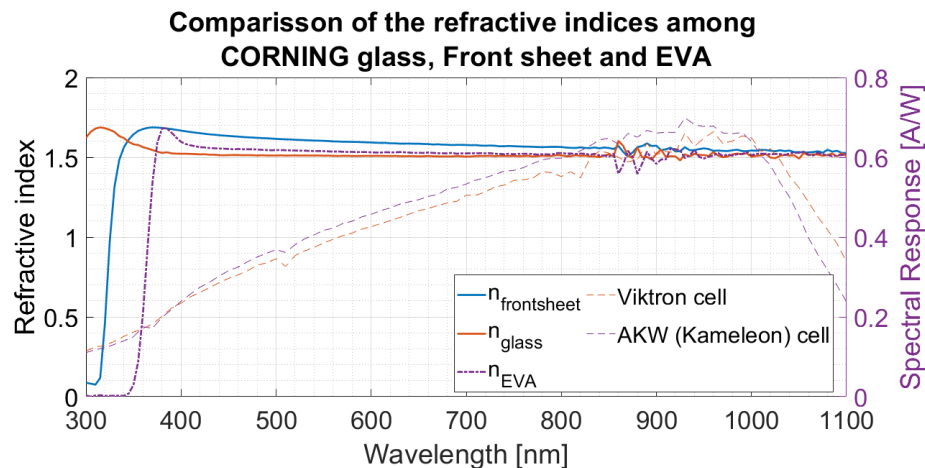


Figure 60. Refractive indices of the CORNING glass and front sheet. The Spectral response of the AKW and Viko cells are plotted for reference. The refractive index of the EVA is also plotted. The glass has a better matching than the front sheet, even around 900 [nm] where the spectral response of the cells is at its highest. However, in this region the difference is small.

From these two figures, it seems that the material is optimized to operate in the highest response region of the cell. This is reinforced when looking at the reflectance of the front sheet as shown in Figure 61. Here, the differences between glass and front sheet become more evident

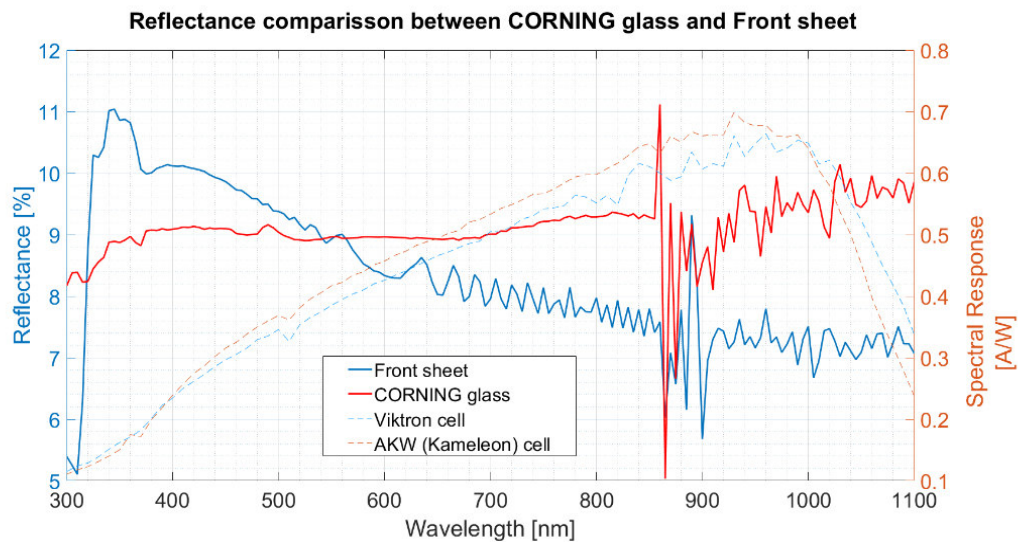


Figure 61. Reflectance of the CORNING glass with respect to the front sheet. The reflectance of the front sheet over performs that of the CORNING glass in the region where the cell responds better. In the small wavelength region, the situation is opposite. However, the cell does not perform well in this region.

The last feature to be analyzed is the absorptance of the front sheet. It was discussed earlier that the CORNING glass has a very low absorptivity. From Figure 62 it is clear that the front sheet absorbs more light than the glass. It is expected that this is reflected in the CTM factor.



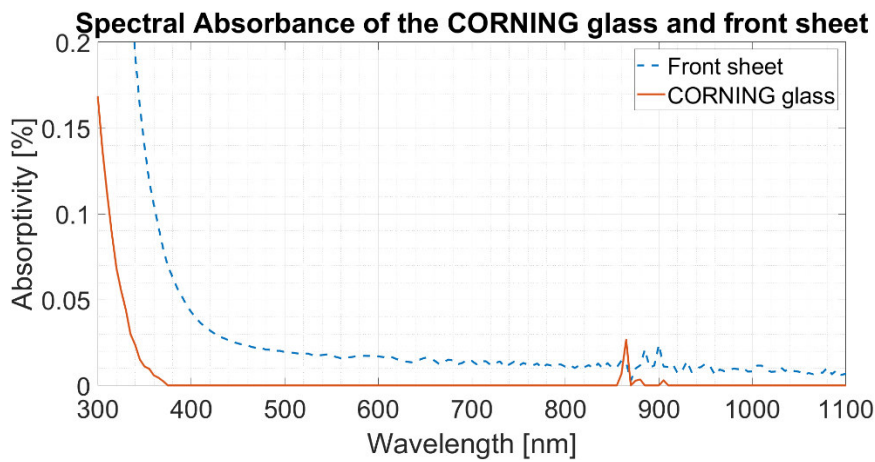


Figure 62. Absorbance of the front sheet and CORNING glass. Note that the front sheet absorbs more light than the glass.

The CTM factors are compared in

Table 7. Although it was expected that the reduced reflection of the front sheet had a greater impact, it is not very large. This gain cannot compensate for a greater absorption of the front sheet.

	CORNING glass	Front sheet
Reflection	0.91	0.92
Absorption	1	0.98
Reflection glass (front sheet)-EVA	0.99	0.99

Table 7. Comparison of the CTM factors of the reference module of Section 1.4.5 and the foldable module prototype. The numbers refer to the  $k_i$  factors and are dimensionless. A higher number indicates that the losses are low. For instance, the front sheet reduces the reflection losses in comparison with glass, but has also a greater absorption loss.

#### 4.5.2. Prototype performance

In order to determine the performance of the prototype, its IV and PV curves were measured. Considering the full area of the module, the measured efficiency is only 9.3 %. This poor result is because of the large inactive areas. Adding to the already existing border and cell spacing areas, an additional spacing was introduced *between mini modules* to allow the folding.

If only the active area is considered, an initial efficiency of 17.27 % was achieved. The module is able to deliver 16.58 [W] at its maximum power point. Figure 63 shows the IV and PV curves of the module. As a summary, the external parameters are also shown in

Table 8.

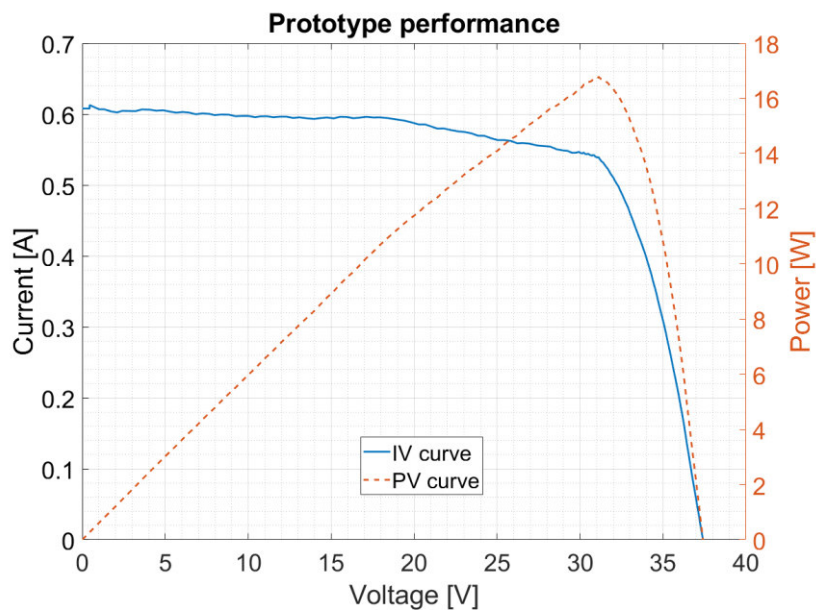
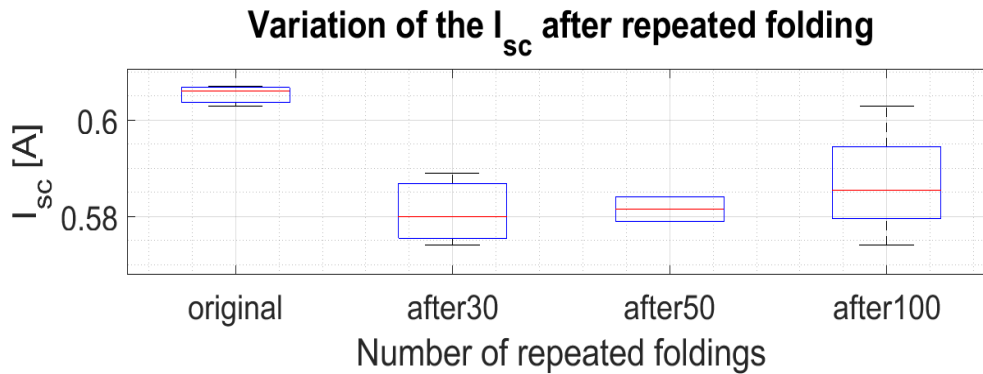


Figure 63. IV and PV curves of the foldable module just after fabrication.

Parameter	Value
$V_{oc}$	37.6 [V]
$I_{sc}$	0.6 [A]
$P_{mpp}$	16.58 [W]
FF	0.73 [-]
Module efficiency	9.3 %
Active area efficiency	17.27 %

Table 8. External parameters of the foldable module.

So far, the performance was analyzed as *initial*. This is, just after fabrication. To determine the effect of folding an unfolding, an analysis similar to [51]. The module was then subjected to continuous folding an unfolding for 30, 50 and 100 times. After each sequence, the IV curves were measured under the LASS to determine if there is a change in the short circuit current.



**Figure 64. De-rating of the short circuit current as a result of folding and unfolding. In all cases, the current decreased indicating that the folding had an effect on the connections.**

Figure 64 shows that when the module is subjected to folding, the short circuit current diminished and never return to the original state. This reduction in the current can be explained as an *adjustment* of the connections just as explained in [51]. Moreover, by looking at the electroluminescence picture of Figure 65 there are some damaged cells. One of them being on the corner. This is important since in order to fold-unfold the module, it is grabbed by one of the corners. Thus, possibly stressing the already-damaged cell.



**Figure 65. Electroluminescence analysis of the foldable module. It can be seen that the module suffered some damage during manufacturing (dark areas). Also, some cracks were formed during lamination and the cells themselves have some defects that appear as irregular spots.**

When the module was connected via the buck converter to a mobile phone, it was not able to charge it. This does not mean that the module or the buck are not operational. Rather, the control circuit of the telephone is preventing it from charging. If an 80% efficiency is assumed for the buck converter, the maximum power that can be delivered to the load is 13.26 [W]. This value is below the 15 [W] that were needed to correctly supply the telephone.

## 5.5. Future work

Improvements to the present design can follow different paths. For instance, one of the main improvements lay on the hinge system. So far, the hinges were folded into Tyvek®. However, the fact that the whole module presents a zig-zag shape when folded instead of a flat surface as is supposed to be, is related with the thickness of the modules.

Flat origami (such as the Miura-ori) pattern allows the folding of a rigid panel. Mathematically, all the patterns can be folded flat keeping each panel unaffected [54]. However, these patterns are designed ignoring the material thickness and some modifications are needed in order to take into account this fact [54, 55]. The methods should be such that the characteristics of the original fold are preserved. Depending on the application, different approaches have been proposed. Morgan, *et al*, [56] discuss the *offset panel technique* in which the panel is shifted downwards where a valley fold is formed. The hinge is introduced in the intersection between the two modules. They proved this concept on the Miura folding of a circuit board with 1.6 [mm] thickness.

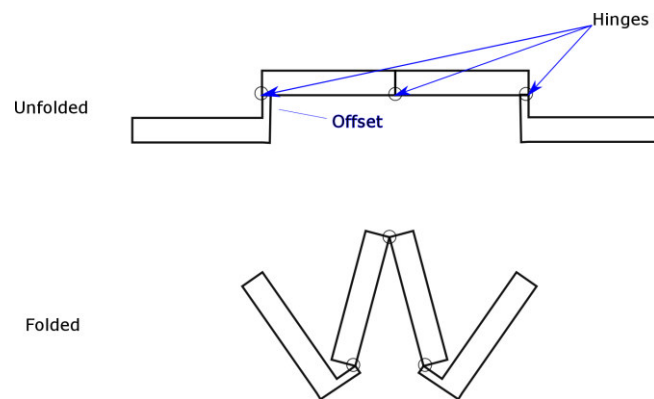


Figure 66. Offset panel technique. Adapted from [56]. Note the offset of the lower panel to form a valley fold.

The hinges also present an additional problem. The survival of the electrical contact. As the metal will be subject to motion, it is possible that after some folding-unfolding sequences the conductor will break. For the proposed tape, it can withstand at least 100 cycles without damage, but this is a small number considering the lifetime of the product. Test on the durability of the connections should be further performed and alternatives developed. Even more, conductive hinges might be beneficial for this kind of design even allowing different connection schemes.

Finally, the construction of the Miura fold allows the addition of new unit modules, as long as the folding pattern is preserved. This means that the sequence of *mountain* or *valley* fold should be kept and, naturally, the shape of each unit module. Additionally, to fully benefit from the design, an easy attach-detach system should be used.

Modularity possesses two important challenges.

1. The addition of new hinges.
2. The electrical connection of the new units to the existing array.

One possibility is the use of conductive hinges. In that way both problems are attacked at one. However, the concept needs to be further developed.

## 5.6. Conclusions

A foldable module based on the Miura-ori fold was fabricated. The designed included trapezoidal cells that accommodate better to the parallelogram mini modules needed for the Miura fold to work. However, square cells of the same size can also be used with no impact on the border area efficiency loss, nor the cell spacing. The disadvantage of square cells relies on the fact that they are too close to the edges of the mini module. This means that slightly smaller cells are recommended if squares are to be used.

A Tyvek® was used as a support and to create the hinges in the desired shape. This material behaves like paper allowing to follow a traditional folding to create the pattern, thus the hinges. The electrically conductive tape was used to interconnect each unit module as it is flat and flexible.

The effect of the front sheet was analyzed and its performance compared with the CORNING glass. This material presents many advantages over glass since it is lightweight and easy to cut in custom shapes. The optical performance is very similar to glass and the results lead to conclude that it has been optimized to operate in the highest spectral response point of the solar cells. It helps to improve the reflection loss, with the disadvantage that absorbs more light than the CORNING glass.

The flexible module performs reasonably well although it is not able to supply a 15 [W] load when connected to an 80 % efficiency buck converter.

Although the efficiency of the module at a full area is rather small, the active area efficiency provides an acceptable result.

Further work needs to be done in upgrading the hinge system taking into account the thickness of the modules, adding modularity and flexibility in the connection schemes.



# 6

## Solar puzzle

There is a wide range of commercially available toys with integrated solar power (*solar toys* or *photovoltaic toys*). Most of them incorporate a single-cell module to provide power for moving a piece or lighting the product.

However, these modules are often squares or rectangles. Even if the module is of different shapes, the cell inside are squares which result in a lot of unused space.

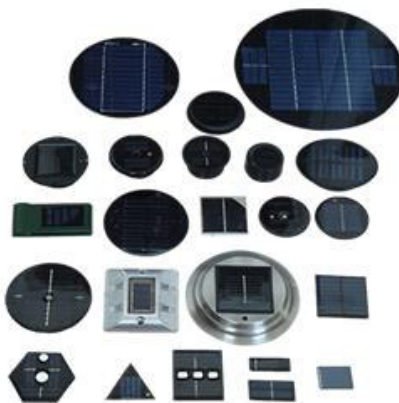


Figure 67. Commercially available mini modules from Link Light Solar. Retrieved from [57].

Furthermore, the cell itself is a different piece which can be easily perceived.

In the case of photovoltaic puzzles, the products are mostly 3D wooden puzzles which incorporate a solar cell as an external piece.

The only product that claims a similar behaviour of single cells as puzzle pieces is proposed by SOUKO Robots [58]. Although, at the moment of writing this report it was not clear if it is a concept or a commercially available product.

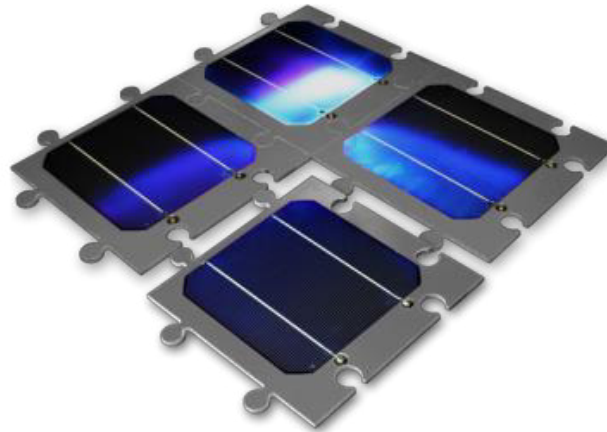


Figure 68. SOUKO Robots' photovoltaic puzzle concept. Retrieved from [58].

## 6.1. Puzzle Requirements

It was decided to design a puzzle such that each of the pieces is a single-cell solar cell cut into the desired shape. These cells were first laser cut and then encapsulated in a foil-to-foil single cell module. The terminals are soldered into Neodymium magnets which will form the connection when placed over an electrically conductive copper tape. Each piece is covered with silicone rubber covering the connection of the cell and leaving only the sunny side of the module and the magnets exposed. When all the pieces are fitted together, they will power up an array of 6 RGB (Red-Green-Blue) LEDs. By turning three knobs it is possible to change the colours of the LEDs.

The reasoning of the above decisions is based on the requirements that were set in order to design the puzzle. These are enlisted in Table 9.



Requirement	Solution
<i>The pieces must contain solar cells</i>	The pieces are solar cells cut into the puzzle shape and laminated as single-cell modules
<i>The puzzle must allow handling by a 4-year old child</i>	Silicone rubber is used to house each piece module and connections
<i>The connections of the pieces should be done in a seamless manner</i>	Neodymium magnets are used the terminals of the cell. They make contact on a conductive wire tape pasted on top of a stainless-steel board
<i>The puzzle must be able to power at least a LED</i>	The load are 6 RGB LEDs equipped with safety resistors and potentiometers for colour change. The pieces are cut large enough to meet this requirement
<i>The puzzle should self-indicate when it is properly assembled</i>	Only a correct assembly leads to the lighting of the LEDs. Even under low light conditions the RED led will shine.
<i>The puzzle must be attractive for a 4-year old child</i>	All the pieces, when assembled form a sailfish. The pieces are also coloured in blue and the puzzle allows the control of the LED colours.
<i>The puzzle should provide an adequate challenge for its assembly</i>	All the connections remain hidden and only some initial pieces are fixed. The only guideline is the position for the magnets and the final figure.

Table 9. Fulfillment of requirements.

## 6.2. Cell shapes

Figure 69 shows the desired figure that will form the solar puzzle. It is based on the silhouette of a sailfish (top) (*Istiophorus* spp). The decomposition into different shapes which will form the cells can be seen in Figure 69 (bottom).

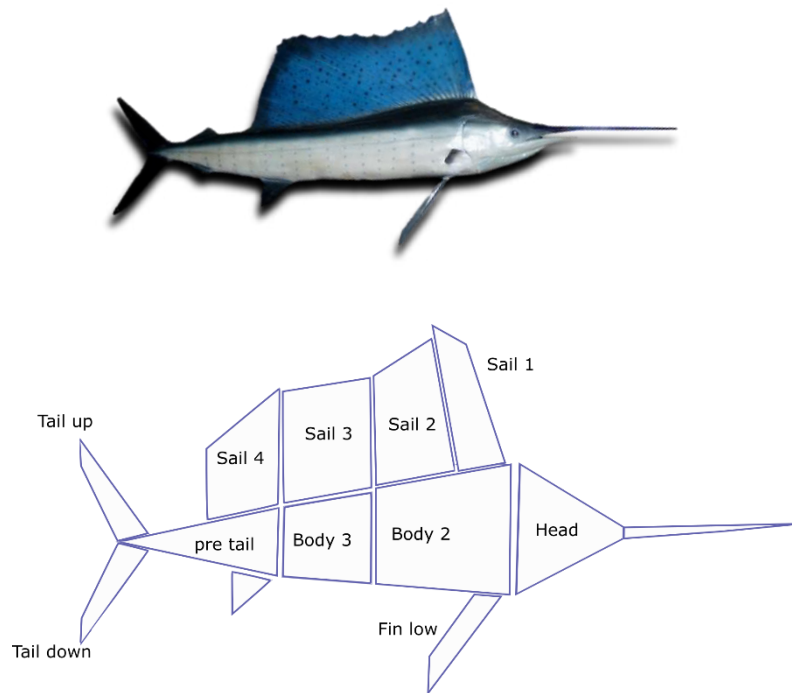


**Figure 69. Solar puzzle fish design. Top, Image of an *Istiophorus* spp. Retrieved from [59]. Bottom, decomposition into geometrical shapes. The names assigned to each cell is also shown here. These names will be used throughout this chapter.**

Cutting the cells in such shapes also represent a challenge as some of them are very thin (i.e. the nose) and can easily break during either process of the mini module making (cutting, soldering or lamination).

Three full 15.6 x 15.6 [cm] full cells are needed to cut all the pieces. Note that in Figure 70, the busbars are not always parallel to the base of the figures, nor centered or even straight.



**Figure 70. Cut cells prior to soldering and encapsulation.**

Since the cells are not soldered, as in traditional modules, one to each other, the orientation of the busbars does not play a crucial role. Furthermore, in order to save material, the greatest

number of pieces should be cut from a single full-size cell. This is not possible when using straight busbars.

After soldering and lamination, only 11 single-cell modules were used. The two smallest pieces (nose and back lower fin) were not used as modules.

The different size of the cells implies a current mismatch. The pieces near the head are the largest and will not be able to produce at their full potential because of the limiting current of the cells at the tail and lower fins. In order to overcome this issue, the short-circuit current of each mini module was measured and assigned to a *group*. Each group is connected in *series*. Member within a group are connected in *parallel*. This strategy allows the *reduction* of the current mismatch by 36.23 % while keeping a voltage high enough to power the load.

The resultant single-cell modules and their characteristics as well as the group they were allocated are best described in

Table 10.

1-cell module	Active area [cm <sup>2</sup> ]	I <sub>sc</sub> [A]	V <sub>oc</sub> [V]	Group
Body 2	67.86	1.17	0.616	1
Body 3	32	0.78	0.62	5
Fin low	9.48	0.211	0.598	7
Head	33.62	0.866	0.61	4
Pre tail	24.73	0.512	0.617	8
Sail 1	23.05	0.578	0.63	7
Sail 2	37.89	0.889	0.616	3
Sail 3	43.27	0.969	0.617	2
Sail 4	30.19	0.72	0.619	6
Tail down	9.39	0.214	0.626	8
Tail up	9.39	0.198	0.619	6

Table 10. Parametrization of the single cell module.

### 6.3. Mini module interconnection

The interconnection of the cells also represents a challenge as they are not perfectly aligned. Moreover, depending on the shape, they can have more than one busbar. These multiple busbars mean that an extra connection must be made within them. However, since the single cell module must be laminated as close as possible to the cell in order to preserve the shape, there is no extra space for additional connections. Therefore, it was decided to allocate all the

tabbing wires to the back of the laminated module and then perform the connections on the outside. They remain protected from the environment by the silicone rubber.

As no cables will be used and the pieces must allow an easy and quick connection and disconnection, the terminals of each modules are connected to Neodymium magnets. The electrical connection is achieved when the magnets touch and electrically conductive copper tape placed on top of a stainless-steel board. The interconnection scheme is shown in Figure 71 and the equivalent electrical diagram is shown in Figure 73

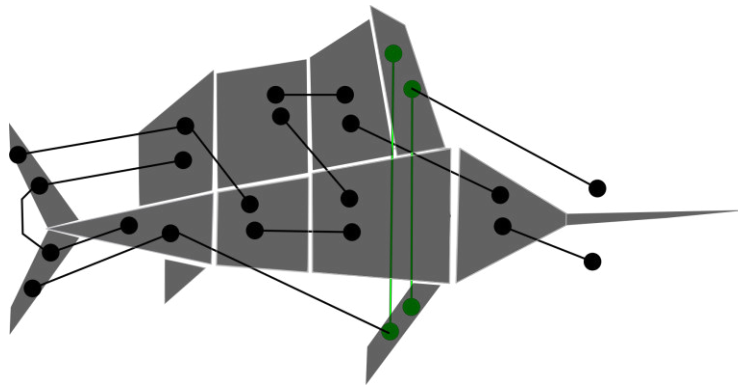


Figure 71. Interconnection scheme. Some lines are drawn in red for clarity.

Since, according to the requirements, the removal of a single piece must cause the load to turn off, a solution must be found to turn off any of the parallel connected cells.

This is achieved by breaking the connection pad at the point where the parallel group is connected in series to other cells. The circuit is closed when the magnet is placed and becomes open when the piece is removed, thus causing the load to turn off. This is illustrated in Figure 72.

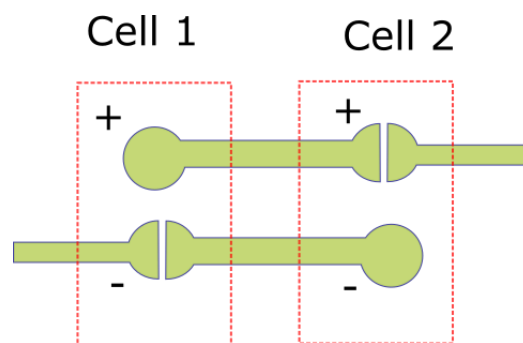


Figure 72. Solution for breaking the parallel connection. When a magnetic contact is placed on top of the broken pad, it closes the circuit turning the load on. The removal of any piece causes the circuit to become open.

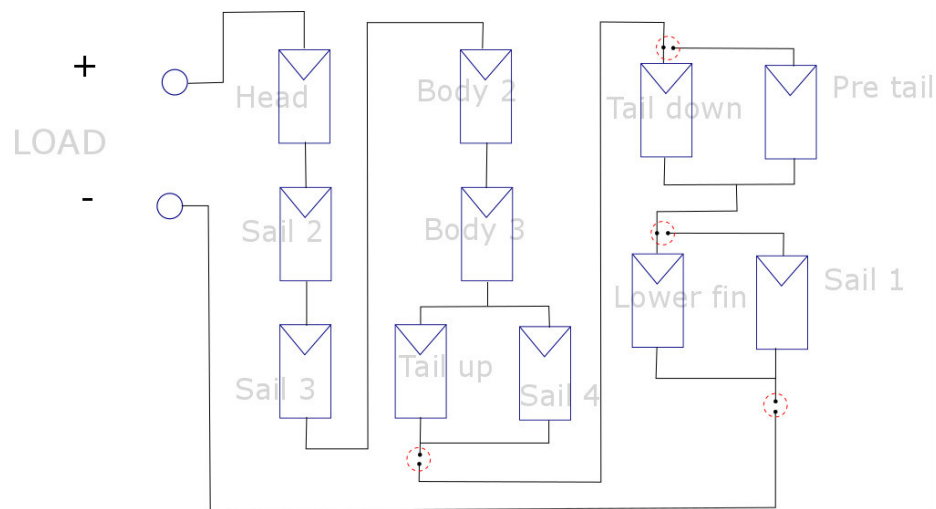


Figure 73. Electrical diagram of the puzzle interconnection. The red dotted circles indicate the points where the tracks are connected as in Figure 72.

## 6.4. Final design

The finished puzzle can be appreciated in Figure 74.

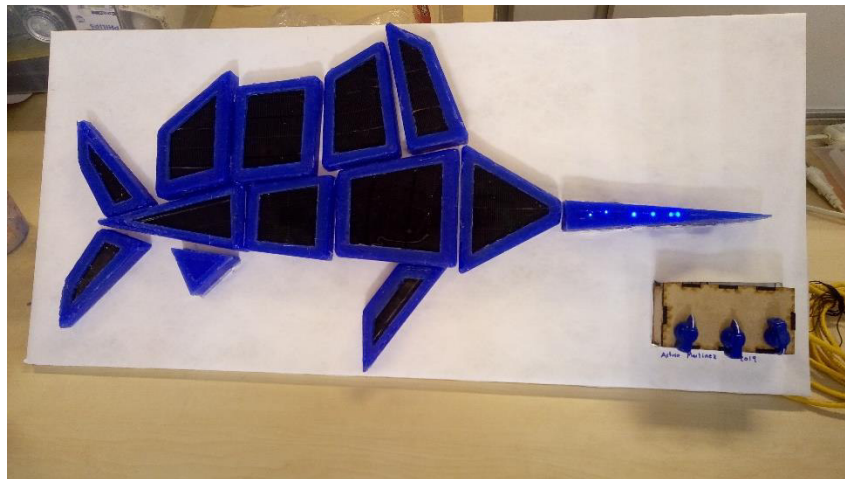


Figure 74. Finished PV puzzle.

An electroluminescence analysis was performed in order to check that all the mini modules were operating as well as determining the damages during lamination. Furthermore, when recalling at Figure 76, the biggest piece is not properly working as its IV curve is almost a straight line.

Figure 75 depicts the electroluminescence results. All the mini modules are operating despite the cracks in almost all the pieces.

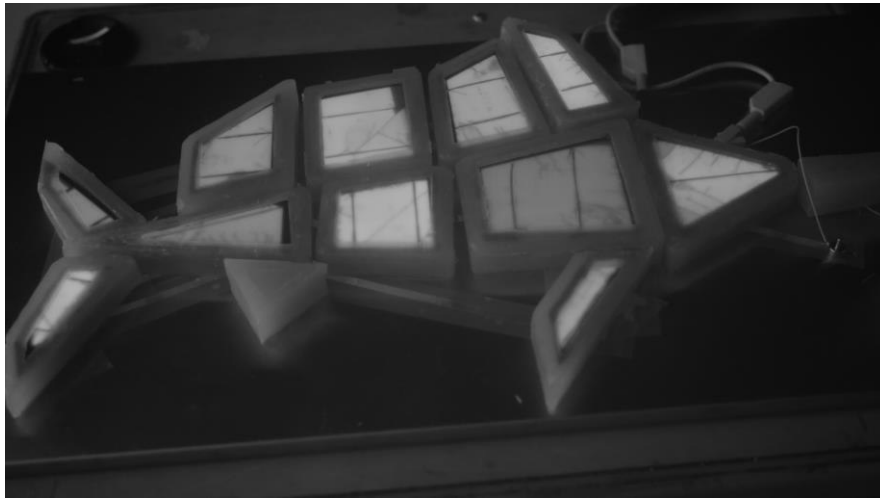


Figure 75. Electroluminescence picture of the PV puzzle. Cracks can be seen in the whole puzzle. However, their effect is small. The biggest problem is in “Sail 3” which has a complete area in black. Because of the already existing current mismatch, this black area doesn’t represent a big problem.

Even though some pieces show dark areas, this does not affect the performance of the puzzle because of the already existing current mismatch. Furthermore, the electroluminescence show that the biggest piece is less bright indicating poor performance.

## 6.5. Analysis of the finished puzzle

In order to keep the interconnection hidden and flat, each mini module unit is connected to each other using electrically conductive copper tape. This material is an adhesive tape made of copper which allows current flow not only in the direction of the copper but also *through* the adhesive.

The tape was chosen because of the flexibility that it offers in terms of ease of interconnection, flatness and adherence to a magnetic surface (stainless steel). However, this material has not been designed for its use in solar systems and it is mainly used in shielding applications.

According to the manufacturer [60], the resistance through the adhesive is only 0.005 [ $\Omega$ ]. However, measurements of resistance with a bench multimeter, show that the resistance considerably increases when the adhesive part of the tape is placed in contact with the copper side of it (i.e., creating a connection). Furthermore, when performing an IV curve measurement of all the pieces as in Figure 76, it becomes evident that all the pieces have an elevated series resistance. Since the connections are on the back of the pieces, a pad was built with the same electrically conductive tape. Each segment was glued in a shingle manner, allowing a wide area for placing the magnets and measuring each piece.

The results of Figure 76 suggest that the tape has a major impact on the module performance. This can be noted by the high series resistance of practically all the cells).

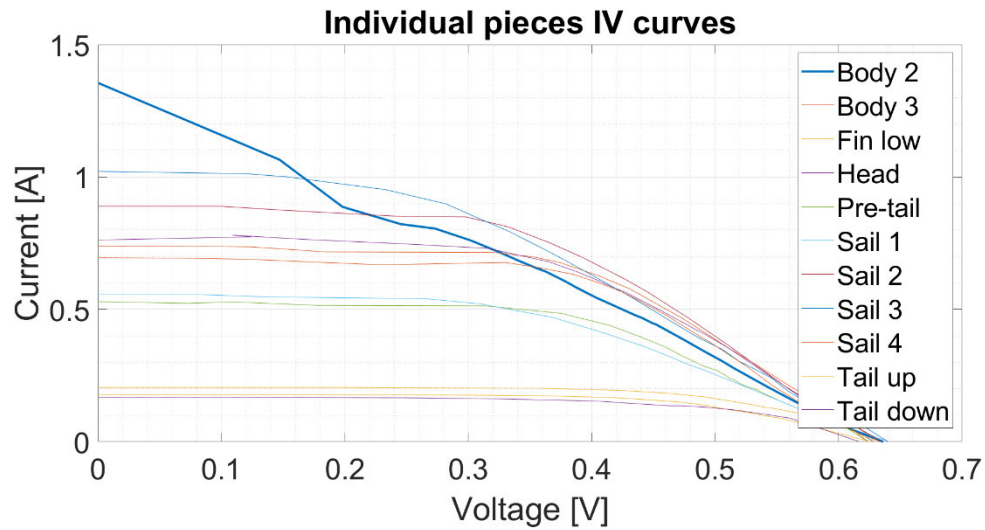


Figure 76. IV curves of the individual mini module pieces. It can be seen that the biggest cell “Body 2” (thick line) is underperforming. This can be corroborated with the electroluminescence picture of Figure 75. Also note the large current range. From cells producing less than 0.5 [A] to cells that almost triplicate the smaller ones.

Since each piece is different, the removal of different pieces must have a different effect over the whole module. To determine this, each piece was removed and short circuited (if in series) or left open (if in parallel). The effect over the rest of the puzzle was measured under the LASS.

As expected, in Figure 77 it is possible to note that the main effect is the reduction of the current. Especially when the larger pieces are removed in parallel with the small ones. For example, the removal of “pre-tail” results in a very small current since the remaining small piece, “tail down” is in series with the array; hence, limiting the current.



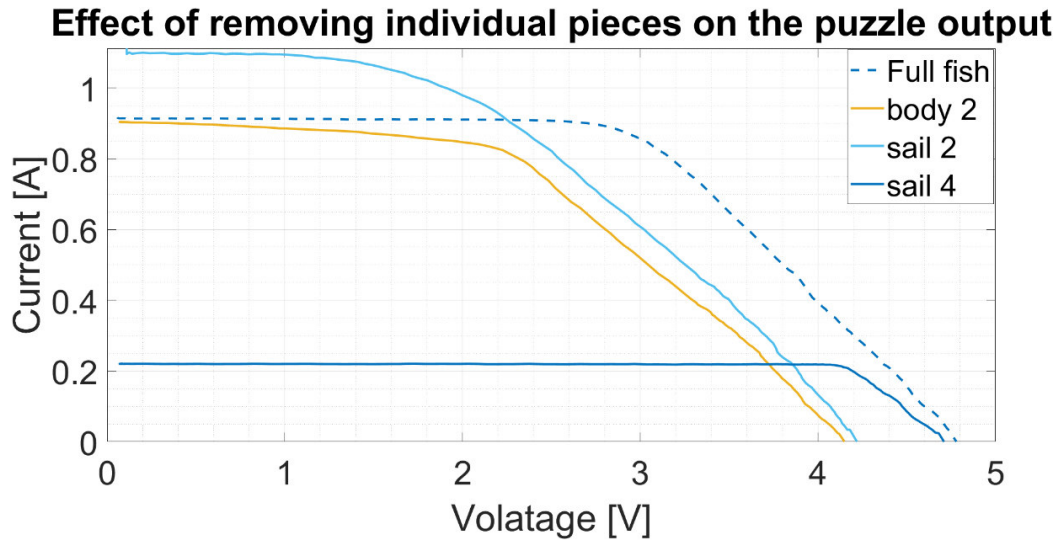


Figure 77. IV curves of the whole puzzle when each individual piece is removed. For clarity, not all of the pieces are shown here. The IV curve of the whole puzzle is shown as a dashed line. Here it can be seen that the piece “sail 2” is limiting the current. When it is removed the current rises. Since it is in series, its removal also causes a voltage drop.

The opposite occurs with “sail 4”. This cell is connected in parallel, so the voltage drop is basically null. It is connected to a small piece; therefore, removing it leaves only the small piece in series. This limits the current. The piece “cell 2” that is underperforming causes only the corresponding voltage drop. It is also an indicator that the current of this cell is being limited.

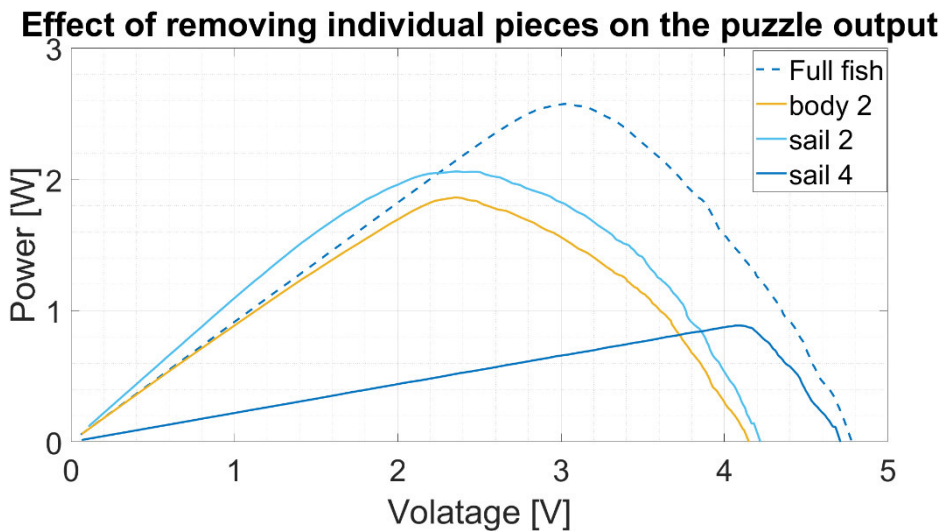


Figure 78. PV curves of the whole puzzle when each of the pieces is removed. Analog to the IV curves, removal of large pieces cause a significant drop in power. Even “body 2” that is underperforming has an important role in the array as the power is greatly reduced when this piece is missing. As before, the removal of “sail 4” leaves only the small cells in series limiting the whole array current.



Figure 77 and Figure 78 also show that the fill factor improves when only the small cells are operating and degrades when these are removed. As fewer current flows through the copper tape adhesive, the resistive losses are greatly reduced resulting in an improvement of the fill factor.

The efficiency of the full puzzle was calculated as 8.03% for the active areas. This result is no surprise taking into account the great current mismatch of the cells. Further, when cutting the cells, the focus was put on saving material rather than achieving a high efficiency. For this application, efficiency is not as important as to getting enough power to feed the load.

Figure 79 supports the statement that the smaller pieces have almost no influence on the overall performance. Care must be taken when interpreting the effect of removing “tail down”. From the figure, it seems that its removal improves the efficiency. Nevertheless, this might be not the case. When taking measurements of this piece, the IV curve exhibited a changing behavior. Part of it is attributed to a rising temperature while measuring under the LASS, but also contact problems might be behind the unexpected results.

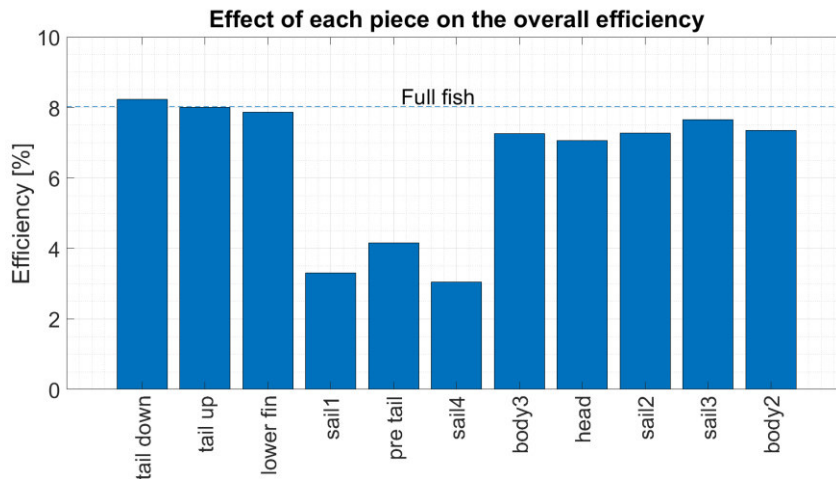


Figure 79. Effect on the efficiency caused by removing each individual cell. At first sight, it would seem that the removal of “tail down” increases the puzzle efficiency. Care should be taken while interpreting this.

## 6.6. Future work and applications

The solar puzzle demonstrates the potential of using mini modules interconnected in non-conventional ways. If a different housing is used for the mini modules, for instance, concrete or wood, then the integration of solar energy into buildings becomes even easier as the products can become truly building *integrated*. This is even enhanced by the fact that figures different that squares may be also achieved; improving, therefore, the esthetics of the products.

To improve current development, the reliability of the magnetic contact pads must be ensured. Replacing the adhesive joint with another connection method, like soldering, could reduce the resistive losses considerably. A re-design of the magnetic pads is also needed to ensure a proper connection of the pieces.

The most significant development would be exploring options for adapting the product for indoor applications. While it currently can power very low power LED with indoor light, the power is not enough to light up the blue and green LEDs which demand more current.

The design proposed uses black back sheet to hide the solar cells. The next step for improving esthetics would be experimenting with coloured cells.

## **6.7. Conclusions**

A solar puzzle was designed proving that nickel coated Neodymium magnets can be effectively used as contacts. The effect over the resistance losses is negligible. The copper side of the tape is an excellent conductor and can be used for solar applications. However, while the electrically conductive adhesive of the tape simplifies greatly the connection process, it increases the series resistance of the whole array in a considerable amount. The resistance of the adhesive increases when the tape starts to peel off, which is common if it is subject to additional mechanical stress. In the case of the PV puzzle, the connection, sliding and disconnection of the pieces cause the tape adhesive to wear down. Thus, increasing the resistance of the whole array. The effect of the series resistance was verified by analysing the effect of each piece over the whole puzzle. When the smaller pieces are left in series, there is an improvement of the fill factor as a result of less current flowing, thus reducing the resistive effect.

# 7

## Conclusion and Recommendations

New ways of producing solar modules can lead to a better integration of PV energy into products and buildings. Traditional rectangular modules are difficult to merge in products. For this reason, designers and architects can benefit from modules that can be custom produced, especially regarding its shape and size. This thesis had as an objective to demonstrate that by using c-Si solar cells that are commercially available, it is possible to produce custom modules. Especially regarding the shape and size of the cells and the connection schemes.

To do this, four research main research questions were proposed. In this chapter they will be summarized and the way they were answered explained.

The first research question *What is the effect of cutting a c-Si solar cell into different shapes and sizes?* was addressed in Chapter 3 – *Creating custom shapes*. Here, commercial cells were laser cut and the effect on the efficiency analysed. It was proven that the use of a laser cutter indeed affects the solar cell by introducing new shunts and edge recombination. If the laser parameters are not properly chosen, then the reduction of efficiency may be significant. With this, the first sub question (*Does the laser cutting process have a significant effect on the efficiency?*) is answered.

The research continued with the analysis of the cut cell size. For this, the second sub question *Is there a shape that leads to a better performance?* was proposed. Here it was discovered that the shading area of the cells plays an important role. It cannot be stated that there is a single shape that leads to a better performance. However, the geometry of the cell should be chosen such that the shading fraction is reduced and, avoiding to split the cell into several sub cells by looking at the finger pattern. The best performance was found to be such that the relation between the cell perimeter and shaded fraction lay between the limits marked by Figure 35. This also helps to answer the third and last sub question *Can solar cells be cut into very tiny pieces?* Very small cells will have a large perimeter-to-area ratio which means that the edge recombination losses will prevail, reducing the resultant efficiency.

In Chapter 4 – *Building mini modules* the second research question *How does the CTM ratio behaves within the small-sized module?* was tackled especially in sub section 4.1 – *Cell-To-Module*. To answer this, a reference module was built and the analysis of a full sized-module was followed. The main difference is that the cell original size was not considered but the already cut cells. A ratio greater than 1 was achieved for the reference module thanks to the optical gains. However, this with the disadvantage of a quite large border area. The method used here provides a good starting point for the CTM analysis, especially for different materials. The sub question *Can the same approach of commercial-sized modules be used?* has

for answer yes, but only as an approximation. It is based on assumptions that are only valid for square shapes. Therefore, a specific analysis of different geometries must be carried out.

Sub section 4.2 – *Electrical contact* provides the basis for answering the third research question *Which innovative interconnection schemes can be used for PV modules?* Two methods were proposed to addressing the question: magnets and an electrically conductive adhesive tape. Both methods facilitate the connection of the modules in applications where cables and connectors are not suitable. For instance, the PV puzzle required flat connections in order to completely hide them. The magnets provide a good solution for quickly attachment of the pieces. *How does the conductive adhesive behave within small-sized modules?* Well, if it is used with the adhesive in direct contact to the cells, the output is unsatisfactory. Nevertheless, if it is used as tape-tape connection it can achieve a better result. The resistance of the adhesive increases as it wears out by attaching and detaching the tape. This kind of wearing is experienced in applications where and adhered junction is subjected to motion, such as the PV puzzle. In the case of magnets, *Does the use of magnets have a significant impact on the cell's output?* No. It was found that the proposed magnets can be effectively used as contacts for solar cells. The induced loss is extremely small. Even more, the advantages of a quick and reliable connection further expand the benefits of these products.

The proposed concepts of Chapters 5 and 6 (i.e. the foldable module and the PV puzzle) provide the answer to the fourth and last research question: *How can a mini-module help with the integration of PV power into daily life activities?.* By combining non-square shapes and unconventional connection methods it is possible to create a wide range of products where solar power is integrated. The two prototypes serve as an evidence for this. The use of front sheet eliminates the necessity of glass giving the designer great flexibility in adapting the PV modules directly into the products.

## 7.1. Recommendations

### 1.7.1. Laser cutting

This thesis focused on solar cells with busbars at the front. Other technologies among which are MWT or busbarless solar cells should also be tested. The reduction of shaded area of these technologies might help to improve the resultant efficiency. Also important is to reduce the waste material. With the used cells, only the pieces that are connected to the busbar can be used which results in a large quantity of cell wasted.

The laser cutting machine plays a very important role in the results achieved. Since the parameters are valid only for a specific machine, a universal method for determining them should be studied. This can lead to fewer time and material consumption so far needed to do this.

### 1.7.2. Cell-To module

The method presented here is a good starting point. The major drawback is that it doesn't consider the losses induced by the laser cutting. The main reason why it is not used lays in the corrected power  $P_0$ . Since a full solar cell can have more power than a mini module, it makes no sense to use the full cell power. The whole calculation algorithm is based on this value so a careful adaptation should be done.

New geometries demand adapting some parameters, especially the fitting functions that are given only for squares.

Also, it can be interesting to include the current mismatch losses as a separate value of  $k$ . Currently the losses are indeed taken into account but not expressed in the results.

### 1.7.3. Electrical contacts

Due to restrictions in storage requirements and chemical management, two products were not tested. Namely an electrically conductive adhesive that needs to be stored at  $-20$  [°C] and an Electrically Conductive paint. The use of this product was restricted due to unknown health hazards. Due to regulations of TU Delft, the product was only approved for use in the clean room. This made it inconvenient for the purpose of this project.

The ECA is currently being used in the fabrication of shingled modules. Its use in the PV industry is not unknown. Since traditional soldering leads to cell breakage, further use of ECA can help to minimize these events and allow new connection methods.

The conductive paint can also help to implement new connection methods and can be even an interesting option for substituting traditional tabbing wire. The selected paint had silver particles so its resistance was expected to be very low. Other cheaper presentations include nickel particles instead of silver.

### 1.7.4. Foldable module

As discussed earlier, better hinges have to be proposed in order to achieve a more compact product. Furthermore, they can also be used to produce shade-tolerant modules if they are made conductive by facilitating the connection of different cell groups within the module.

A layer of Tyvek® can also be implemented on the front side of the prototype to help to protect the connections. This material can also be investigated as a housing for modules as it is waterproof and lightweight.

Modularity, can provide a great advantage of this module. One way to do this is using the features of magnets described here. The hinges might be fabricated as magnetic (and conductive) elements allowing a very easy way to keep the foldability and modularity.

Challenges of modularity include (besides the hinges), keeping or modifying the cell string as new elements are added.

#### 1.7.5. PV puzzle

The attachment of the magnets to the silicone rubber housing had to be done by making the tabbing wire to support the magnets while the rubber was poured over the mould. However, since the magnets are not perfectly supported, they can move during the procedure. Thus, the result can be them not being perfectly flat. As a result, only a small fraction of it might actually make the contact. For this reason, a better method for attaching them is needed.

Also, currently only the rim is touching the base, making the contact area quite small. Trying to maximize this area is one of the steps to improve the user experience. Likewise, making the magnets to fit better into the base will help the user to place the pieces without having to find if they're in touch with the tape or not.

# 8

## References

- [1] B. Petter Jelle, C. Breivik, and H. Drolsum Røkenes, "Building integrated photovoltaic products: A state-of-the-art review and future research opportunities," *Solar Energy Materials and Solar Cells*, vol. 100, pp. 69-96, 2012/05/01/ 2012.
- [2] I. Cerón, E. Caamaño-Martín, and F. J. Neila, "'State-of-the-art' of building integrated photovoltaic products," *Renewable Energy*, vol. 58, pp. 127-133, 2013/10/01/ 2013.
- [3] B. P. Jelle and C. Breivik, "The Path to the Building Integrated Photovoltaics of Tomorrow," *Energy Procedia*, vol. 20, pp. 78-87, 2012/01/01/ 2012.
- [4] P. B. Isa Zanetti, Francesco Frontini, Erika Saretta, Guus Verberne, Finn M. Vossen, Menno van den Donker, Kostas Sinapsis, Wiep Folkerts, "Building Integrated Photovoltaics: Product Overview for solar Building Skins," SUPSI, University of Applied Sciences and Arts of southern Switzerland, SEAC, Solar Energy Application Centre 2017, Available: [https://www.seac.cc/wp-content/uploads/2017/11/171102\\_SUPSI\\_BIPV.pdf](https://www.seac.cc/wp-content/uploads/2017/11/171102_SUPSI_BIPV.pdf).
- [5] M. E. Max Mittag, Helen rose Wilson, tobias Fellmeth, "Mosaic Module Concept for Cost-Efficient and Aesthetic BIPV Modules," presented at the 35th European PV Solar Energy Conference and Exhibition, Brussels, Belgium, 2018. Available: [https://www.ise.fraunhofer.de/content/dam/ise/de/documents/publications/conference-paper/35-eupvsec-2018/Mittag\\_6AO75.pdf](https://www.ise.fraunhofer.de/content/dam/ise/de/documents/publications/conference-paper/35-eupvsec-2018/Mittag_6AO75.pdf)
- [6] (19-12-18). *Dutch Solar Design*. Available: <http://www.dsd-pv.nl/>
- [7] N. Adamovic, A. Zimmermann, A. Caviasca, R. Harboe, and F. Ibanez, "Custom designed photovoltaic modules for PIPV and BIPV applications," *Journal of Renewable and Sustainable Energy*, vol. 9, no. 2, p. 021202, 2017/03/01 2017.
- [8] G. Apostolou and A. H. M. E. Reinders, "Overview of Design Issues in Product-Integrated Photovoltaics," *Energy Technology*, vol. 2, no. 3, pp. 229-242, 2014/03/01 2014.
- [9] E. Findeisen, R. H. H. Tjokropranoto, J. Rijnenberg, J. Lenssen, and A. Reinders, "Integration of flexible photovoltaic modules on top of inflatable tents," in *2016 IEEE 43rd Photovoltaic Specialists Conference (PVSC)*, 2016, pp. 2715-2717.
- [10] A. Sacco, L. Rolle, L. Scaltrito, E. Tresso, and C. F. Pirri, "Characterization of photovoltaic modules for low-power indoor application," *Applied Energy*, vol. 102, pp. 1295-1302, 2013/02/01/ 2013.
- [11] G. Apostolou, "Investigating the Use of Indoor Photovoltaic Products Towards the Sustainability of a Building Environment," *Procedia Environmental Sciences*, vol. 38, pp. 905-912, 2017/01/01/ 2017.
- [12] P. Satpute, R. M. Punekar, and A. Shende, "Opportunity Areas for Industrial Designers to Explore New Applications of Product-Integrated Photovoltaics (PIPV) for Rural Communities of India," in *Research into Design for a Connected World*, Singapore, 2019, pp. 413-422: Springer Singapore.
- [13] S. McLeod. (2007, 12-08-2019). *Maslow's hierarchy of Needs*. Available: <https://www.simplypsychology.org/maslow.html>



- [14] Lasergraaf NL. (13-08-2019). *Wat is een fiber laser nu precies*. Available: <https://lasergraaf.nl/archief/wat-is-een-fiber-laser-nu-precies/>
- [15] S. Villa, "Colored PV modules based on Interference Filters," Master of Science, TU Delft, 2018.
- [16] P. Maggioni, "Upscaling thin film solar cells for water treatment devices," MSC, TU Delft Electrical Engineering, Mathematics and Computer Science, Delft University of Technology, 2018.
- [17] BELVAL S.A., "PASAN CELL TESTER IId Operation and Service Manual," ed, 2006.
- [18] Experia Solar. (13-08-2019). *Experia Laboratory Laminator*. Available: <https://www.experia.solar/lab-laminator/>
- [19] L. T.C., "Periodic-Random Modulated Surface Textures," Master of Science, Photovoltaic Materials and Devices, TU Delft, 2018.
- [20] Iscount Laboratory services. (2015, 13-08-2019). *PerkinElmer Lambda 650/750/950*. Available: <https://www.isocount.com/>
- [21] AKW Solar, "MONO 3BB 5.0W 100PC," ed.
- [22] I. Haedrich, U. Eitner, M. Wiese, and H. Wirth, "Unified methodology for determining CTM ratios: Systematic prediction of module power," *Solar Energy Materials and Solar Cells*, vol. 131, pp. 14-23, 2014/12/01/ 2014.
- [23] B. S. Yilbas, "1 - Introduction," in *The Laser Cutting Process*, B. S. Yilbas, Ed.: Elsevier, 2018, pp. 1-4.
- [24] Lasegraaf. (12-02-2019). *MOPA & Q Fiber lasers 101 - Hoe werken ze en wat zijn de verschillen*. Available: <https://lasergraaf.nl/mopa-q-fiber-lasers-101-hoe-werken-ze-en-wat-zijn-de-verschillen/>
- [25] R. Paschotta. (2008, 11-02-2019). *Fluence*. Available: <https://www.rp-photonics.com/fluence.html>
- [26] K. McIntosh and C. B. Honsberg, *The Influence of Edge Recombination on a Solar Cell's Iv Curve*. 2000.
- [27] D. Bertrand, S. Manuel, M. Pirot, A. Kaminski-Cachopo, and Y. Veschetti, "Modeling of Edge Losses in Al-BSF Silicon Solar Cells," *IEEE Journal of Photovoltaics*, vol. 7, no. 1, pp. 78-84, 2017.
- [28] S. Eiternick, K. Kaufmann, J. Schneider, and M. Turek, "Loss Analysis for Laser Separated Solar Cells," *Energy Procedia*, vol. 55, pp. 326-330, 2014/01/01/ 2014.
- [29] D. Zhang and L. Guan, "4.06 - Laser Ablation," in *Comprehensive Materials Processing*, S. Hashmi, G. F. Batalha, C. J. Van Tyne, and B. Yilbas, Eds. Oxford: Elsevier, 2014, pp. 125-169.
- [30] C. Hördemann, C. Fornaroli, and A. Gillner, "Ultrashort pulsed laser-dicing of silicon wafers for the decollating of conventional and hybrid solar cells," in *Proceedings of SPIE - The International Society for Optical Engineering*, 2017, vol. 10363.
- [31] C. Fornaroli, J. Holtkamp, and A. Gillner, "Dicing of Thin Si Wafers with a Picosecond Laser Ablation Process," *Physics Procedia*, vol. 41, pp. 603-609, 2013/01/01/ 2013.
- [32] Shenzhen JPT Opto-electronics, "YDFLP Laser Installation Guide and user Manual," ed, 2016.
- [33] D. Bertrand, M. Pirot, S. Manuel, A. K. Cachopo, and Y. Veschetti, "Fabrication of High Voltage Modules by Optimization of Performances of Reduced Area Silicon Solar Cells," *Energy Procedia*, vol. 92, pp. 715-720, 2016/08/01/ 2016.
- [34] G. H. Yordanov, O.-M. Midtgård, and T. O. Saetre, "Series resistance determination and further characterization of c-Si PV modules," *Renewable Energy*, vol. 46, pp. 72-80, 2012/10/01/ 2012.
- [35] Q. Cheng, "The perimeter-area fractal model and its application to geology," *Mathematical Geology*, vol. 27, no. 1, pp. 69-82, 1995/01/01 1995.
- [36] J. Y. Yang *et al.*, "Research on decrease of cell to module loss for crystalline silicon photovoltaic module," *Journal of Renewable and Sustainable Energy*, vol. 5, no. 5, p. 052003, 2013/09/01 2013.
- [37] C. Honsberg and S. Bowden. (2019, 11/08/2019). *Spectral Response*. Available: <https://www.pveducation.org/pvcdrom/solar-cell-operation/spectral-response>



- [38] National Renewable Energy Laboratory (NREL). (03-06-2019). *Reference Solar Spectral Irradiance Air Mass 1.5*. Available: <https://rredc.nrel.gov/solar//spectra/am1.5/>
- [39] O. Dupré, J. Levrat, J. Champliand, M. Despeisse, M. Bocard, and C. Ballif, "Reassessment of cell to module gains and losses: Accounting for the current boost specific to cells located on the edges," 2018, vol. 1999.
- [40] M. Braunovic, V. V. Konchits, and N. K. Myshkin, *Electrical contacts : fundamentals, applications and technology*, Boca Raton: CRC Press, 2007. [Online]. Available.
- [41] G. Windred, "Electrical contact resistance," *Journal of the Franklin Institute*, vol. 231, no. 6, pp. 547-585, 1941/06/01/ 1941.
- [42] J. Park, W. Oh, H. Park, C. Jeong, B. Choi, and J. Lee, "Analysis of solar cells interconnected by electrically conductive adhesives for high-density photovoltaic modules," *Applied Surface Science*, vol. 484, pp. 732-739, 2019/08/01/ 2019.
- [43] S. Zhang *et al.*, "A study on the resistivity and mechanical properties of modified nano-Ag coated Cu particles in electrically conductive adhesives," *Journal of Materials Science: Materials in Electronics*, vol. 30, no. 10, pp. 9171-9183, 2019/05/01 2019.
- [44] T. Geipel, M. Meinert, A. Kraft, and U. Eitner, "Optimization of Electrically Conductive Adhesive Bonds in Photovoltaic Modules," *IEEE Journal of Photovoltaics*, vol. 8, no. 4, pp. 1074-1081, 2018.
- [45] U. Eitner, T. Geipel, S. N. Holtschke, and M. Tranitz, "Characterization of electrically conductive adhesives," 2012, vol. 27, pp. 676-679.
- [46] Supermagnete. (18/08/2019). *Neodymium magnets: the super strong ones*. Available: <https://www.supermagnete.de/eng/supermagnete-strong-neodymium-magnets>
- [47] Y. Nishiyama, "Miura Folding: Applying Origami to Space Exploration," *Interational Journal of Pure and Applied Mathematics*, vol. 79, pp. 269-279, 2012.
- [48] K. Miura, "Method of Packaging and Deployment of Large Membranes in Space," *The Institute of Space and Astronautical Science*. 618, 1985.
- [49] K. Miura, "Triangles and Quadrangles in Space," in *Proceedings of the International Association for Shell and Spatial Structures (IASS) Symposium*, Valencia, 2009.
- [50] E. Landau. (2014, 16-07-2019). *Solar Power, Origami-Style*. Available: <https://www.nasa.gov/jpl/news/origami-style-solar-power-20140814>
- [51] R. Tang *et al.*, "Origami-enabled deformable silicon solar cells," *Applied Physics Letters*, vol. 104, no. 8, p. 083501, 2014/02/24 2014.
- [52] B. Jasim and P. Taheri, "An Origami-Based Portable Solar Panel System," in *2018 IEEE 9th Annual Information Technology, Electronics and Mobile Communication Conference (IEMCON)*, 2018, pp. 199-203.
- [53] DuPont. (2019, 16-08-2019). *what is Tyvek(R)* Available: <https://www.dupont.com/tyvekdesign/design-with-tyvek/why-tyvek.html>
- [54] T. Tachi, "Rigid-Foldable Thick Origami," in *Origami 5: Fifth International Meeting of Origami Science, Mathematics, and Education*: CRC Press, 2016, pp. 253-263.
- [55] S. A. Zirbel *et al.*, "Accommodating Thickness in Origami-Based Deployable Arrays1," *Journal of Mechanical Design*, vol. 135, no. 11, pp. 111005-111005-11, 2013.
- [56] M. R. Morgan, R. J. Lang, S. P. Magleby, and L. L. Howel, "Towards Developing Product Applications of Thick Origami Using the Offset Panel Technique," *Mechanical Sciences*, vol. 7, pp. 69-77, 2016.
- [57] Link Light Solar. (2011, 30-06-2019). *Mini-watt Epoxy encapsulated Solar Panels 0.1-9W*. Available: <http://www.linklightsolar.com/mini-watt-solar-panels.html>
- [58] SOUKO Robots. (2019, 30-06-19). *Photovoltaic puzzle*. Available: <http://www.soukosrobots.gr/en/environmental-en/photovoltaic-puzzle>
- [59] Wikipedia editors. (2019, 13-08-2019). *Sailfish*. Available: <https://en.wikipedia.org/wiki/Sailfish>

- [60] 3M Innovation. (2000, 15-07-2019). *1181 Tape. Copper foil with Conductive Adhesive. Datasheet.* Available: <https://docs-emea.rs-online.com/webdocs/0097/0900766b80097b8f.pdf>

## 8.1. Lasergraaf technical specifications

The technical specifications of the Lasergraaf are shown in Table 11.

Average Output Power [W]	30
Full Power Frequency Range [kHz]	60-1000
Adjustable Frequency Range [kHz]	1-1000
Pulse width Range ( $T_{on}$ ) [ns]	6-250
Laser wavelength [nm]	1064
Power range%	0-100

Table 11. . Lasergraaf technical specifications. Retrieved from [32].

## 8.2. Method for determining the Cell-To-Module ratio

Table 12 shows the loss and gain mechanisms. It is important to mention that in this study  $k_7$  was not considered as the used cells had a continuous busbar design. Therefore, there is no shading due to soldering. Also,  $k_8$  to  $k_{10}$  were considered as a single mechanism.

$k_1$	Loss factor due to module border
$k_2$	Loss due to cell spacing
$k_3$	Loss factor due to glass reflection
$k_4$	Loss factor due to glass absorption
$k_5$	Loss factor due to glass-EVA reflection
$k_6$	Loss factor due to EVA absorption
$k_7$	Loss factor due to ribbon shading (non-continuous busbar design).
$k_8$	Gain factor due to optical coupling of the cell's anti-reflection coating
$k_9$	Gain factor due to optical coupling of the finger scattering
$k_{10}$	Gain factor due to optical coupling of the busbar scattering
$k_{11}$	Gain factor due to back sheet reflection
$k_{12}$	Loss factor due to cell interconnection
$k_{13}$	Loss factor due to string interconnection

Table 12. Loss and gain factors as defined by Haedrich *et al* [22].

When the cells are connected in series, the least producing cell will limit the current of the whole array. This loss is taken into account by the value  $P_0$ . This magnitude refers to the sum of powers of every cell connected in *series* within the array and adjusted for the current

mismatch by looking at the IV curves of each cell and estimating of each cell at the point of the minimum current of the array

### 8.3. Buck converter design for the foldable module

The prototype is intended to work as a mobile charger; therefore, a USB interface was needed. With the assumption that the module is to be operated outdoors, under full sun illumination, only a buck converter was proposed. This allows stepping down the voltage from 15 [V] to 5[V] as required by USB.

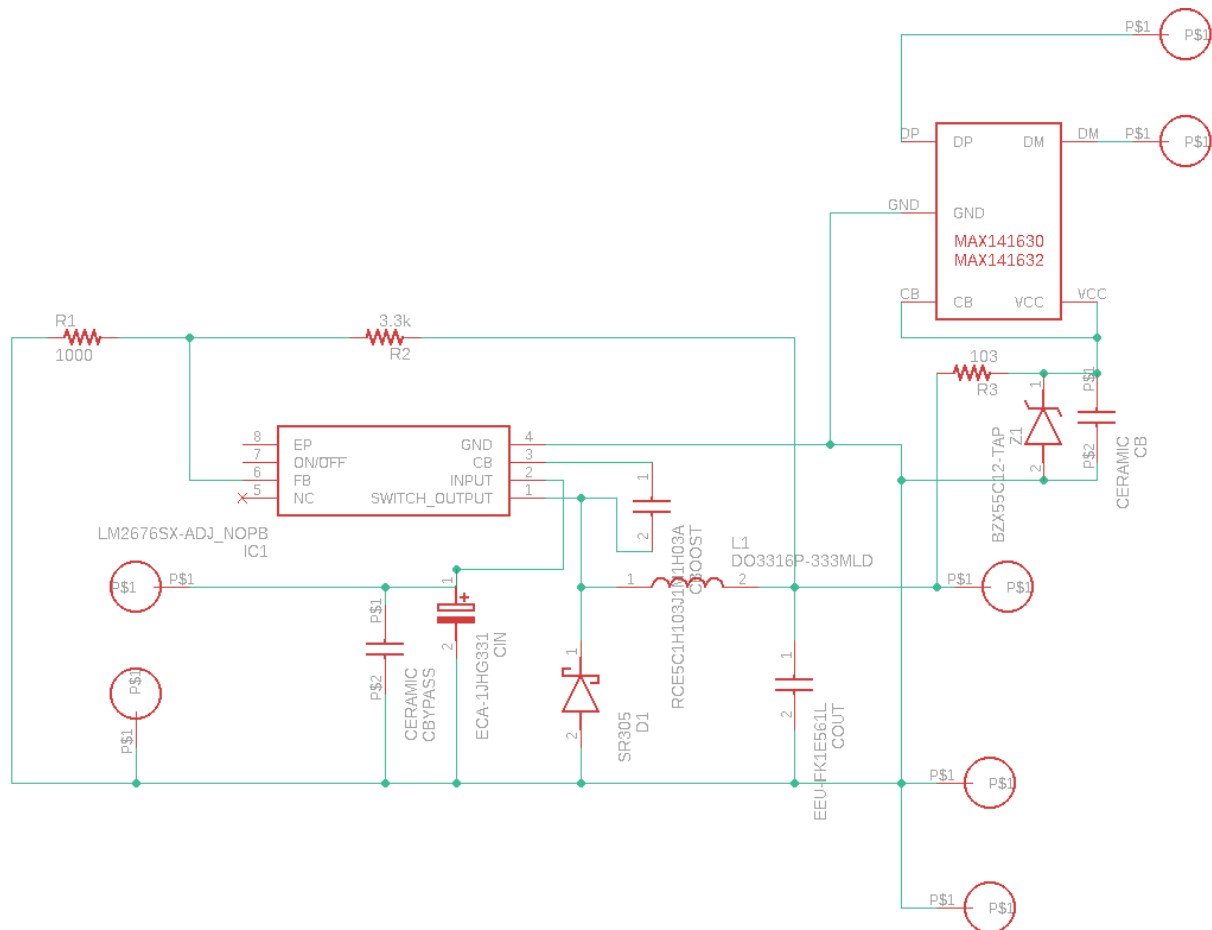


Figure 80. Schematic diagram for the buck converter.

A USB emulator was added to the design to allow the connected device to work in a high-current charging mode. To prevent damage to this additional integrated circuit (IC), a 5.1 [V] zener diode limits the feeding voltage of the IC when the buck converter has no load.